Low-Temperature Tolerant Gel Polymer Electrolytes for Rechargeable Zn-Air Batteries

by

Jiayao Cui

A thesis submitted in partial fulfillment of the requirements for the degree of

Master of Science

in

Chemical Engineering

Department of Chemical and Materials Engineering

University of Alberta

Abstract

Global warming and climate change are driving the use of cleaner energy sources to replace fossil fuels. Wind and solar energy are renewable and sustainable clean energies and can generate electricity. However, both wind and solar energy depend on the weather conditions. Storing the electricity in batteries is a way to create a more consistent supply. Li-ion batteries are the most widely used batteries currently, but their high price hinders their application in grid storage. In contrast, metal-air batteries, especially Zn-air batteries (ZABs), are gaining traction because of their safe operation and lower price compared with Li-ion batteries. Gel polymer electrolytes (GPEs) are emerging materials for ZABs as the GPE can act as an electrolyte and a separator in the ZAB and prevent short circuits caused by Zn dendrite formation. This thesis focuses on extending the working temperature range of the ZAB to low temperatures (as low as $-41℃$) as well as reducing the interfacial resistance between the GPE and the electrode.

The first study involved fabricating two GPEs (GPE-KOH and GPE-KOH-KI) for ZABs through the polymerization reaction of poly(acrylic) acid and KOH with (GPE-KOH) and without (GPE-KOH-KI) ZnO, followed by an immersion in a solution containing KOH, KI and ZnO (GPE-KOH-KI). ZABs using these two GPEs were tested at different temperatures and current densities. Both GPEs demonstrated excellent low temperature resistance and competitive performance in a ZAB compared with the literature. The ZAB using GPE-KOH was able to cycle at 10 mA cm^{-2} and $-28℃$ and at 5 mA cm^{-2} and $-41℃$ for 100 h (200 cycles). The initial and final efficiencies were 50% and 41% ($-28℃$, 10 mA cm^{-2}) and 42% and 32% ($-41℃$, 5 mA cm^{-2}), respectively. When tested at $21℃$, the ZAB using GPE-KOH exhibited a peak power density of 127 mW cm^{-2} and successfully cycled for 260 h (520 cycles) at 10 mA cm^{-2} before experiencing accelerated performance degradation. The initial efficiency was 61% and the efficiency at 260 h was 42%. The

addition of KI to the electrolyte changed the conventional charging reaction to a reaction with a lower thermodynamic barrier. The battery efficiency was improved significantly with a maximum increase of 36% relative to ZABs without KI. It was proposed that only the reaction at the Zn electrode was fully reversible, while the reaction at the air electrode was not, which would result in accumulation of KIO_3 as the battery cycles. When tested at 21℃, the ZAB using GPE-KOH-KI had a lower peak power density of 98 mW cm^{-2} compared with the ZAB using GPE-KOH, due to I^- occupying active oxygen reduction reaction sites, and was able to cycle for 100 h (200 cycles) at 10 mA cm^{-2} with initial and final efficiencies of 71% and 52%, respectively. When tested at −41℃ and 5 mA cm^{-2}, the battery could cycle for 100 h (200 cycles) with initial and final efficiencies of 52% and 43%, respectively.

The second study explored a new fabrication methodology to fabricate the GPE (without KI) by an in-situ method in the jig for ZAB fabrication. Our initial hypothesis was that the in-situ fabrication method could reduce the interfacial resistance between the electrolyte and the electrode and improve battery cyclability, compared with ZABs using ex-situ fabricated GPE, because the precursor solution has better fluidity and wettability and can establish a better contact with the air electrode. A battery cell was designed and fabricated via 3D printing to realize in-situ fabrication of GPE for ZABs. The interfacial resistance was not reduced, nor was the battery cyclability improved by in-situ fabrication of GPE. The battery cyclability was similar at 2 mA cm^{-2} for both synthesis methods, but the charging performance was worse for the ZAB using in-situ fabricated GPE when cycled at 5 mA cm^{-2} and 10 mA cm^{-2}. Scanning electron microscopy (SEM) and energy dispersive X-ray (EDX) spectroscopy revealed that GPE completely penetrated through the air electrode when in-situ fabrication of GPE was used. This caused electrolyte flooding, reduced

catalytic activity, and blocked GDL pores, leading to poorer battery efficiency and worse charging performance during battery cycling. Further studies are needed to test our initial hypothesis.

Preface

This thesis focuses on gel polymer electrolyte synthesis, battery configuration design, and electrochemical testing for rechargeable ZABs. The research presented in Chapter 3 and Chapter 4, along with the Supporting Information, is my original work.

The work described in Chapter 3 and Chapter 4 was done with the assistance of several colleagues. Mr. Labbe conducted some of the cyclic voltammetry tests and contributed to discussions about battery reversibility (Chapter 3). Mr. Hu performed some of the scanning electron microscopy analysis and recorded some data for the electrolyte retention test (Chapter 3). Ms. Ni Yang from the IOSI lab performed the ion chromatography experiment and provided insights about the results. Dr. Anqiang He provided suggestions for analyzing the air electrode samples (Chapter 4). Other gel polymer electrolyte composition optimization, electrode preparation, electrochemical testing, battery configuration design, and characterization analysis were conducted by myself. Manuscript preparation was accomplished with the help of Dr. Douglas G. Ivey and Dr. Hyun-Joong Chung.

Dedication

To my beloved parents.

Acknowledgements

First, I would like to thank my supervisor Dr. Douglas G. Ivey for giving me the opportunity to pursue a Master's degree. Dr. Ivey did not only teach me how to be a better engineer but a better person. He taught me how to show respect to everyone and think twice before saying what we want to say. He taught me what ethical standards we should follow, as an engineer and as a researcher. He showed me what a man would look like when he enjoys what he is doing. Thank you for always being patient with me and providing me with invaluable advice. I am so lucky to have you as my supervisor and will forever be grateful for the journey that I had with you.

I would also like to thank Dr. Hyun-Joong Chung, who gave me the opportunity to study in his group. Your rigorous attitude toward research inspires me and helps me become a better engineer and researcher. Your brilliant advice always enlightens me and gives me new ways of thinking. I could not complete this work without you.

I would like to thank Dr. Xiaolei Wang for supplying some experimental materials and his PhD student Zhixiao Xu for his thoughtful suggestions. I would also like to thank Dr. Hongbo Zeng and Dr. Arno De Klerk for allowing me to access their laboratories. Last but not least, I would like to thank IOSI staff Lisa Brandt and Ni Yang for their technical support.

Financial support from the Natural Sciences and Engineering Research Council of Canada (NSERC), and Future Energy Systems (FES, T06 P03) are gratefully acknowledged.

I would like to thank the group members in Dr. Ivey and Dr. Chung's group for their encouragement and support. Particularly, Matthew Labbe, thank you for being a good friend of mine. You truly made this study experience more joyful.

I am deeply grateful to my parents, who love me with all their hearts. Thank you for all the love and support. You are the shelter of my life.

Table of Contents

List of Tables

List of Figures

Chapter 1. Introduction

Climate change caused by the use of fossil fuels has been a topic discussed among many countries and organizations[1]. One of the solutions to this problem is to use renewable energy as the main source of energy[2]. However, renewable energy sources, such as wind energy and solar energy, are unstable in terms of supply due to uncontrollable weather conditions. To maintain a consistent supply of electricity generated by renewable power sources, grid storage systems can be used. Electricity can be stored in the systems when weather permits and supplied whenever needed[3]. Rechargeable batteries, especially metal-air batteries, have been considered as one of the most competitive candidates for this task. They are a cost-effective and efficient means of energy storage[4]. Although Li-ion batteries (LIBs) have proven their success in commercial use, the intrinsic instability of Li when exposed to air and the flammability of their electrolytes have caused concerns[5]. More importantly, the increase in demand of Li in recent years has led to a spike in the price of Li[6], which makes the use of LIBs for grid storage less cost effective[4].

Figure 1.1 shows typical metal-air batteries including their theoretical specific energies, volumetric energy densities and nominal cell voltages. Even though Li has the highest specific energy among all other metal anodes, Li-air batteries are still less competitive than the others, due to the reasons mentioned above. Similar to Li-air batteries, K-air and Na-air batteries need to use non-aqueous electrolytes as they are not stable in aqueous electrolytes. Mg-air and Al-air batteries can use aqueous electrolytes and their theoretical energies and specific energies are comparable to Li-air batteries. However, self-discharge and poor Coulombic charging efficiency caused by low reduction potentials are drawbacks of these two materials. Between the last two candidates, Zn is a better choice than Fe because Zn has a higher cell voltage and theoretical energy in aqueous metal-air batteries. Compared to Li, Zn is a much safer material and more abundant in the earth's crust[5]. Therefore, Zn-air batteries (ZABs) can potentially be a reliable and cost-effective solution for grid storage.

The practical energy densities of current commercial rechargeable ZABs are limited to about 150-180 Wh kg^{-1}, but recent progress in ZAB research suggests that the practical energy density can be improved greatly[7]. For example, Tran et al. achieved an energy density of 748 Wh kg_{Zn}^{-1} at 5 mA cm^{-2} and 146 mW cm^{-2} peak power density in a rechargeable ZAB[8]. An average Alberta household uses 20-26.6 kWh of electricity per day[9]. Therefore, assuming that electricity

is consumed at the same rate during the day (e.g., a rate of 0.833 kW), to produce a battery that has a capacity of 20 kWh to provide the electricity required for an average Alberta household for one day, at least 26.7 kg of Zn and an air electrode active surface area of 0.57 m^2 are needed. By comparison, 111 kg of Zn are required if the battery has an energy density of 180 Wh kg^{-1}.

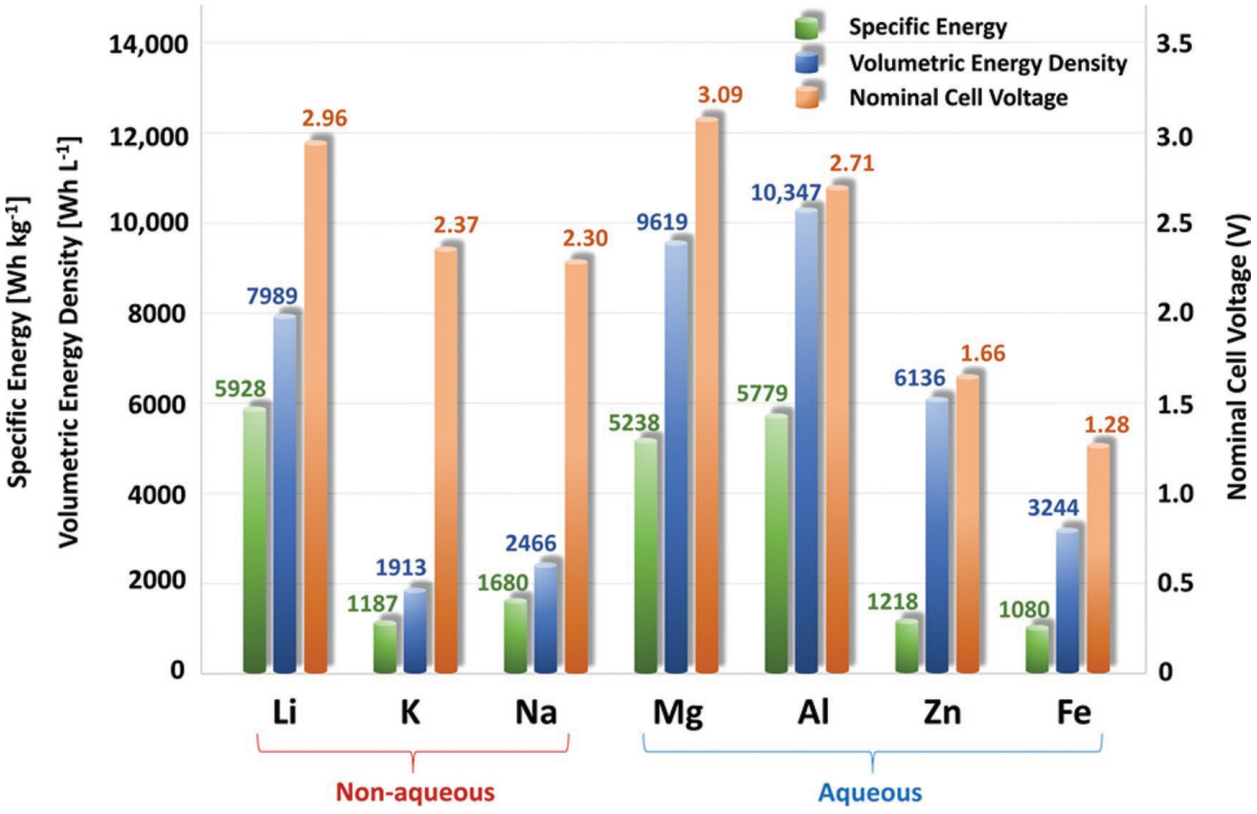

Figure 1.1. Theoretical specific energies, volumetric energy densities and nominal cell voltages for various metal anodes in metal-air batteries[5].

ZABs suffer from dendrite formation on the Zn electrode and aqueous electrolyte leakage. Gel polymer electrolytes (GPEs) can be used to mitigate these problems[10]. The use of GPEs can bring new problems to the battery, as GPEs cannot utilize the pores of the air electrode as well as aqueous electrolytes[5].

The objectives of this work are to develop GPEs for ZABs that can deliver competitive battery performance at various temperatures and to pursue in-situ fabrication of GPE to simplify production.

Chapter 2 presents a literature review of ZABs and electrolytes for ZABs, as well as the characterization techniques that are used in this work. Chapter 3 investigates two GPEs for ZABs that can operate at various temperatures. Chapter 4 explores the in-situ fabrication of GPEs for ZABs and its impacts on battery cyclability. Chapter 5 provides conclusions for the thesis as well as future directions.

Chapter 2. Literature Review

2.1. Zn-Air Batteries

Zn-air batteries (ZABs) have generated significant attention from researchers in recent years. ZABs have a relatively high theoretical energy density ($1218\ \mathrm{W\ h\ kg^{-1}}$) and volumetric energy density ($6136\ \mathrm{W\ h\ L^{-1}}$)[5]. The intrinsic properties of Zn being a safer and more abundant material than Li give ZABs an advantage in terms of grid storage of electricity[4].

2.1.1. ZAB Chemistry

Figure 2.1 shows a typical setup for a ZAB. In a typical ZAB, there are four components, a metallic Zn electrode, a porous air electrode, a separator, and an alkaline electrolyte. The main purpose of the separator is to prevent short circuits caused by Zn dendrite formation and facilitate the transport of hydroxide ions (OH^-) from the air electrode to the Zn electrode. The oxygen reduction reaction (ORR) and oxygen evolution reaction (OER) occur at the air electrode. The following reactions occur in a ZAB during operation (SHE is the standard hydrogen electrode)[5]. The forward and reverse directions show the discharge and charge reactions, respectively.

Zn electrode:

$$\mathrm{Zn} + 4\mathrm{OH^-} \rightleftharpoons \mathrm{Zn(OH)_4^{2-}} + 2\mathrm{e^-} \qquad \mathrm{E^0} = 1.26\ \mathrm{V\ vs.\ SHE} \qquad (2-1)$$

$$\mathrm{Zn(OH)_4^{2-}} \rightleftharpoons \mathrm{ZnO} + \mathrm{H_2O} + 2\mathrm{OH^-} \qquad \mathrm{Zn(OH)_4^{2-}\ decomposes\ to\ ZnO} \qquad (2-2)$$

Air electrode:

$$\mathrm{O_2} + 2\mathrm{H_2O} + 4\mathrm{e^-} \rightleftharpoons 4\mathrm{OH^-} \qquad \mathrm{E^0} = 0.40\ \mathrm{V\ vs.\ SHE} \qquad (2-3)$$

Overall reaction, $(2-1)+(2-2)+(2-3)$:

$$2\mathrm{Zn} + \mathrm{O_2} \rightleftharpoons 2\mathrm{ZnO} \qquad \mathrm{E^0} = 1.66\ \mathrm{V\ vs.\ SHE} \qquad (2-4)$$

Zn oxidizes to Zn^{2+} during discharge at the Zn electrode. Zn^{2+} then combines with OH^- in the electrolyte to form $\mathrm{Zn(OH)_4^{2-}}$. Once the concentration of $\mathrm{Zn(OH)_4^{2-}}$ reaches saturation, $\mathrm{Zn(OH)_4^{2-}}$ begins to decompose into ZnO[5].

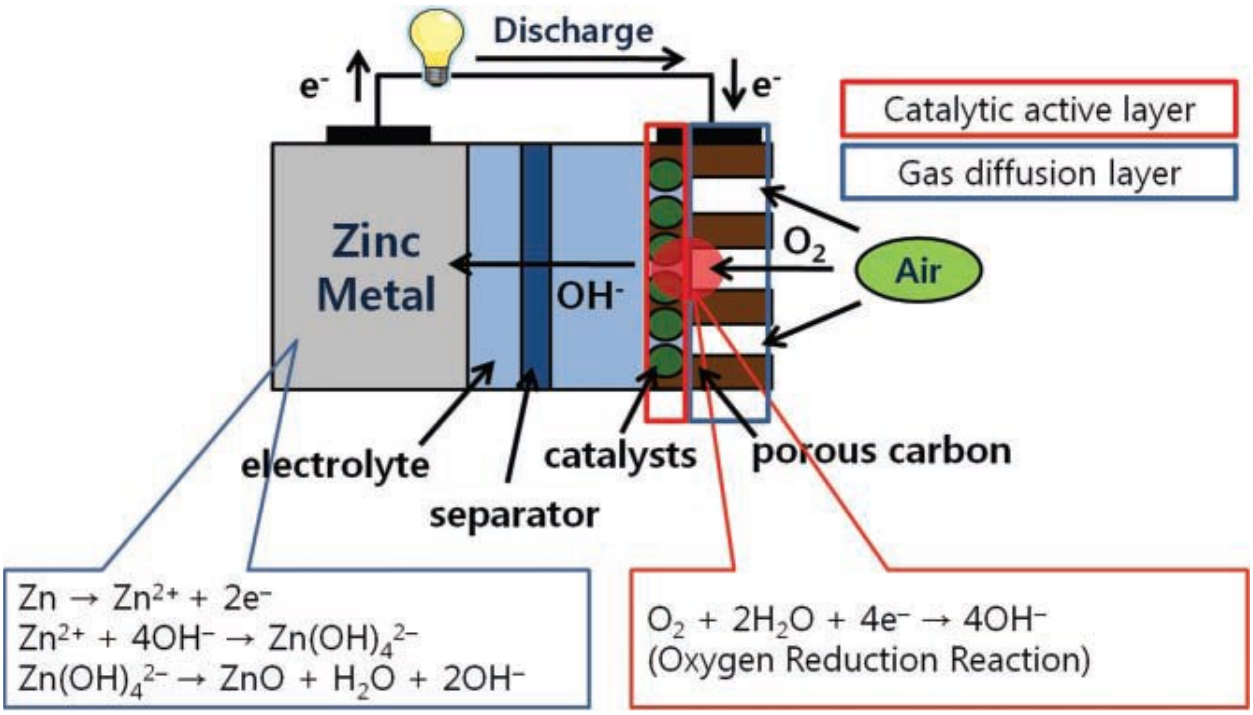

Figure 2.1. Schematic of a typical ZAB setup[11].

2.1.2. Battery Configuration

There are currently 3 main battery configurations used for electrically rechargeable ZABs, each designed for a specific purpose. The planar configuration was first used for primary ZABs with a prioritization in achieving a high energy density. The flow battery was designed to achieve long battery cyclability, whereas flexible batteries are aimed at wearable devices[5].

2.1.2.1. Planar Batteries

A planar arrangement is usually employed for conventional ZABs and the other battery configurations discussed in the following subsections. Figure 2.2 shows a schematic of a prismatic ZAB, which is the most common configuration for rechargeable ZAB research. Researchers use bolts, nuts, and plastic plates to combine the battery components, which allows for quick battery assembly and disassembly. This configuration is also used in larger primary ZABs. Button cells use their cap and casing as current collectors while the prismatic configuration adds current collectors under a plastic casing[5].

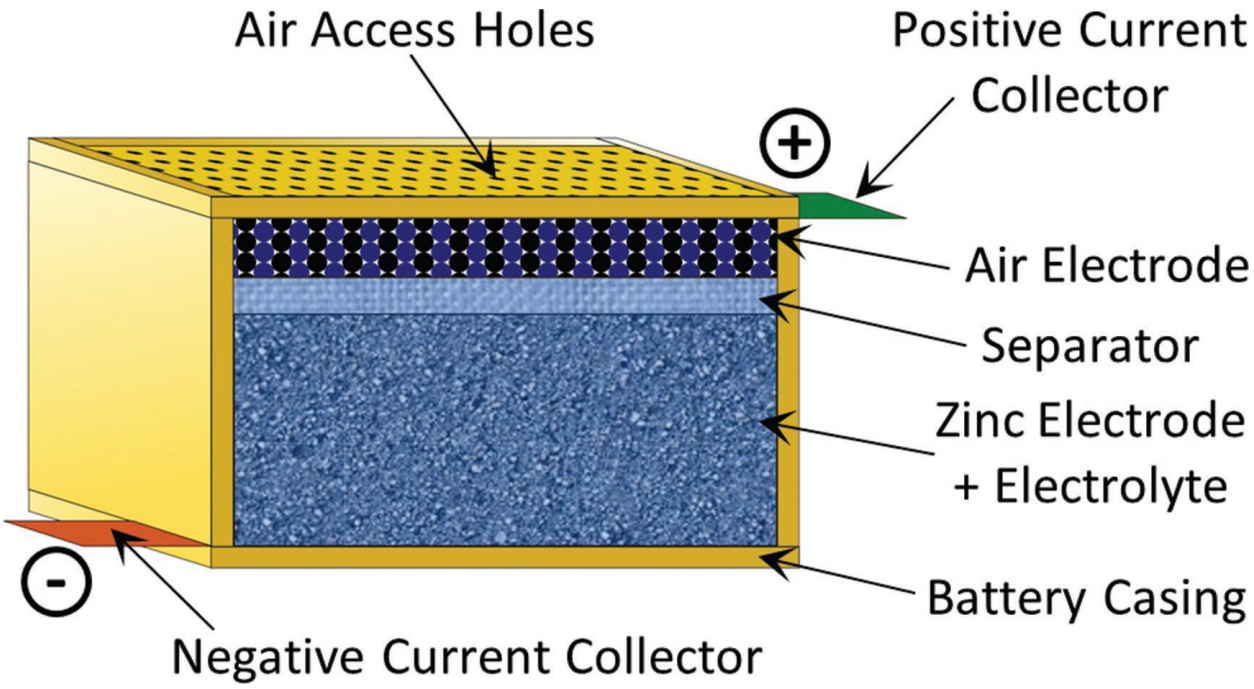

Figure 2.2. Schematic of a prismatic ZAB configuration[5].

2.1.2.2. Flow Batteries

Figure 2.3 shows a schematic of a ZAB with flowing electrolyte. The flowing electrolyte helps improve the battery's performance as well as reduce degradation of the Zn and the air electrode. On the Zn electrode side, the flowing electrolyte helps reduce electrolyte concentration gradients and improve the current distribution. This helps reduce problems of dendrite formation, passivation, and shape change. On the air electrode side, the flowing electrolyte helps wash away precipitated carbonates formed by the reaction between KOH and CO_2 and other undesirable solids, which are eventually excluded by an external filter. Therefore, this configuration should be able to provide better battery performance. On the other hand, in order to distribute flowing electrolyte to the battery, pumps, tubes, and excess electrolyte are needed, which increase the complexity of making the battery and reduce energy efficiency[5].

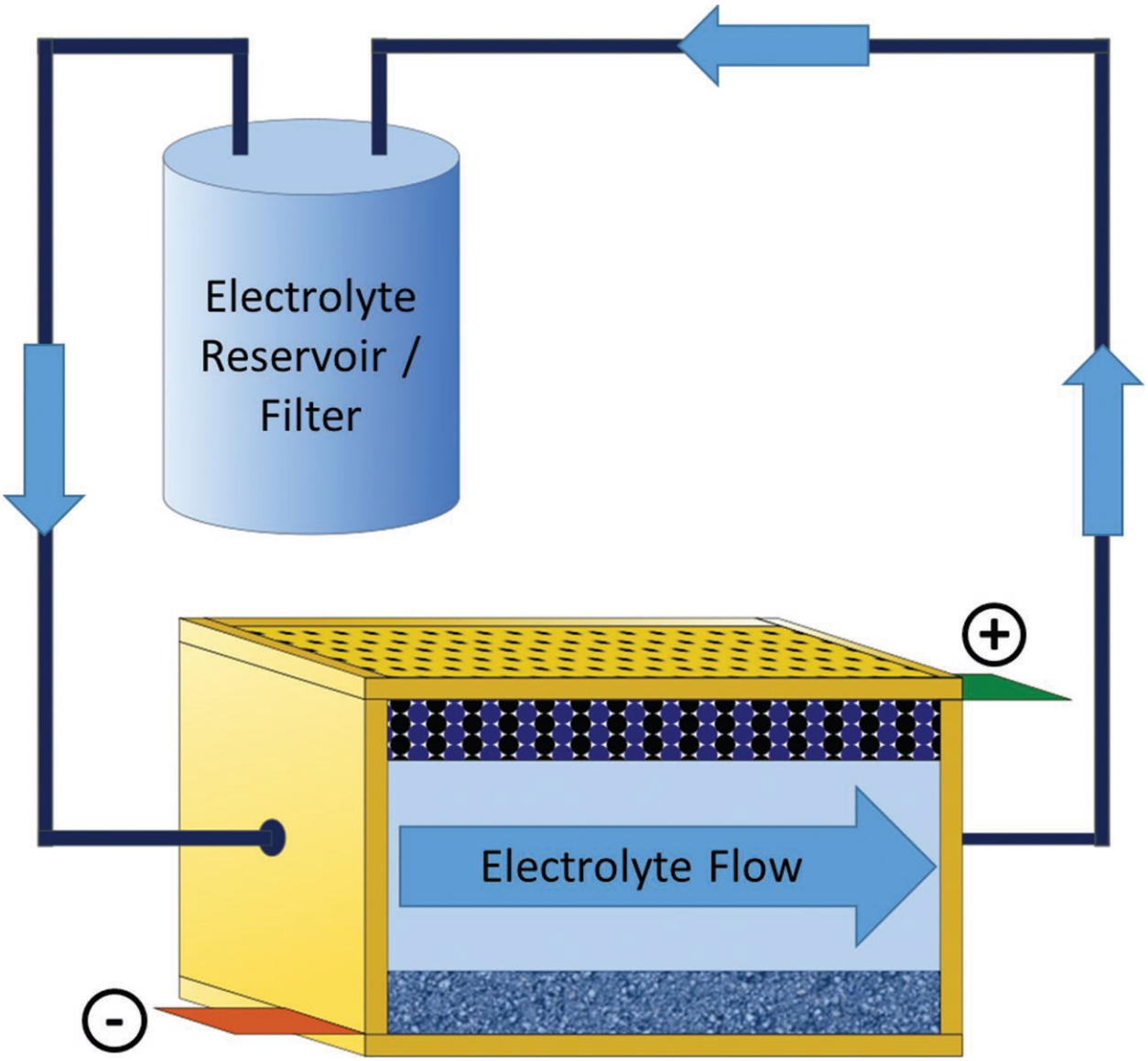

Figure 2.3. Schematic of a ZAB with flowing electrolyte[5].

2.1.2.3. Flexible Batteries

Flexible batteries have gained attention in the last 15 years due to their possible applications in flexible electronics. Figure 2.4 shows a schematic of a flexible ZAB configuration. Solid-state electrolytes should be used in flexible ZABs because aqueous electrolyte in ZABs may evaporate and/or leak onto sensitive electronic equipment due to the semi-open configuration of ZABs. All components in flexible ZABs need to have good mechanical strength in order to withstand deformation[5].

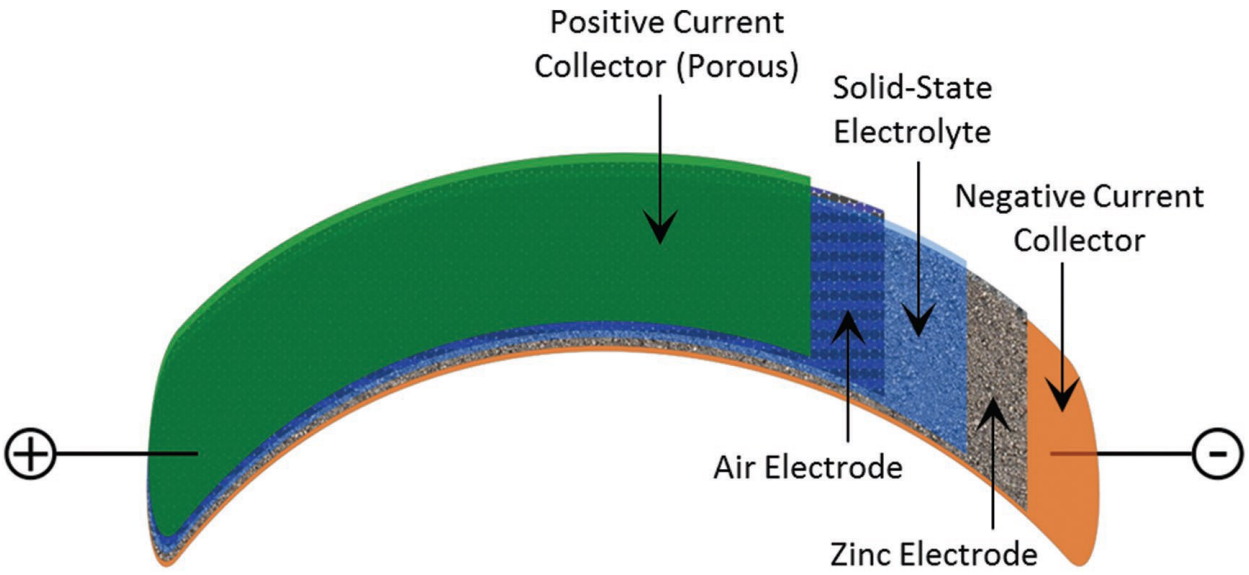

Figure 2.4. Schematic of a flexible ZAB configuration[5].

2.1.2.4. Multi-Cell Configuration

Figure 2.5 shows schematics of multi-cell ZAB configurations. This approach is applicable to situations where the voltage of the battery needs to be increased. Figure 2.5a shows a monopolar arrangement where the air electrode of each cell is externally connected, and the Zn electrode is placed between the air electrodes. To connect each cell in series, one cell's air electrode is externally connected to the adjacent cell's Zn electrode. Figure 2.5b shows a bipolar arrangement where for each cell one side of the Zn electrode is coupled with one air electrode and each cell is connected in series by an electrically conductive bipolar plate with air access channels. The bipolar arrangement is packed more efficiently, and the current is distributed more evenly than in the monopolar arrangement. This is because the bipolar arraignment does not have external wires and the monopolar arrangement collects current from the edges of the electrodes. However, the bipolar arrangement requires a certain amount of pressure to make good contact between each component. The air electrode needs to be entirely electrically conductive which means a pure poly(tetrafluoroethylene) (PTFE) layer cannot be placed on the air-facing side of the air electrode. PTFE is often used to prevent leakage of aqueous electrolyte and helps increase the hydrophobicity of the cell[5].

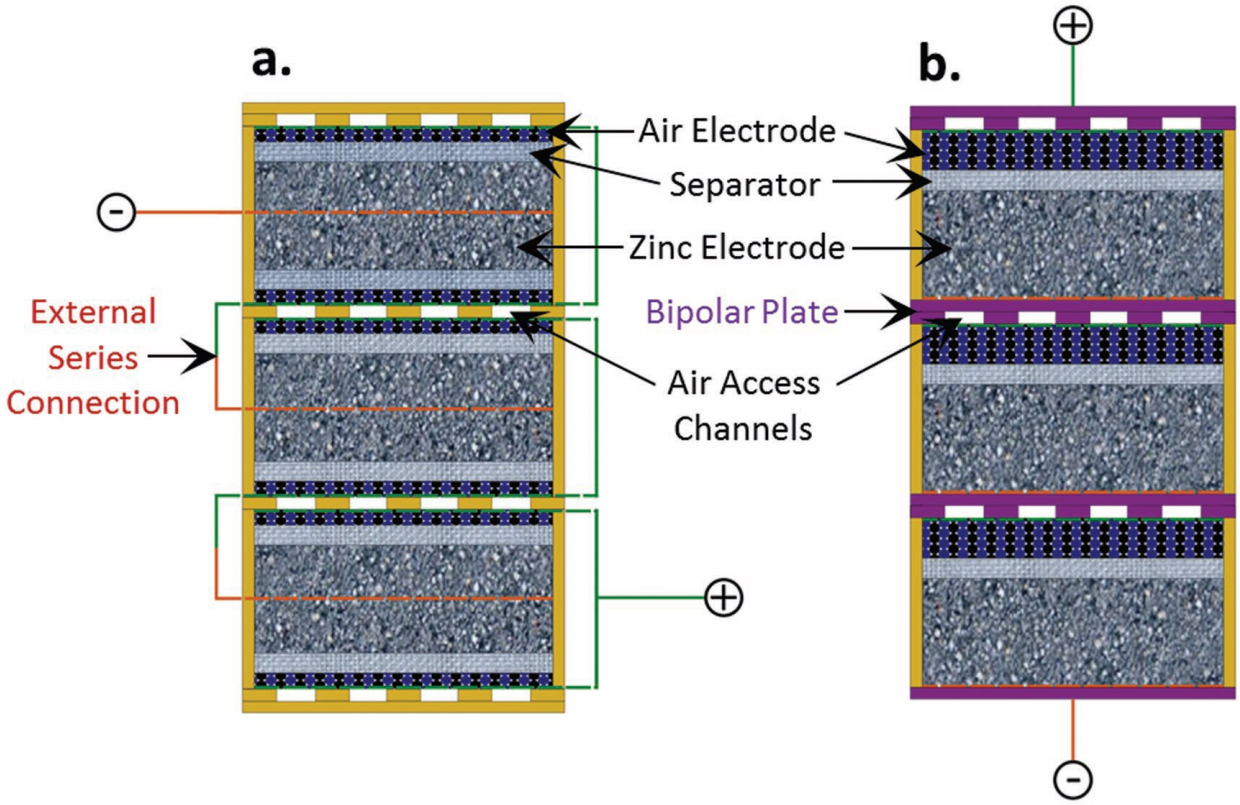

Figure 2.5. Schematics of multi-cell ZABs. a) Monopolar arrangement and b) bipolar arrangement[5].

2.1.3. Challenges for ZABs

While there is research focusing on electrolytes for ZABs, a lot of attention is concentrated on the Zn electrode and the air electrode of ZABs. This is because the relatively poor battery efficiency and long-term cyclability are mainly related to Zn irreversibility and catalytic activity for ORR and OER[7].

2.1.3.1. Challenges with the Zn Electrode

There are four major phenomena that occur during operation in a Zn–air battery which could limit the performance of a Zn electrode: i) dendrite growth (Figure 2.6a), ii) shape change (Figure 2.6b), iii) passivation and internal resistance (Figure 2.6c), and iv) hydrogen evolution (Figure 2.6d)[5].

During electrodeposition, a concentration gradient of $Zn(OH)_4^{2-}$ ions is established as a function of the distance from the Zn electrode surface. $Zn(OH)_4^{2-}$ ions are favorably deposited at areas where the concentration gradient is higher, which will cause dendrite formation over time[12,13].

As shown in Figure 2.6a, dendrite growth on the Zn electrode forms sharp protrusions that can potentially puncture the separator and result in a short circuit between the Zn electrode and the air electrode. In addition, these protrusions may eventually fracture, because of weak adhesion to the Zn electrode, and disconnect from the Zn electrode, leading to capacity losses[5].

Shape change of the Zn electrode is a phenomenon where Zn is dissolved during discharge and redeposited at a different location during charge, which could result in densification of Zn in specific areas and capacity loss. The current distribution on the Zn electrode, uneven reaction zones, and electro-osmotic forces that can cause convective flows within the battery have been found to be responsible for this problem[5].

Passivation occurs when a Zn electrode cannot be further discharged due to the formation of an insulating ZnO film on its surface that blocks migration of the discharge product and/or OH^- ions. As the battery is discharged, $Zn(OH)_4^{2-}$ accumulates and eventually reaches its saturation limit. Upon $Zn(OH)_4^{2-}$ saturation, ZnO begins to precipitate on the electrode surface. In the case of a porous Zn electrode, passivation is preceded by reduction of the pore size due to precipitation of ZnO (which takes up more volume than Zn) and finally occurs when freshly discharged $Zn(OH)_4^{2-}$ is far above the solubility limit, causing it to immediately precipitate and fully plug the remaining pore volume. The failure of a ZAB usually occurs due to passivation of the Zn electrode[5].

The Zn/Zn^{2+} standard reduction potential (-1.26 V vs. SHE at pH 14) is below that of the hydrogen evolution reaction (shown as reaction $(2-5)$) (-0.83 V vs. SHE at pH 14). Therefore, hydrogen evolution is thermodynamically favored and a Zn electrode at rest will go through self-discharge (shown as reaction $(2-6)$). The actual rate of hydrogen evolution on a Zn surface is on the order of 1×10^{-5} mA cm^{-2}. However, the overpotential of hydrogen evolution is significantly decreased on a ZnO surface[5].

$$2H_2O + 2e^- \rightleftharpoons 2OH^- + H_2 \uparrow \qquad (2-5)$$

$$Zn + H_2O \longrightarrow ZnO + H_2 \uparrow \qquad (2-6)$$

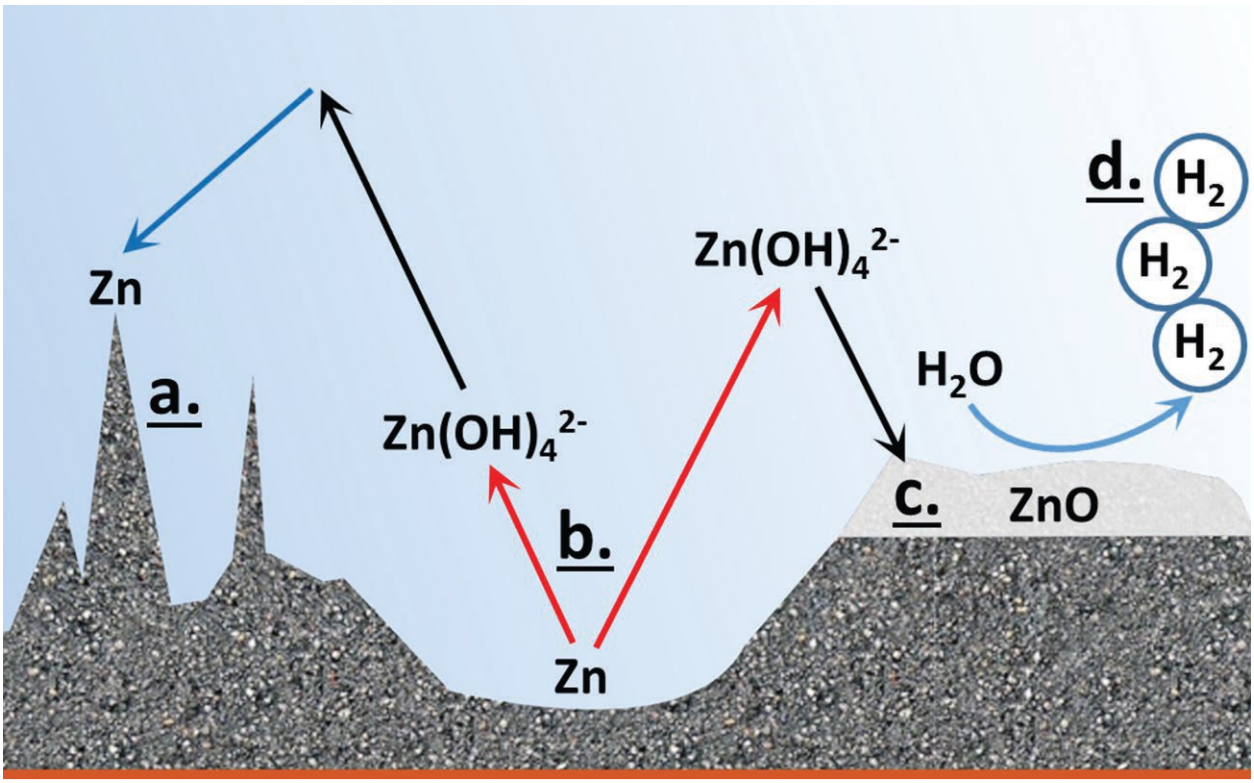

Figure 2.6. Schematic representation of performance-limiting phenomena that may occur on the Zn electrode: a) dendrite growth, b) shape change, c) passivation, and d) hydrogen evolution[5].

2.1.3.2. Challenges for the Air Electrode

A gas diffusion layer (GDL) coated with catalyst is used in a typical ZAB. There are currently two types of commercially available carbon-based GDLs. One is nonwoven carbon paper and the other is woven carbon cloth. Carbon paper GDL is thinner and tends to have lower ohmic resistance and better mass transfer, which should lead to better battery performance. However, carbon paper GDL is quite brittle. On the other hand, the carbon cloth GDL is thicker and more mechanically flexible, which gives it an opportunity to be used in flexible ZABs[5].

The air electrode in ZABs faces problems such as carbon corrosion and electrolyte leakage. In addition, a significant effort is ongoing to find competitive bifunctional catalysts that can be used on the air electrode. The main reason that ZABs have poor battery efficiency is because the kinetics for the ORR and the OER are very sluggish. Therefore, bifunctional catalysts that can boost these reactions are necessary to bring ZABs to a practically usable level. Pt/C (Pt on a carbon black support) has shown excellent performance for the ORR but rather poor performance for the

OER. RuO_2 and IrO_2 exhibit superior performance for the OER but not for the ORR. A combination of Pt/C and RuO_2 has been used as benchmark electrocatalysts for ORR and OER, respectively[5]. However, Pt and Ru are noble metals, which bring concerns of cost and scarcity. Transition-metal-based materials are considered as a way of relieving the concerns as they are more abundant and cost less[14]. However, the stability and long term cyclability of a battery using bifunctional catalysts, as well as the low battery efficiency compared to LIBs, remains problematic[7].

2.2. Electrolytes for ZABs

Electrolytes that are currently used for ZABs can be divided into aqueous electrolytes and non-aqueous electrolytes. Aqueous electrolytes can be further classified into alkaline, neutral, and acidic aqueous electrolytes based on the pH of the solution. Non-aqueous electrolytes include room temperature ionic liquids (RTIL), solid polymer electrolytes and gel polymer electrolytes (GPE)[15].

2.2.1. Aqueous Electrolytes

2.2.1.1. Alkaline Electrolytes

Alkaline electrolytes have been the go-to option for most ZAB research due to their properties of low overpotential and good solubility for Zn, as well as better oxygen reaction kinetics and more electrode material options. KOH, NaOH, and LiOH are reported as candidates for alkaline electrolytes for ZABs. Among them, KOH is more widely used[15] because it has the highest ionic conductivity and good solubility for Zn salts[5]. Figure 2.7 shows the electrolyte ionic conductivity, ZnO solubility, and the Zn/Zn^{2+} exchange current density as a function of KOH concentration. As shown in the figure, 6 M KOH provides the highest ionic conductivity and the Zn/Zn^{2+} exchange current density is quite close to the maximum (at about 8 M), which can support fast electrochemical kinetics and mass transport. Therefore, 6 M KOH is commonly used in ZABs[5]. However, ZABs using alkaline electrolytes suffer from Zn dissolution and the formation of carbonates on the air electrode. On one hand, high solubility of Zn can suppress passivation, while on the other hand, a large amount of Zn is expected to dissolve during discharge and redeposit during charge. During this process, dendrite formation and shape change, as described in 2.1.3.1. Challenges with the Zn Electrode, can occur. KOH and CO_2 can react and produce insoluble

carbonates, which could reduce the ionic conductivity of the electrolyte and block the pores on the air electrode and limit the air access[5,15].

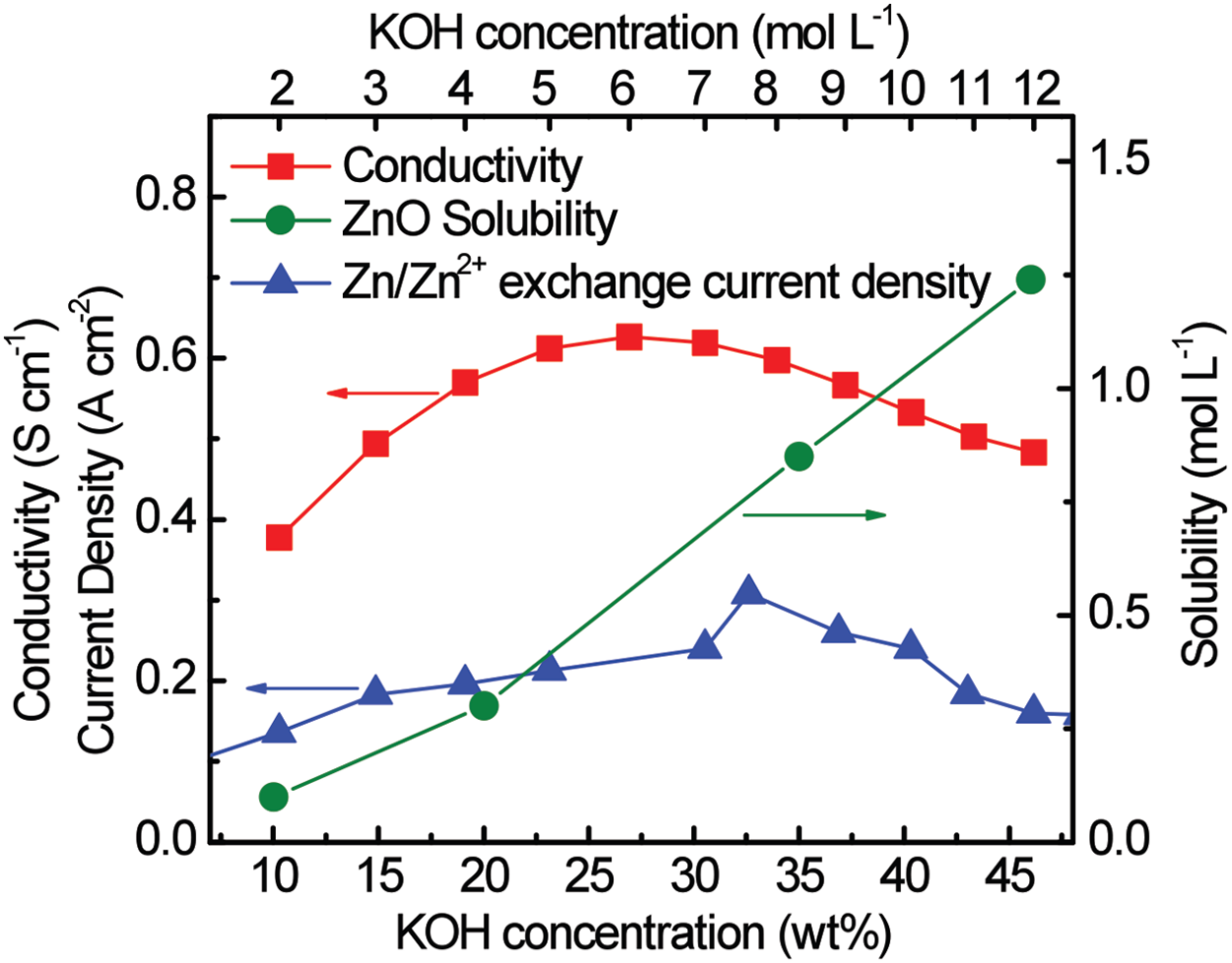

Figure 2.7. Electrolyte ionic conductivity, ZnO solubility, Zn/Zn^{2+} exchange current density as a function of KOH concentration[5].

2.2.1.2. Neutral Electrolytes

Using a neutral electrolyte in a ZAB can prevent the formation of carbonates as well as minimize the problem of dendrite formation on the Zn electrode. This is because the solubility of Zn in an electrolyte with neutral pH is lower than that of an alkaline electrolyte and the absorption of CO_2 is greatly reduced. With a change in electrolyte pH, there is a change in the reactions with the Zn electrode. The reactions on the Zn electrode in an alkaline electrolyte are shown below.

$$Zn + 4OH^- \rightleftharpoons Zn(OH)_4^{2-} + 2e^- \qquad E^0 = 1.26\ V\ vs.\ SHE \qquad (2-1)$$

$$Zn(OH)_4^{2-} \rightleftharpoons ZnO + H_2O + 2OH^- \qquad Zn(OH)_4^{2-}\ decomposes\ to\ ZnO \qquad (2-2)$$

In a neutral electrolyte, the following reactions occur on the Zn electrode in a ZAB[13,14].

$$Zn + H_2O \rightleftharpoons ZnOH + H^+ + e^- \qquad (2-7)$$

$$ZnOH \rightleftharpoons ZnO + H^+ + e^- \qquad (2-8)$$

$$ZnO + H_2O \longrightarrow Zn^{2+} + 2OH^- \qquad (2-9)$$

$ZnCl_2$, $ZnSO_4$, $Zn(AC)_2$, and organic aqueous solvents have been investigated as candidates for neutral electrolytes in ZABs. However, when $ZnCl_2$ is used, chlorine evolution can happen during battery operation and affect battery efficiency. Also, in a neutral electrolyte, common electrocatalysts used for ZABs in an alkaline environment do not perform well. Zn electrodes developed for neutral electrolytes are rare. Even though the reduced solubility of Zn in a neutral electrolyte greatly reduces dendrite formation, reaction kinetics on the Zn electrode are very slow. In summary, the development of neutral electrolytes for ZABs is still at an early stage[16].

2.2.1.3. Acidic Electrolytes

ZABs using acidic electrolytes are rarely reported due to the lack of suitable electrode materials and catalysts. ZABs utilizing acidic electrolytes do not experience the formation of carbonates. However, in an acidic environment, the Zn electrode undergoes severe hydrogen evolution[15,17].

2.2.2. Non-Aqueous Electrolytes

2.2.2.1. Room Temperature Ionic Liquids

Room temperature ionic liquids (RTILs) are molten salts with a melting temperature lower than 100℃. RTILs are composed of an organic cation and an inorganic/organic anion[5]. Based on how cations and anions are paired, ILs can be classified into aprotic, protic and zwitterionic ILs[18]. Aprotic ILs, based on organic cations, have difficulty in packing large irregular cations with small anions. The transfer of a proton from a Brönsted acid to a Brönsted base (usually an amine) occurs in protic ILs. In zwitterionic ILs, cations and anions are tethered in an intramolecular form, which could inhibit migration of the IL component[19].

RTILs have the advantages of a large electrochemical window, nonflammability, and good thermal stability. In addition, utilization of RTILs in ZABs can eliminate Zn corrosion, electrolyte evaporation, and the formation of carbonates. However, compared with traditional aqueous electrolytes, RTILs have a relatively higher viscosity and lower ionic conductivity, which limit the performance at high current densities. In addition, the difficulty in the synthesis of RTILs, as well as their high price, restrict their applications in ZABs[5,15,18].

2.2.2.2. Solid Polymer Electrolytes

Solid polymer electrolytes (SPEs) are ionic conductive solids that contain heteroatoms and allow diffusion and dissolution of salts when an electric field is applied. SPEs eliminate problems such as electrolyte leakage that aqueous electrolytes face. However, the low solubility of salts, as well as low ionic conductivity, limit the application of SPEs in batteries[15].

2.2.2.3. Gel Polymer Electrolytes

The difference between gel polymer electrolytes (GPEs) and SPEs is that a liquid electrolyte is retained in the polymer gel, whereas SPEs do not have liquid added[18]. The addition of a liquid electrolyte to the polymer improves the ionic conductivity while maintaining the advantages of SPEs. GPEs can act as a separator in the battery and, therefore, can prevent short circuits caused by dendrite formation[5]. In addition, the fast development of flexible and wearable electronics demands flexible and mechanically reliable batteries. GPEs have crosslinked hydrophilic polymer chains dispersed in water which allow the toughness and mechanical strength of the GPE to be adjusted so that even when it is under severe deformation, the GPE can still provide good performance[20].

In solid electrolytes, dissolved ions are confined in the polymer matrix and, therefore, their movements are hindered, which leads to reduced ionic conductivity. To provide sufficient ionic conductivity and fast reaction kinetics for OER and ORR, high water content in the GPE is vital. High-water content is useful for dissolving hydroxide ions and movement of polymer chains[21]. As such, the host polymers used for GPEs need to have sufficient hydrophilicity[22]. To prepare solid electrolytes, 3 types of materials can be used as the framework materials: synthetic polymers, biomass materials, and inorganic materials. Table 2.1 shows examples for each type of material. In addition to selecting the optimum host material, strategies such as regulating OH^- content,

adding fillers, and adding other hydrophilic materials, can be used to further improve the ionic conductivity of the electrolytes[23].

Table 2.1. Examples of framework materials for the preparation of solid electrolytes

Type of materials	Examples
Synthetic polymers	Polyethylene oxide (PEO), polyvinyl alcohol (PVA), polyacrylic acid (PAA), polyacrylamide (PAM)
Biomass materials	Cellulose, starch, chitosan, agar, gelatin, protein
Inorganic materials	TiO_2, SiO_2, ZrO_2, zeolite, graphene oxide (GO), layered double hydroxide

ZABs using GPEs may also experience poor battery performance caused by water loss of the electrolyte and increased electrolyte – electrode interfacial resistance. Since ZABs have a semi-open structure, water can evaporate through the pores of the air electrode. Approaches such as introduction of sealing films with breathing holes and the addition of hydrophilic materials such as PAA, PAM, cellulose, GO and SiO_2 can be used to reduce water loss from the electrolyte[23]. One drawback of using a GPE in a ZAB, instead of an aqueous electrolyte, is that utilization of the surface area of the air electrode for GPEs is restricted due to reduced fluidity. In addition, the wettability of GPEs to the air electrode is worse than that of aqueous electrolytes, which leads to higher interfacial resistance and higher overpotentials[5]. To mediate this problem, adjusting the hydrophobicity/hydrophilicity of the electrolyte-electrode interface may improve electron and mass transmission[23].

Freezing of GPEs at sub-zero temperatures can severely limit their practical applications, as the working temperature range of electronics is expected to extend to sub-zero temperatures[20]. The formation of ice is a result of aggregation of water molecules linked by hydrogen bonded networks[24]. Therefore, disrupting the formation of hydrogen bonds between water molecules may decrease the freezing point of the GPE. The methods of decreasing the freezing point of GPEs include adding salts (e.g., $CaCl_2$, NaCl, $ZnCl_2$ and their mixtures) to the GPE during synthesis.

This method utilizes the colligative property of ionic compounds, which decreases the freezing temperature of water due to ion hydration. The second method is adding organic solvents (e.g., glycerol, n-decane, silicone oil, ethylene glycol, paraffin, sorbitol, and glycol) to GPEs. Organic solvents form hydrogen bonds with water molecules and compete with the hydrogen bonds formed between water molecules. These organic solvents make it harder to form hydrogen bonds between water molecules, thereby disrupting hydrogen bond formation between water molecules. However, there is a trade-off between the anti-freezing ability and ionic conductivity of the electrolyte. When more organic solvents are added, the electrolyte can operate at lower temperatures, but the ionic conductivity will be significantly reduced at the same time[20,25]. Moreover, synthesizing GPEs with ethylene glycol requires complex and costly procedures that may be harmful to the environment[26]. Typical ZABs use 6-7 M KOH to achieve the maximum ionic conductivity[5]. Figure 2.8 shows the phase diagram for the KOH - H_2O system. The amount of K corresponding to a 6 M KOH aqueous solution is about 3.5 at% (detailed calculations are shown in section 3.5.1. Calculation Details). The corresponding freezing point at this concentration is about $-50℃$, which should be sufficient for the majority of battery applications.

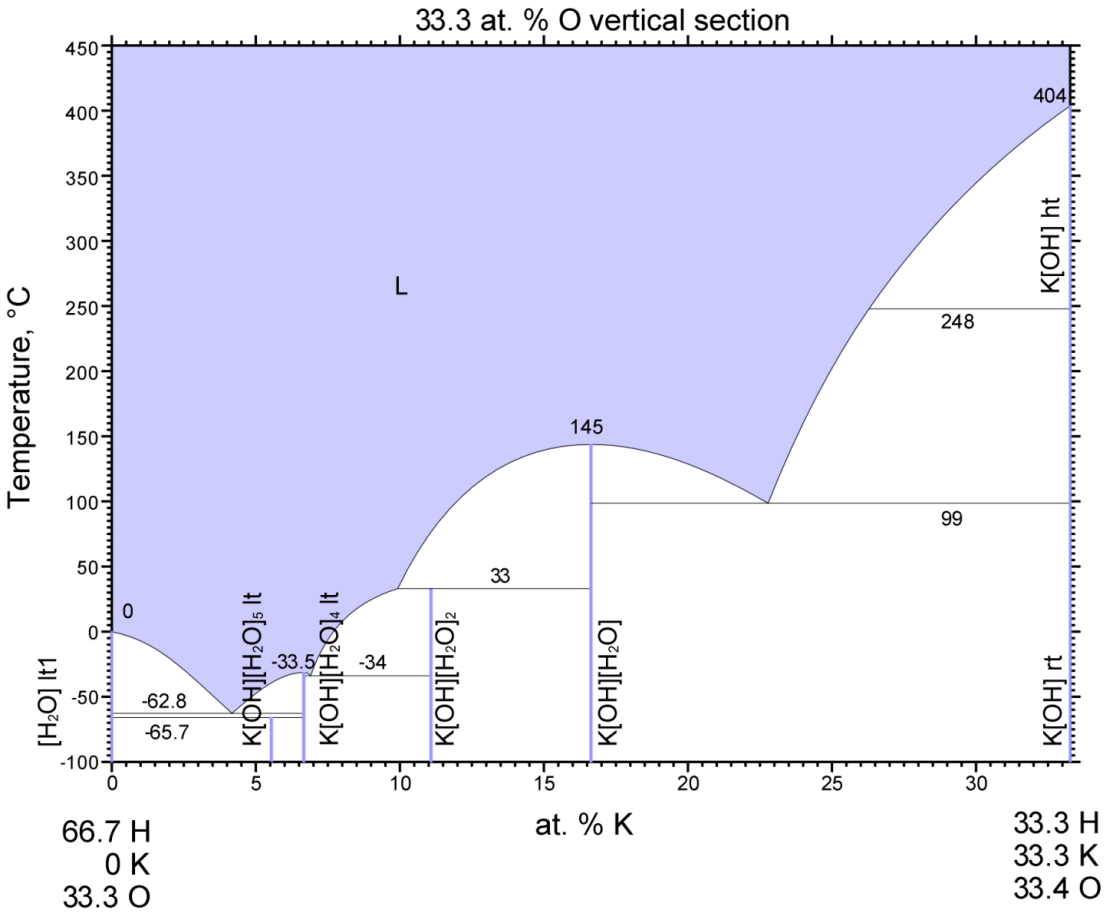

Figure 2.8. Phase diagram for the KOH - H_2O system[27].

Pei et al. synthesised a GPE that works in a ZAB at temperatures as cold as $-36℃$ by adjusting the concentration of KOH. In their study, a desirable polymer host system was determined by calculating the interaction energy between the polymer and water molecules. A larger absolute value of the interaction energy means stronger bonds between the polymer and water molecules. PAA was chosen as the polymer host system and the polymer was pre-neutralized using NaOH to increase the osmotic pressure in the polymer matrix as well as to help maintain the polymer's structure when it is exposed to concentrated alkaline solution. KOH was then added to the GPE during the synthesis step to improve its low temperature tolerance[28]. Tran et al. studied PVA, PAA, and PAM as host polymers for GPEs in ZABs. Their structures as well as polymer states in deionized water (DIW) and 6 M KOH solution are shown in Figure 2.9. Among these polymers, the GPE using PAA with 6 M KOH demonstrated the highest ionic conductivity and the best initial discharge-charge efficiency[29]. Therefore, PAA was selected as the host polymer in this

study due to the reasons mentioned above. Tran et al. then further studied the effects of different cell configurations, as well as concentrations of ZnO additive[8,10], crosslinker[30], and PAA[8], on battery performance. A single air electrode (SAE) battery design was compared with a double air electrode (DAE) design. The SAE cell design is more preferred as the DAE design adds complexity to the battery and the extra weight added reduces the specific energy of the battery. The addition of ZnO to the electrolyte improves the cyclability of the battery but a large amount of ZnO may lead to early passivation of Zn[8]. It was assumed that a larger amount of crosslinker and PAA will lead to a smaller mesh size between polymetric networks which could affect the mobility of large ions such as $Zn(OH)_4^{2-}$ (i.e., zincate ion)[8,30]. Furthermore, when a larger amount of crosslinker is used, the polymer structure becomes denser, which causes a decrease in network void that can retain water. Water retention ability of the GPE is, therefore, reduced[30]. A less adhesive GPE will allow bubbles to better coalesce and escape. As such, the concentration of PAA should be as low as possible. The optimum concentrations of KOH, AA, ZnO, N,N'-methylenebisacrylamide (MBAA) and $K_2S_2O_8$ (KPS) in the GPE determined by Tran et al. are 6.5 M, 0.5 M, 0.25 M, 0.03 M and 0.0015 M, respectively[8].

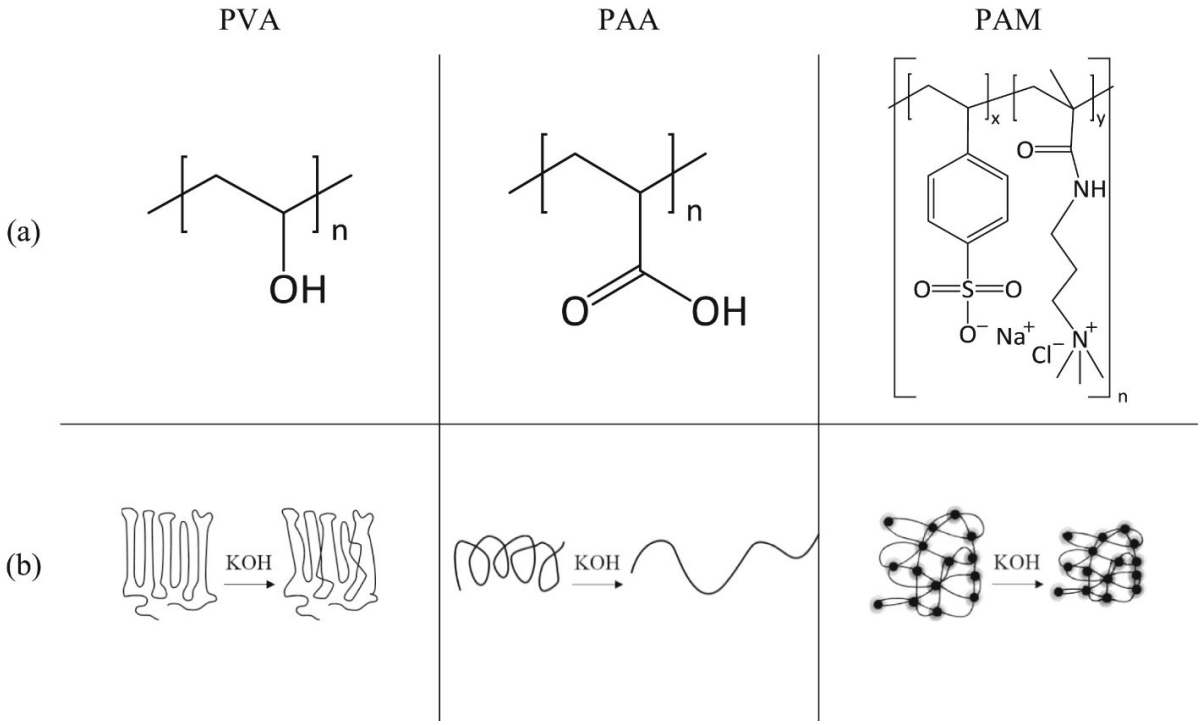

Figure 2.9. (a) Molecular structures of PVA, PAA and PAA and (b) polymer states in DIW and 6 M KOH solution[29].

2.3. Characterization Techniques

Various characterization techniques are used in this work to study the performance of the battery and characteristics of the materials and the GPEs used in the batteries.

2.3.1. Electrochemical Testing

2.3.1.1. Galvanodynamic Polarization

Galvanodynamic polarization is a technique that is used to measure the response of potential and how much it deviates from the open circuit voltage (OCV) as current changes. Figure 2.10 shows an example of the result obtained using the galvanodynamic polarization technique. The black, brown, blue, and red solid lines represent the discharge polarization curve, charge polarization curve, power density of the battery and battery efficiency, respectively. To obtain the charge and discharge polarization curves, positive (charging) and negative (discharging) currents are applied to the battery electrodes with currents increasing gradually. Then, the response of potential is recorded and plotted as a function of current. Three polarization regions are identified with dashed lines and letters in the figure. There is a drop of voltage at the start of the test, which is caused by the energy barrier for electron transfer reactions, known as activation polarization. As the test continues, ohmic polarization starts to dominate the additional voltage losses. Ohmic polarization is mainly caused by the internal resistance of the electrolyte to ion flow as well as the interfacial resistance between the electrodes and electrolyte. The sudden drop of voltage at the end of the test is attributed to mass transfer polarization which is caused by limited mass transfer of the reactants. The power density of the battery is calculated by multiplying the discharge voltage and the current density. Energy efficiency is calculated using the discharge voltage divided by the charge voltage[5].

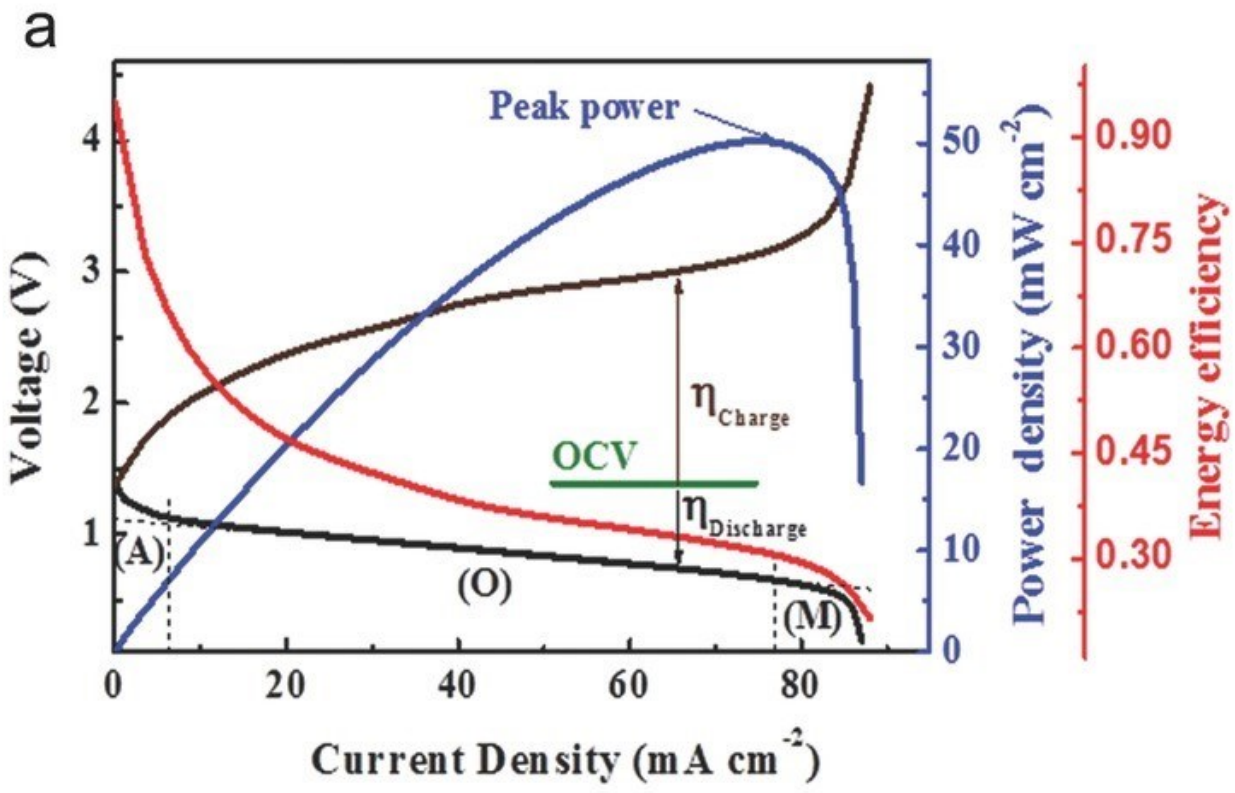

Figure 2.10. An example of typical charge and discharge polarization curves, power density curves, and energy efficiency for rechargeable ZABs, plotted in brown, black, blue and red solid lines, respectively. The black dashed lines identify activation (A), ohmic (O), and mass transfer (M) polarization regions on the discharge polarization curve[5].

2.3.1.3. Galvanostatic Charge – Discharge

Galvanostatic charge – discharge (GCD) is a common technique used in battery research which investigates the stability and durability of the battery[5,31,32]. One way to run this test is to test the battery in a cyclic manner where a constant current is chosen and the battery is discharged and charged alternately for a specific amount of time and cycles, with discharging and charging voltages recorded[5]. Initial and final battery efficiencies can be calculated from this test, which in turn reveals the stability of the battery. The number of cycles at which the battery can operate provides information on the durability of the battery. Another way is to discharge and charge the battery with various current densities for a specific amount of time. Battery efficiencies for each current density can be calculated in the same manner. The response of voltage at each current density provides information about the stability of the battery at the corresponding current density

for a certain amount of time. Examples of both tests are shown in Figure 2.11. Figure 2.11a shows GCD curves for ZABs using GPEs at various current densities. Figure 2.11b shows a GCD test run in a cyclic manner with 30 min per cycle.

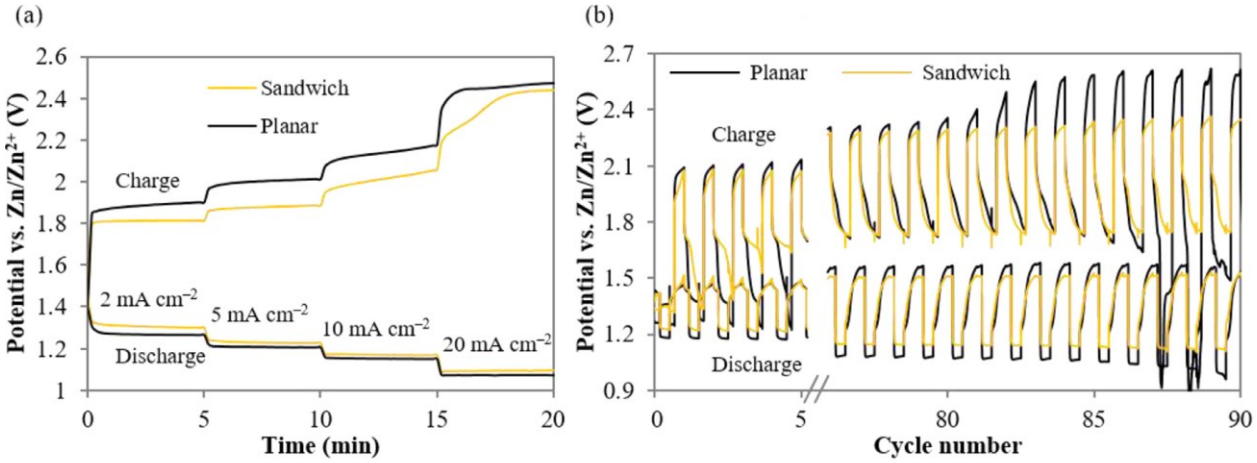

Figure 2.11. GCD testing for ZABs using GPEs (PAA as the host polymer) with different cell configurations: a) At various current densities and b) at a current density of 5 mA cm^{-2} in a cyclic manner[10].

2.3.1.4. Cyclic Voltammetry and Linear Sweep Voltammetry

Cycling voltammetry (CV) and linear sweep voltammetry (LSV) are powerful and popular electrochemical techniques that are used to study electrode reaction mechanisms[33,34]. In a CV measurement, terminal voltages (E_1 and E_2) as well as scan rate (ν) are specified. The test starts from one terminal voltage (E_1) with the voltage varying linearly with time and the resulting current recorded. Once the other terminal voltage (E_2) is reached, the scan direction is reversed and the potential is swept back to E_1[35]. This process can be repeated for multiple cycles, depending on what information desired[36]. Figure 2.12 shows a typical cyclic voltammogram for a reversible redox process. It is assumed that the system is originally in the oxidized state (O). There are two peaks in the figure. The cathodic peak is a reduction peak, corresponding to a reduction reaction of $O \longrightarrow R$. The anodic peak corresponds to an oxidation reaction of $R \longrightarrow O$. From these two peaks, peak currents as well as the peak positions can be determined. The peak current (Equation $(2-10)$) increases with the square root of the scan rate and is directly proportional to concentration. The peak positions are related to the formal potentials (Equation $(2-11)$) of the

redox process. The separation of peak potentials (Equation $(2-12)$) can be utilized to determine the number of electrons transferred.

$$i_p = (2.69 \times 10^5) n^{1.5} A C D^{0.5} \nu^{0.5} \qquad (2-10)$$

$$E^o = \frac{E_{p,a} + E_{p,c}}{2} \qquad (2-11)$$

$$\Delta E_p = E_{p,a} - E_{p,c} = \frac{0.059}{n}\ V \qquad (2-12)$$

where i_p is peak current for a reversible couple at 25℃, n is the number of electrons, A is the electrode area in cm^2, C is the concentration in mol cm^{-3}, D is the diffusion coefficient in $cm^2\ s^{-1}$, ν is the potential scan rate in V s^{-1}, E^o is the formal potential of the redox process, $E_{p,a}$ is the potential of the anodic peak, $E_{p,c}$ is the potential of the cathodic peak, and ΔE_p is the separation between the peak potentials for a reversible couple[36].

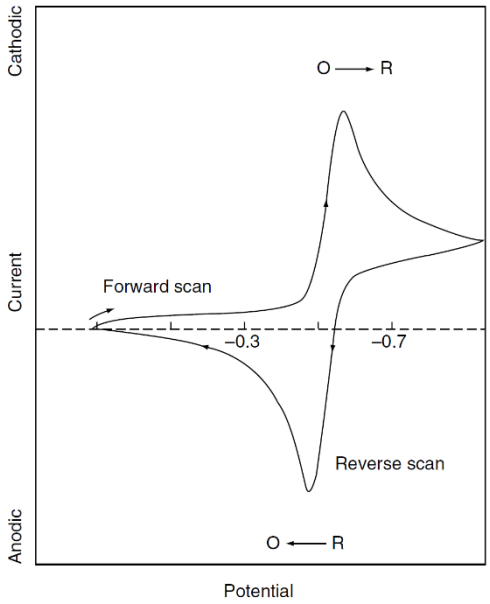

Figure 2.12. Schematic of a typical cyclic voltammogram for a reversible redox process[36].

Figure 2.13 shows cyclic voltammograms for irreversible (curve A) and quasi-reversible (curve B) redox processes. Cyclic voltammograms for irreversible and quasi-reversible processes are different than those of reversible processes. For irreversible processes, the peaks are widely separated and reduced in size. The peak current (i_p) and peak potential (E_p) are characterized by Equation $(2-13)$ and $(2-14)$, respectively. i_p is still proportional to the bulk concentration but the height is lower compared with the peak height of a reversible redox process. In an irreversible system, the peak potential and the half-peak potential at 25℃ will differ by $\frac{48}{\alpha n}$ mV. Therefore, as αn decreases, the shape of the voltammogram becomes wider[35].

$$i_p = n(2.99 \times 10^5)(\alpha n_a)^{0.5} A C D^{0.5} \nu^{0.5} \qquad (2-13)$$

$$E_p = E^o - \frac{RT}{\alpha n_a F}\left[0.78 - \ln\frac{k^o}{D^{0.5}} + \ln\left(\frac{\alpha n_a F \nu}{RT}\right)^{0.5}\right] \qquad (2-14)$$

where n_a is the number of electrons involved in the charge transfer step, n is the number of electrons, α is the transfer coefficient, A is the electrode area in cm^2, C is the concentration in mol cm^{-3}, D is the diffusion coefficient in $cm^2\ s^{-1}$, ν is the potential scan rate in $V\ s^{-1}$, E^o is the formal

potential of the redox process, k^o is the standard rate constant in cm s^{-1}, F is the Faraday constant, R is the gas constant, and T is the temperature in Kelvin[36].

Compared with reversible processes, quasi-reversible processes show larger separations in peak potentials. In quasi-reversible systems with $10^{-1} > k^o > 10^{-5}$ cm s^{-1}, the shape of the voltammogram is a function of $\frac{k^o}{\sqrt{\pi a D}}$, where $a = \frac{nF\nu}{RT}$. When the scan rate is fast, the system shows irreversible behavior, whereas when $\frac{k^o}{\sqrt{\pi a D}}$ is large the process behaves similar to a reversible process[36].

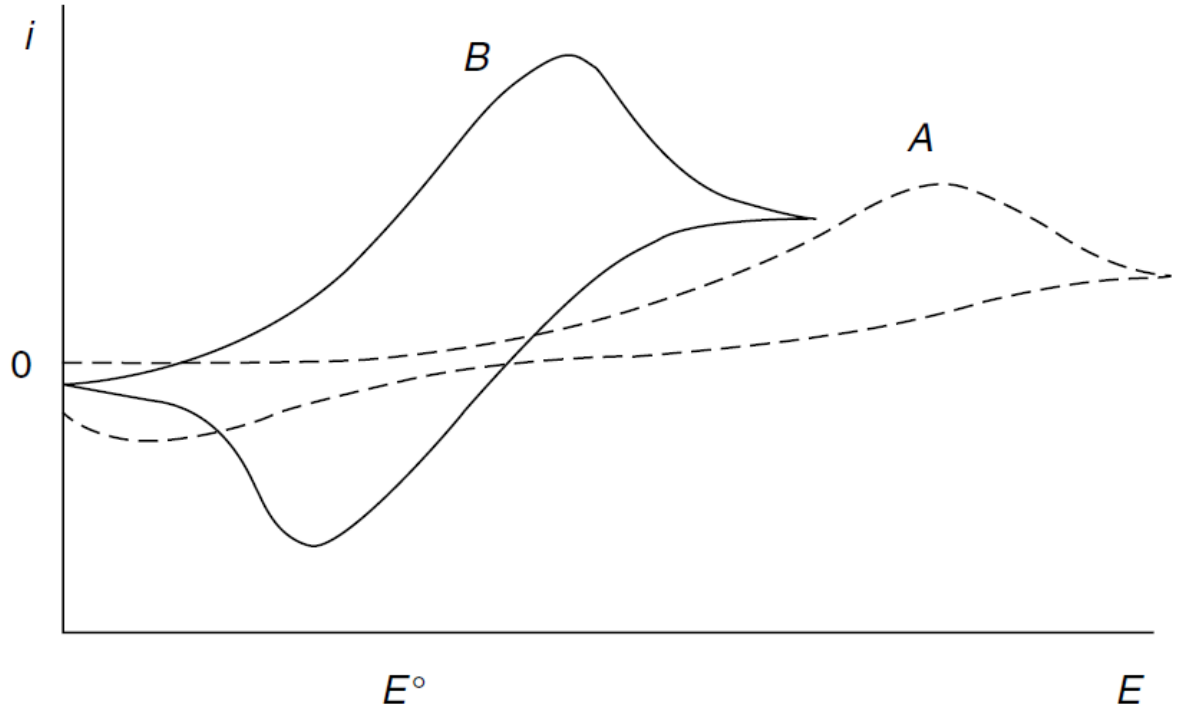

Figure 2.13. Schematic of cyclic voltammograms for irreversible (curve A) and quasi-reversible (curve B) redox processes[36].

LSV and CV can both be used to study electron transfer reactions. CV is a reversal technique where two terminal voltages are determined, whereas in a LSV measurement, only one terminal voltage is determined[34]. In a LSV experiment, the potential is varied linearly with time

with the corresponding current recorded. The potential sweep rate can range from 10 mV s^{-1} to 1000 V s^{-1} with conventional electrodes[33]. Examples of LSV curves are shown in Figure 2.14.

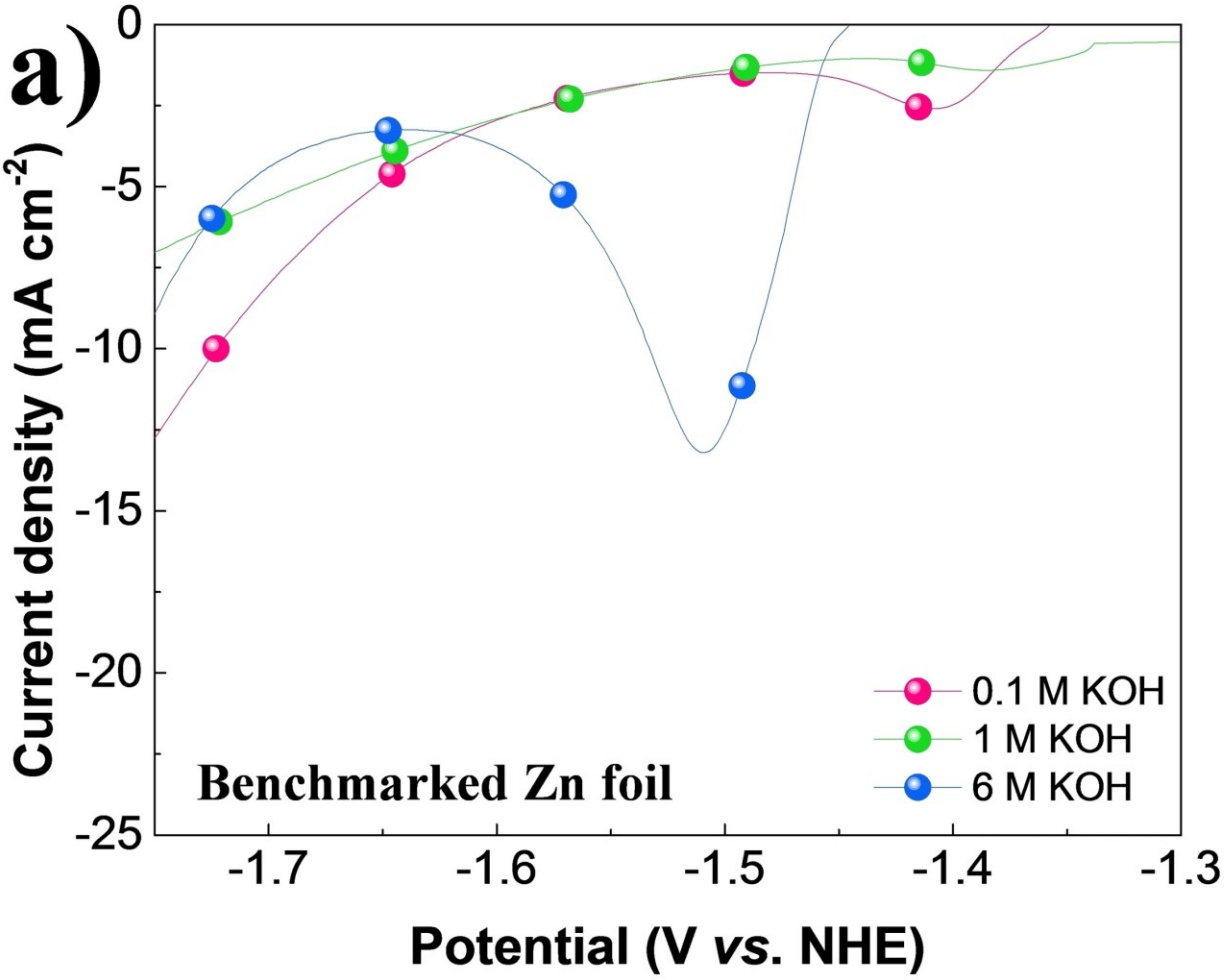

Figure 2.14. Examples of LSV measurements on Zn foils using different concentrations of KOH[37].

2.3.1.5. Electrochemical Impedance Spectroscopy

Electrochemical impedance spectroscopy (EIS) is an AC technique where an applied potential is varied over time at a certain frequency with a predetermined amplitude. The collected data can be plotted in various ways, but the most important plot is the Nyquist plot[38]. Figure 2.15 shows typical Nyquist plots for full cell testing and ionic conductivity testing.

EIS can be used to reveal charge transfer resistance (R_{ct}), interfacial resistance (R_{int}), electrolyte resistance (R_s), and bulk resistance of a ZAB, which can further be used to analyze the limiting factors (e.g., limitations by catalyst or electrolyte) of a ZAB. Overall, a smaller R_{ct}

implies better catalytic activity. Smaller R_{int} and R_s values imply better electrolyte-electrode contact and lower internal resistance from the electrolyte, respectively[5]. Among all these parameters, the interfacial resistance is of most interest for ZABs using a GPE since the wettability of GPEs is usually worse than for aqueous electrolytes and may cause poorer battery performance[27]. In addition, a combination of EIS and Equation $(2-15)$ can be used to determine the ionic conductivity of a GPE. A coin cell is needed to measure the ionic conductivity of a GPE. σ is the ionic conductivity of the GPE, L is the thickness of the GPE, and R and A are the bulk resistance and the contact area of the GPE within the coin cell[29].

$$\sigma = \frac{L}{R \times A} \qquad (2-15)$$

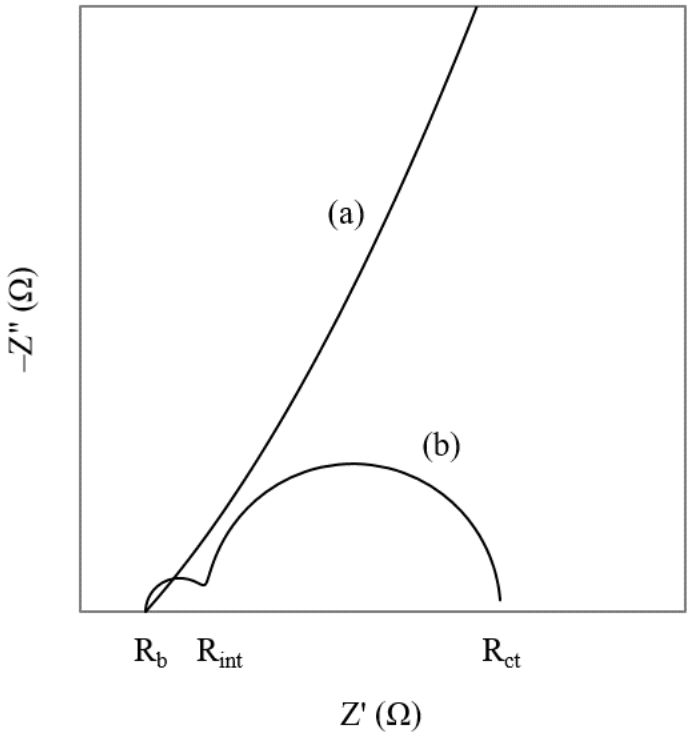

Figure 2.15. Schematic of Nyquist plots for EIS data: a) Ionic conductivity of the electrolyte and b) full cell testing[39].

2.3.2. Scanning Electron Microscopy and Energy Dispersive X-ray Spectroscopy

Scanning electron microscopy (SEM) can be used to study the microstructures of the Zn electrode and air electrode before and after battery tests. A combination of SEM and energy

dispersive X-ray spectroscopy (EDX) are used to perform quantitative or semi-quantitative elemental analysis on samples of interest[40].

To perform SEM analysis on a sample, a focused beam of electrons is generated by an electron source in a scanning electron microscope. After being accelerated to a desired energy and modified by components of the microscope (e.g., apertures and magnetic and/or electrostatic lenses, to reduce the beam diameter), the beam is scanned across the surface of the specimen, generating two types of electrons, backscattered electrons (BSEs) and secondary electrons (SEs). BSEs are beam electrons that have experienced scattering and deflection caused by the electric fields of the atoms in the specimen but still manage to emerge from the specimen with most of the incident energy intact. SEs are electrons that escape the specimen surface with energy smaller than 50 eV. BSEs can be used to provide information on specimen composition, surface inclination, and crystallography. SEs are useful for studying the topography of the specimen[40].

Two types of X-rays can be produced when energetic electrons interact with the specimen atoms. One is characteristic X-rays and the other one is continuum or background X-rays. The production of characteristic X-rays is due to inner shell ionizations. A beam electron with high energy (more than a critical amount) knocks out an inner shell electron (e.g., K-shell). The inner shell electron is then ejected from the atom and creates a hole in the inner shell, making the atom unstable/ionized. An electron from a higher energy shell (e.g., L-shell) fills the vacancy and energy is released. The energy can be given off in the form of an X-ray or an Auger electron. If an X-ray is released, the X-ray is called a characteristic X-ray because its energy or wavelength is characteristic of the element that produces it. This feature allows researchers to perform qualitative or even quantitative elemental analysis of the specimen[40].

Continuum X-rays, also known as Bremsstrahlung X-rays, form a background beneath any characteristic X-rays, which affects the measurement accuracy. Continuum X-rays can be produced during the inelastic interaction of the nucleus of the atom with the beam electron[40].

2.3.3. Rheological Measurements

Rheology is the study of the deformation and flow of materials[41]. The complex modulus (G^*) (expressed in Equation $(2-16)$), storage modulus (G') (expressed in Equation$(2-17)$),

and loss modulus (G'') (expressed in Equation$(2-18)$) are the resistance of a material to deform, the elastic energy, and the viscous energy, respectively[42].

$$G^* = \frac{\tau_0}{\gamma_0} = \sqrt{(G')^2 + (G'')^2} \qquad (2-16)$$

$$G' = \frac{\tau_0}{\gamma_0}\cos\delta = G^*\cos\delta \qquad (2-17)$$

$$G'' = \frac{\tau_0}{\gamma_0}\sin\delta = G^*\sin\delta \qquad (2-18)$$

$$\tan\delta = \frac{G''}{G'} \qquad (2-19)$$

where τ_0 is the stress amplitude, γ_0 is the strain amplitude, and δ is the phase angle between the stress and strain and its range is from $0°$ to $90°$. In rheology testing, the ratio (i.e., $\tan\delta$) between G'' and G' determines how solid-like or liquid-like the sample is. The value of $\tan\delta$ gives information about the balance of lost and stored energy. For $0° < \delta < 45°$, the system is considered as a gel state (i.e., solid-like). For $45° < \delta < 90°$, the system is considered as a sol state (i.e., liquid-like)[10]. Therefore, for a GPE to be classified as solid-like, $\tan\delta$ needs to be smaller than 1. When $\tan\delta$ is smaller than 1, G'' is smaller than G', which means the elastic response dominates and the sample is more solid-like[8,43].

2.3.4. Differential Scanning Calorimetry

Differential scanning calorimetry (DSC) is a powerful tool for analysis of physical properties of a polymer, such as determination of melting and crystallization temperatures[44]. There are two thermoelectric disks in a differential scanning calorimeter, one for the sample of interest and the other for a reference sample[45]. The samples are heated at the same rate (e.g., 5℃ min^{-1}) by the disks. Since the samples are different, their heat capacities will be different, which causes a difference in the rate of thermal energy supplied to the samples. This rate is referred to as heat flow. The difference in heat flow between the two samples is recorded and plotted against temperature. Examples of DSC profiles are shown in Figure 2.16. Depending on how the heat flow is measured, it can be plotted as exothermic or endothermic. The process of crystallization is exothermic, which means that when it happens, the heater supplies less energy to the sample of

interest than to the reference sample to maintain the same heat rate (e.g., 5℃ min^{-1})[46]. In Figure 2.16, the crystallization temperatures are determined as the points of intersection of the leading edge of the crystallization exotherm and the x-axis[47].

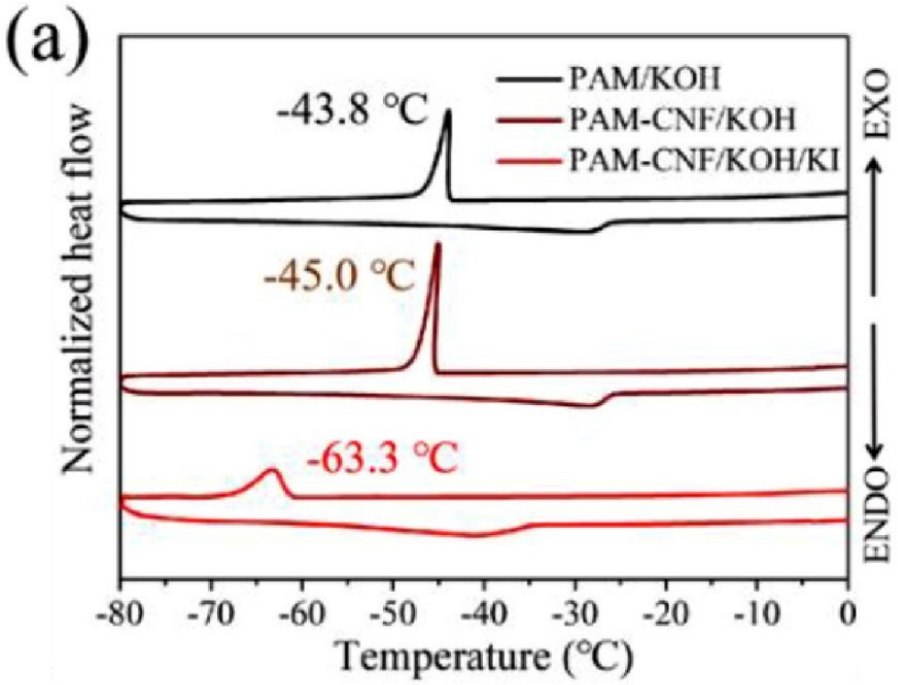

Figure 2.16. Examples of DSC profiles for GPEs using PAM and additives, with the crystallization temperatures indicated[48].

2.3.5. Ion Chromatography

Ion chromatography is an analytical technique that can be used to separate and determine ionic solutes[49]. Figure 2.17 shows components for a typical IC instrument. In this setup, a pump is used to allow the eluent to flow through the column and enter the detector. A fixed amount[50] of sample is injected into the flowing eluent using an injection device before the eluent enters the column[49]. The column is used to separate different components in the sample via ion exchange[49,50]. Different components interact with the column differently and exit the column at different times. Therefore, these sample components will enter the detector at different times, which are characteristics of these components[49]. Figure 2.18 illustrates separation between components A and B in the column as well as a typical IC chromatogram. The amount of each component in the

sample can be determined by calculating the area under each peak to the baseline of the IC chromatogram[51].

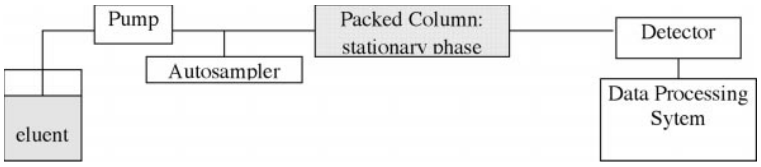

Figure 2.17. Schematic illustration for a typical IC instrument[50].

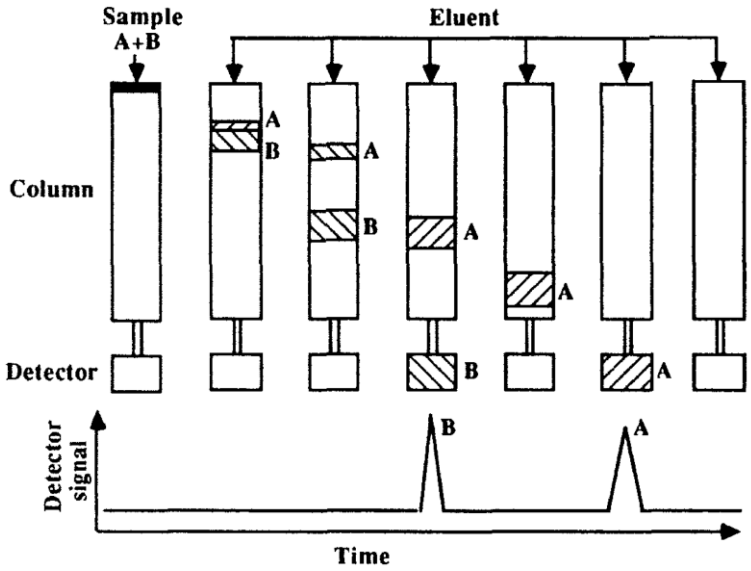

Figure 2.18. Separation of two components A and B and a typical IC chromatogram[49].

2.3.6. Ultraviolet–Visible Spectroscopy

Ultraviolet–visible (UV–vis) spectroscopy is a quantitative analytical technique that measures the absorbance or transmittance of light that passes through a medium as a function of wavelength[52]. Figure 2.19 shows a schematic for the instrumentation setup of a double-beam UV-vis spectrophotometer. A UV-vis spectrophotometer consists of beam sources, a wavelength selection device, a sample holder, a detector, and a data processing system. A tungsten lamp is usually used for visible radiation and a deuterium lamp is typically used for near-UV radiation. UV-vis spectroscopy can be used to quantify both organic and inorganic species. Organic species are detected in the near-UV region by electronic transitions, whereas some inorganic species are detected in the visible region by their intrinsic absorption of radiation[53]. Organic molecules absorb

energy from light that can excite electrons from a lower energy orbital to a higher energy unoccupied orbital. Such electronic transitions require specific energy and only a specific wavelength of light has the required amount of energy[52]. Beer's law (expressed in Equation$(2-20)$) relates absorbance and concentration and can be used for analytical study[53].

$$A = \varepsilon bc \qquad (2-20)$$

where A is the absorbance of the solution, ε is the molar absorptivity (L mol^{-1} cm^{-1}), b is the path length of radiation through the absorbing medium (cm), and c is the concentration (mol L^{-1}).

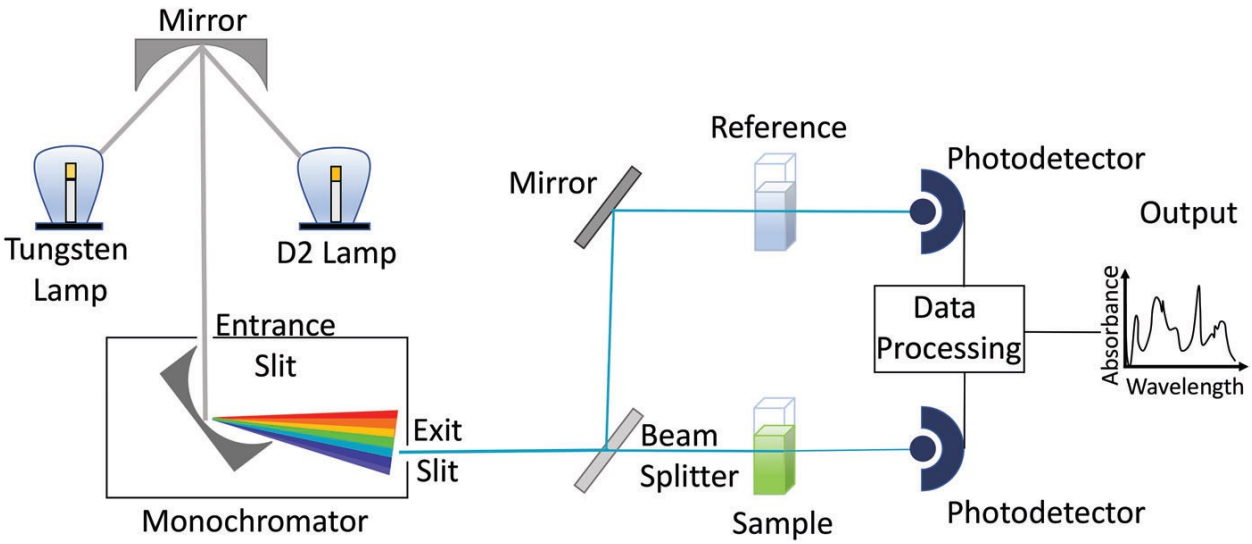

Figure 2.19. Schematic of a double-beam UV-vis spectrophotometer[52].

2.4. Summary

ZABs have the advantages of high theoretical energy, high abundance of Zn in the earth's crust, and improved safety over LIBs. However, rechargeable ZABs are not commercially viable yet, mainly due to low battery efficiencies as well as problems associated with the Zn electrode, such as dendrite formation and passivation. GPEs have been reported as being effective against short circuits caused by dendrite formation. However, GPEs can experience problems such as water loss and higher interfacial resistance between the electrolyte and the air electrode than for aqueous electrolytes. Moreover, reduced performance of GPEs at sub-zero temperatures limits their applications in rechargeable ZABs. Therefore, it is vital to develop GPEs that can perform

well at sub-zero temperatures and improve the wettability of GPEs to the air electrode, to expand the applications of GPEs in ZABs.

Chapter 3. Gel Polymer Electrolytes for Zn-air Batteries Operating at Low Temperatures

3.1. Introduction

The increase in global temperatures in recent years has raised awareness of climate change caused by the use of fossil fuels[54,55]. The transition from fossil fuels to renewable energies, such as solar energy and wind energy, is considered as a potential solution to mediate this problem[56,57]. However, these energy sources are subject to weather conditions which can cause the supply to be unstable[58,59]. Electricity, as one of the forms of these energy sources, can be stored in batteries. Lithium-ion batteries (LIBs) have proven their success in commercial use but the high cost of using LIBs in grid storage makes them less competitive compared with other batteries, such as metal-air batteries[60]. One of the candidates that is receiving considerable attention is ZABs[61]. Zn is a much safer material compared with Li and is more abundant in the earth's crust[5], which makes ZABs potentially more affordable[62,63].

Gel polymer electrolytes (GPEs) are electrolytes stored in a polymer host[64]. They can also act as a separator in ZABs and, therefore, prevent short circuits caused by dendrite formation at the Zn electrode[18,62,65]. In addition, GPEs have good mechanical properties which allow them to be used in flexible batteries[64,66–69]. When applying ZABs in electronic devices, the batteries are expected to be able to function in a reasonably cold environment[20]. However, when the temperature is decreased to sub-zero values, GPEs may freeze[70], causing the electrochemical reactions to slow down[71], resulting in a reduced battery efficiency.

The aggregation of water molecules linked by hydrogen bonded networks results in ice formation[24]. Therefore, disruption of the formation of hydrogen bonds between water molecules can be used as a strategy to extend the operation temperature of GPEs to low temperatures. Selecting a suitable polymer host should be the first step as the polymer provides the backbone of the GPE. Pei et al. compared PVA and PAA as the potential host polymer for their GPEs and used density functional theory to calculate the interaction energy between the polymer and water molecules. A larger absolute value of the interaction energy indicates stronger bonds between the polymer and water molecules as well as better resistance to low temperatures. PAA was selected as the host polymer because the carboxyl group in PAA with adjacent water molecules has a larger interaction energy (-54.06 kJ mol^{-1}) than that of PVA (-25.56 kJ mol^{-1})[28].

In addition to the selection of a proper host polymer, additives can be utilized to reduce the crystallization temperature of GPEs. One approach is to add organic solvents (e.g., ethylene glycol and glycerol) to GPEs[25]. This method reduces the crystallization temperature of GPEs but the ionic conductivity of GPEs is reduced at the same time[28]. Also, to successfully add ethylene glycol to GPEs requires costly and complex procedures that may be harmful to the environment[26]. Another approach is to add salt (e.g., $CaCl_2$, NaCl, $ZnCl_2$, and their mixtures) to the GPE during the synthesis step[25]. This method utilizes one of the colligative properties of ionic compounds. In the study conducted by Pei et al., alkalifying the carboxyl groups in PAA into a salt form improved the interaction energy between water molecules and PAA from -54.06 kJ mol^{-1} to -70.96 kJ mol^{-1}. In an experiment where both alkalified PAA (A-PAA) and PVA were stored at $-20℃$, A-PAA showed better low temperature resistance than PVA[28]. The crystallization of water was reduced due to ion hydration in this method[20]. In the case of ZABs, 6-7 M KOH is usually selected as the electrolyte due to the maximum ionic conductivity and near-maximum Zn/Zn^{2+} exchange current density achieved[5]. This feature gives ZABs an advantage in low-temperature applications as the crystallization temperature of the electrolyte without any additives may already be sufficiently low for most battery applications. This point will be further discussed in the Results and Discussion section.

Efforts have been made with the use of catalysts for ZABs in order to achieve better battery efficiency[7,14,72–74]. From the perspective of electrolytes, KI has been reported as a reaction modifier in ZABs when utilized as an additive to the electrolyte. This is achieved by altering the path of reaction when charging the battery. Instead of following the traditional OER path during charging, an alternative pathway which has a lower thermodynamic barrier is followed[48,75]. Also, since KI is a salt, its colligative properties can be used to further reduce the crystallization temperature of the electrolyte[28]. Therefore, the battery efficiency of ZABs at both room and sub-zero temperatures can be greatly improved. However, the discharging reaction(s) of the battery is not clear, which raises concerns regarding the reversibility of ZABs utilizing KI as an additive in the electrolyte.

In this study, GPEs with (GPE-KOH-KI) and without KI (GPE-KOH) are investigated for application to rechargeable ZABs at room and low temperatures. The synthesis procedures of the GPE without KI[8,10,29,30] and electrocatalysts[76] are based on previous work done within the author's research group. The objectives of this study are to develop GPEs for ZABs that can deliver

competitive battery performance at room and low temperatures and to explore the viability of utilizing KI as an additive to the electrolyte.

3.2.1. Experimental Details

3.2.1.1. Synthesis of GPEs

GPE-KOH and GPE-KOH-KI were synthesized and used in this study. Acrylic acid (99.5%, stabilized with 200 ppm 4-methoxyphenol), KOH pellets, ZnO powder, solid KI, a vortex mixer, transfer pipettes, 50 mL polypropylene conical tubes, and 5 mL polypropylene round-bottom tubes were purchased from Fisher Scientific. MBAA (99.5%) and KPS (99%) were purchased from Sigma-Aldrich.

The target precursor solution volume for both GPE-KOH and GPE-KOH-KI was 20 mL. The concentrations of each component added to the precursor solution for GPE-KOH were 6.5 M KOH, 0.2 M ZnO, 0.5 M acrylic acid, 0.03 M MBAA, and 0.0015 M KPS. All concentrations of the components were the same for GPE-KOH-KI except for ZnO, which was not added to the precursor solution.

For GPE-KOH, 7.29 g KOH and 0.3256 g ZnO were added to a 50 mL conical tube and mixed with 12 mL deionized water (DIW) using a vortex mixer. Once all solids were dissolved and the temperature of the solution was at room temperature, 0.685 mL acrylic acid was added to the tube followed by another mixing and cooling step. 0.0925 g MBAA and 0.008 g KPS were then added. More DIW was added to reach the 20 mL target. The solution was mixed vigorously for about 2 min before transferring to round-bottom tubes using a transfer pipette with each tube containing 4 mL of precursor solution. The tubes were then kept in an oven at 65℃ for 1 h to complete polymerization. The prepared GPEs were air cooled to room temperature overnight before use. GPE-KOH-KI was synthesized using the same synthesis procedure but without ZnO added during fabrication. Instead, after air cooling overnight, GPEs without ZnO were immersed in a solution containing 6 M KOH, 2 M KI, and 0.4 M ZnO to obtain GPE-KOH-KI. Non-transparent containers were used for immersion to prevent possible oxidation of KI from light.

3.2.1.2. Synthesis of Electrocatalysts

$(Co,Fe)_3O_4$ decorated nitrogen-doped carbon nanotubes (N-CNTs) and Pt/RuO_2 on carbon black were used as electrocatalysts for this work. $(Co,Fe)_3O_4$ decorated N-CNTs were previously developed in the author's group and provided good ORR and OER catalytic behavior when used with aqueous electrolytes[76]. $Co(CH_3COO)_2 \cdot 4H_2O$ (98+%) was purchased from Acros Organics. $FeSO_4 \cdot 7H_2O$, NaOH pellets, reagent alcohol (RA) (histological grade), Nafion (D-521 dispersion, 5% w/w in water and 1-propanol), parafilm, and glass vials were purchased from Fisher Scientific. N-CNTs (30-50 nm diameter, 1-2 μm length) were purchased from MKnano. A BOLA vacuum filter funnel was purchased from Finemech. Conventional ORR/OER catalysts, i.e., Pt and RuO_2 on carbon black (nominally 40% Pt, 20% Ru), were utilized for some of the electrochemical testing; the components were purchased from Alfa Aesar. Gas diffusion layer (GDL) substrates (5% polytetrafluoroethylene (PTFE) coated, Sigracet 39 BB) were purchased from the Fuel Cell Store. Carbon cloth (W0S 1009, Cetech) was purchased from Taobao.

To prepare GDL substrates impregnated with $(Co,Fe)_3O_4$ decorated N-CNTs, 35 mg $Co(CH_3COO)_2 \cdot 4H_2O$, 175 mg $FeSO_4 \cdot 7H_2O$, 80 mg NaOH, 50 mg N-CNTs, and 10 mL RA were stirred at 800 RPM for 10 min in a 30 mL glass vial. The suspension was then sonicated for 5 h before being transferred to a 250 mL beaker. 15 mL of RA and 1 mL of Nafion were added to the beaker and a circular GDL (4.5 cm in diameter) was soaked in the suspension. Sonication of the suspension was done for 20 min with the beaker sealed by a piece of parafilm and an elastic band. The GDL was then taken out and dried in air before putting in the vacuum filter. The vacuum filter allowed 7 mL of catalyst suspension to pass through the GDL. Once the GDL appeared dry, it was rinsed twice with RA, once with DIW, and one more time with RA. The 20 min sonication and filtration processes were repeated for two other pieces of GDLs. All GDLs were air dried overnight and annealed at 300℃ for 30 min before use. The mass loading of $(Co,Fe)_3O_4$ on each GDL was roughly 2.5 mg cm^{-2}.

A spray coating technique was used to prepare Pt/RuO_2 on carbon cloth (W0S 1009, Cetech) and GDL (5% polytetrafluoroethylene (PTFE) coated, Sigracet 39 BB). 50 mg of a Pt/RuO_2 mixture on a carbon black support, 2 mL DIW, 1 mL of isopropyl alcohol (added a few drops at a time with shaking to disperse), and 0.1 mL Nafion were added to a 1 dram vial. The vial was then sealed and placed in ice water to sonicate the suspension for 45 min. A spray brush (Royalmax Airbrush, 0.2 mm nozzle diameter) was used to spray coat the post-sonication suspension onto a

piece of 4 cm × 8 cm carbon cloth. The Pt/RuO_2-coated carbon cloth was dried at 60℃ for 30 min with a resulting mass loading of about 0.47 mg cm^{-2}.

3.2.1.3. Cell Fabrication

Figure 3.1a and Figure 3.1b show a sandwich-type cell made from acrylic sheets that was utilized for ZABs with GPEs. A piece of polypropylene film was used in the sandwich-type cell to restrict the contact area. Two pieces of GPEs were employed to achieve better current distribution. The thickness of the GPE in the cell was 3 mm. The contact area between the electrolyte and the air electrode was 1 cm^2, with 1 cm^2 exposed to air.

Figure 3.1c and Figure 3.1d show a 3D-printed cell that was employed for ZABs using aqueous electrolytes. The 3D model of the aqueous cell was created using SolidWorks. A Prusa i3 MK3S+ 3D printer was used to print the aqueous cell with acrylonitrile butadiene styrene (ABS) as the filament. Print quality was set to 0.15 mm with 15% infill and brim. Temperature settings for the nozzle and bed were 255℃ and 110℃, respectively. The width, height, and length of the 3D-printed cell were 1 cm, 3 cm, and 2.9 cm, respectively. The contact area between the electrolyte and the air electrode was also 1 cm^2.

Zn foil (0.25 mm thick) and acetone were purchased from Fisher Scientific. Prior to use in galvanostatic charge – discharge cyclability tests, Zn foils were ground using abrasive sandpaper (1200 grit, LECO) and washed using acetone and then reagent alcohol. Once dried with a paper towel, all sides of the highlighted areas (shown in Figure 3.1e) of the Zn foil were coated with epoxy (EpoThin 2, BUEHLER) in a hardener-to-resin weight ratio of 0.45:1. The epoxy-coated Zn foil was left in the fume hood overnight to let the epoxy harden. This epoxy was utilized to prevent water line corrosion of the Zn foil during electrochemical testing.

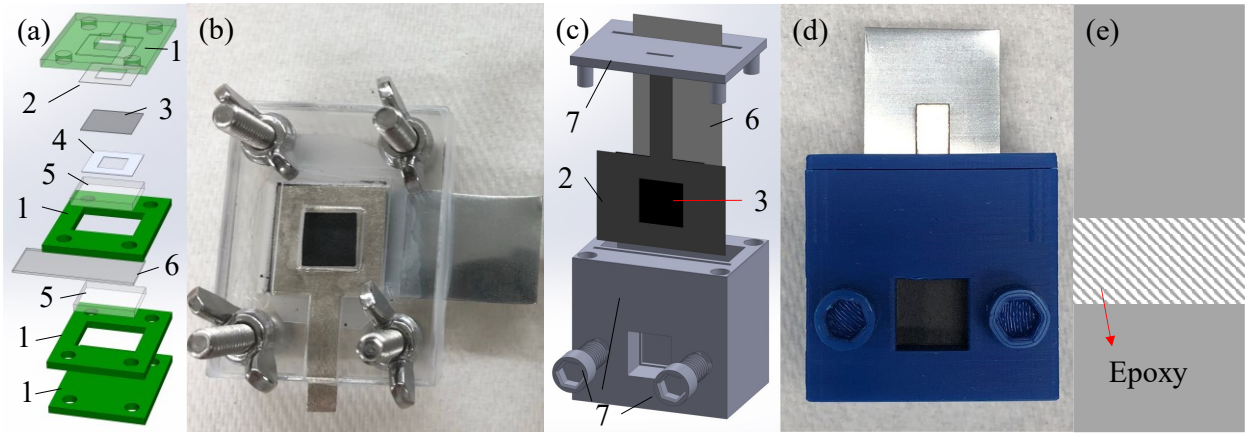

Figure 3.1. (a) Schematic of the sandwich-type cell in a disassembled view. (b) Optical image of the sandwich-type cell in an assembled view. (c) The 3D-printed cell in a disassembled view. (d) Optical image of the assembled 3D-printed cell. (e) Illustration of Zn foil coated with epoxy. Note that the numbers correspond to the following: 1) Acrylic sheets, 2) Ni current collector, 3) GDL or carbon cloth coated with electrocatalyst, 4) polypropylene film, 5) GPE, 6) Zn foil, and 7) 3D-printed parts using ABS.

3.2.1.4. Materials Characterization

A Tescan VEGA3 SEM coupled with an Oxford energy dispersive X-ray spectrometer (EDX) was used for microstructure characterization of the Zn and air electrodes. The accelerating voltage used was 20 kV for both SEM and EDX analyses.

Ionic conductivities of PAA-KOH and PAA-KOH-KI were measured using potentiostats (BioLogic VSP-100 and SP300) through EIS at open circuit potential with an applied 10 mV AC potential from 100 kHz to 10 mHz in a sealed CR2032 coin cell. For measurements at low temperatures, the coin cells containing GPE were stored in a freezer (DW-60W28, Ligfreezer Low-Temp Equipment Co., Ltd or Midea WHS-65LB1) for 20 min before testing. The following equation was used to calculate the ionic conductivities of the GPEs.

$$\delta = \frac{l}{R \cdot A} \qquad (3-1)$$

where δ is the ionic conductivity of the GPE, l is the thickness of the GPE, R is the resistance of the GPE, which is the value of the intersection with the x-axis in the Nyquist plot, and A is the area of the GPE.

An electrolyte retention capacity test of GPE-KOH and GPE-KOH-KI was done in dry (58% RH) and humid (85% RH) environments with the GPEs exposed to ambient air (21℃). The masses of the GPEs were recorded over time and the following equation was used to calculate the electrolyte retention capacity of the GPEs.

$$W_r = \frac{W_i}{W_0} \times 100\% \qquad (3-2)$$

where W_r and W_i are the electrolyte retention capacity and the weight of the GPE at time i, respectively. W_0 is the initial weight of the GPE.

The rheological properties of the GPEs were characterized by a rheometer (Kinexus Lab+) using a parallel plate geometry. The top plate had a rough surface with a diameter of 4 cm and the bottom plate was stainless steel with a 6.1 cm diameter. The sample had a height of 3 mm and the gap between the top and the bottom plate was set to 2.9 mm to ensure good contact between the sample and the plates. An amplitude sweep from 0.1 to 100% strain at 1 Hz was used to determine the linear viscoelastic region (LVER).

To determine the volume occupied by PAA in GPE-KOH, a 4 mL GPE-KOH sample was taken out of the round-bottom tube and immersed in DIW for 3 days to allow electrolyte to leach out of the GPE. Then the sample was completely dried in a vacuum sealed container with desiccant for 1 week. The sample was weighed, and the volume of the polymer was calculated using the following equation. More details are presented in Section 3.5.1.

$$Volume\ of\ PAA = \frac{Weight\ of\ PAA\ sample}{Density\ of\ PAA} \qquad (3-3)$$

To analyze composition changes in the electrolyte after charge and discharge, an aqueous mixture of 6 M KOH and 2 M KI was charged at 0.83 V vs. Hg/HgO for 2 h and discharged at -0.77 V vs. Hg/HgO for 2 h using a potentiostat (BioLogic VSP-100) and carbon cloth coated with Pt/RuO_2 as the air electrode. The setup used is shown in Figure 3.2a. The anion composition of the

produced water samples was characterized using ion chromatography. The water samples were first diluted by a factor of 10,000 before being filtered through a 0.45 μm hydrophilic syringe filter. The samples were further diluted by a factor of 10 with DIW and injected into an ion chromatography system (Dionex 5000). An analytical column (AS 17) and a guard column were used as the stationary phase. The mobile phase was an aqueous solution containing 1 mM $NaHCO_3$ and 3.5 mM Na_2CO_3, and a constant flow rate was set at 1 mL min^{-1}. The conductivity chromatogram was recorded through a conductivity detector after suppressing the eluent background conductivity with an anion self-regenerating suppressor (ASRS 300). Locations of peaks for KI and KIO_3 were determined by running IC tests on standard KI and KIO_3 solutions prepared using chemicals purchased from Fisher Scientific.

An ultraviolet–visible (UV–vis) spectrometer (Varian Cary 50) was used to generate UV–vis spectra for aqueous KOH, DIW, KIO_3, and KI samples. Samples were diluted so that the absorbance was smaller than 1. Quartz crucibles with a path length of 5 mm were used for this test.

3.2.1.5. Electrochemical Measurements

All electrochemical measurements were done using BioLogic VSP-100 and SP300, as well as Arbin LBT20084, potentiostats. For batteries using GPEs as electrolytes, the batteries were left in the ambient environment for 1 h before any full cell testing to allow the GPE wet the GDL or carbon cloth. To bring the temperature of the battery to low temperatures, batteries were kept in the freezer (DW-60W28, Ligfreezer Low-Temp Equipment Co., Ltd or Midea WHS-65LB1) for 2 h after assembly and the 1 h wetting step. The temperatures of the freezers were set to 0℃, $-25℃$, and $-45℃$. However, due to fluctuations of temperature in the freezers, the actual temperature ranges were $-3 \pm 2℃$, $-28 \pm 5℃$, and $-41 \pm 3℃$. In galvanostatic charge – discharge cyclability tests, each cycle was 30 min long and composed of a sequence of 10 min discharging, 5 min rest, 10 min charging, and 5 min rest. During galvanostatic charge – discharge rate tests, batteries were discharged at 2, 5, 10, and 20 mA cm^{-2} for 10 min at each current density, followed by a 10 min rest before charging at the same current densities for 10 min each. Battery efficiency for both cyclability testing and rate testing were calculated using the following equation.

$$\eta = \frac{E_{discharge}}{E_{charge}} \times 100\% \qquad (3-4)$$

where η is the battery voltage efficiency, while $E_{discharge}$ and E_{charge} are the battery discharge voltage and charge voltage, respectively.

Battery efficiency improvement percentage was calculated using the following equation.

$$Improvement\% = \frac{\eta_{GPE-KOH-KI} - \eta_{GPE-KOH}}{\eta_{GPE-KOH}} \times 100\% \qquad (3-5)$$

where $\eta_{GPE-KOH-KI}$ and $\eta_{GPE-KOH}$ are the calculated battery efficiencies for ZABs using GPE-KOH-KI and GPE-KOH, respectively.

Cyclic voltammetry (CV) was used to determine the reactions at the Zn electrode and the air electrode. The three-electrode setups for CV tests for the Zn electrode and air electrode are shown in Figure 3.2a and Figure 3.2b, respectively.

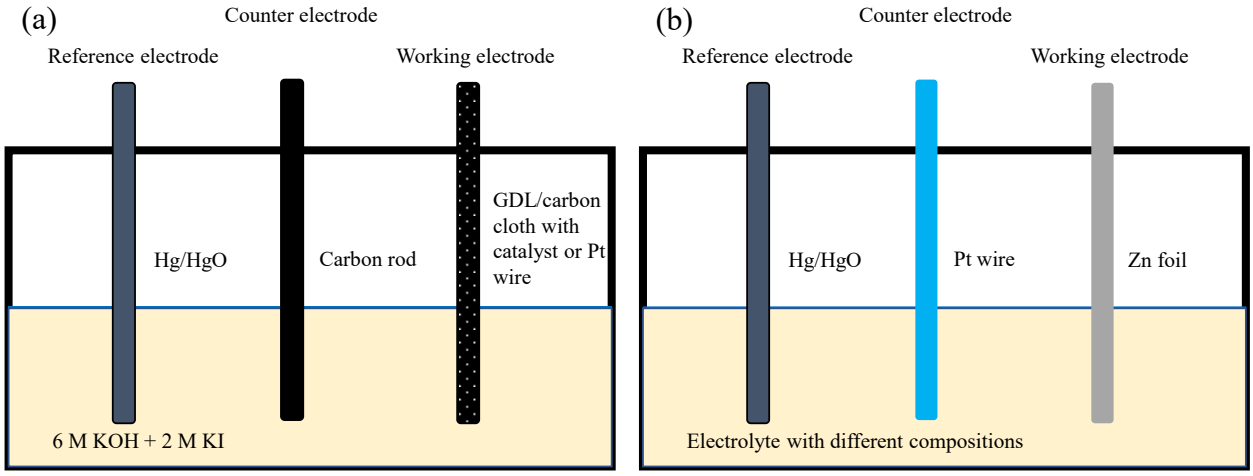

Figure 3.2. (a) Three-electrode setup for CV tests at the air electrode. (b) Three-electrode setup for CV tests at the Zn electrode.

The discharge polarization curve was obtained by discharging the battery from 0 mA to 400 mA with a scan rate of 1 mA s^{-1}. The power density of the batteries was determined using the discharge polarization curve and the following equation.

$$P = J \cdot V \qquad (3-6)$$

where P, J and V are the power density of the battery, discharge current density and the corresponding discharge voltage, respectively.

3.3. Results and Discussion

3.3.1. Characterizations of Gel Polymer Electrolytes

Rheological measurements were done for GPE-KOH and GPE-KOH-KI using an amplitude sweep for the confirmation of successful synthesis of GPEs. Conventionally in rheology testing, the phase angle (δ) needs to be between $0°$ and $45°$ in order for a sample to be considered as solid-like (i.e., gel state)[10]. As shown in Figure 3.3a, $\tan\delta$ values for GPE-KOH and GPE-KOH-KI are both smaller than 1, which indicates that both samples can be classified as GPEs.

To estimate the crystallization temperature of GPE-KOH and GPE-KOH-KI, the phase diagram for the KOH - H_2O system (shown in Figure 3.3b) was used. The amount of K corresponding to a 6 M KOH aqueous solution is about 3.5 at% (detailed calculations are shown in Section 3.5.1. Calculation Details). As illustrated in the diagram, the corresponding crystallization temperature for KOH solution at this concentration is about $-50℃$, which should be sufficient for the majority of battery applications. When stored in a freezer at $-41℃$ overnight, neither of the GPEs froze. Therefore, GPE-KOH and GPE-KOH-KI both have good low-temperature resistance and were later used in low temperature electrochemical tests.

Electrolyte retention capacity testing for GPE-KOH and GPE-KOH-KI was done in a closed container in both dry (58% relative humidity) and humid (85% relative humidity) environments by exposing the GPEs directly to ambient air at room temperature. As shown in Figure 3.3c, when tested in the dry environment, GPE-KOH-KI has better electrolyte retention with an electrolyte retention of 98.7% at 12 h and 90.7% at 100 h. GPE-KOH, on the other hand, has an electrolyte retention of 96.9% at 12 h and 84% at 100 h. The host polymer plays a vital role in the water retention capability of the GPE. PAA is highly hydrophilic and known as a superabsorbent which can absorb water in amounts corresponding to several hundred times its weight[77,78], which may hinder water evaporation from the GPE. The slower dehydration rate of GPE-KOH-KI may be attributed to the hydration of K^+ and I^- that improved the attraction between ions and water molecules[48]. When tested in an environment with an 85% relative humidity (RH), Figure 3.3d shows that the weights of both GPEs increase at nearly the same rate, to 110% of the initial weights at 12 h and 155% at 100 h. This result reveals the hygroscopic property[79] of the GPEs. In daily use, RH fluctuation in ambient air is common and the intrinsic semi-open structure

of ZABs allows water in the electrolyte to evaporate. Therefore, this feature allows the GPEs to absorb water when the RH is high enough which allows the electrolyte to retain water content against evaporation. The volume occupied by the polymer in the GPE was 0.28 mL, which means 7% of the GPE system is in the electrolyte.

Figure 3.3e and Figure 3.3f show ionic conductivities for GPE-KOH and GPE-KOH-KI at 21℃, −3℃, −28℃, and −41℃. Ionic conductivities for both samples are almost the same at low temperatures with the ionic conductivities of GPE-KOH being slightly higher than those of GPE-KOH-KI. At 21℃, GPE-KOH has an ionic conductivity of 216 mS cm^{-1} whereas GPE-KOH-KI has a conductivity of 184 mS cm^{-1}. An increase in the amount of ions may improve the ionic conductivity of the electrolyte. However, when the temperature is −3℃ or lower, the viscosity of the electrolyte increases and the ion transport kinetics are expected to decrease, which affects the ionic conductivity of the electrolyte. Depressing the freezing point of the electrolyte by adding more salt is considered an effective strategy of enhancing the ion transport kinetics of electrolytes at low temperatures[80]. The addition of KI to the GPE makes the crystallization temperature of the GPE-KOH-KI lower than that of GPE-KOH, which helps narrow the ionic conductivity gap between these two electrolytes at low temperatures. Zhang et al. added KI to PAM and compared its crystallization temperature with the sample without KI. PAM with KI added as an additive exhibited a crystallization temperature of −63.3℃, whereas the crystallization temperature of the sample without KI was −45.0℃[48].

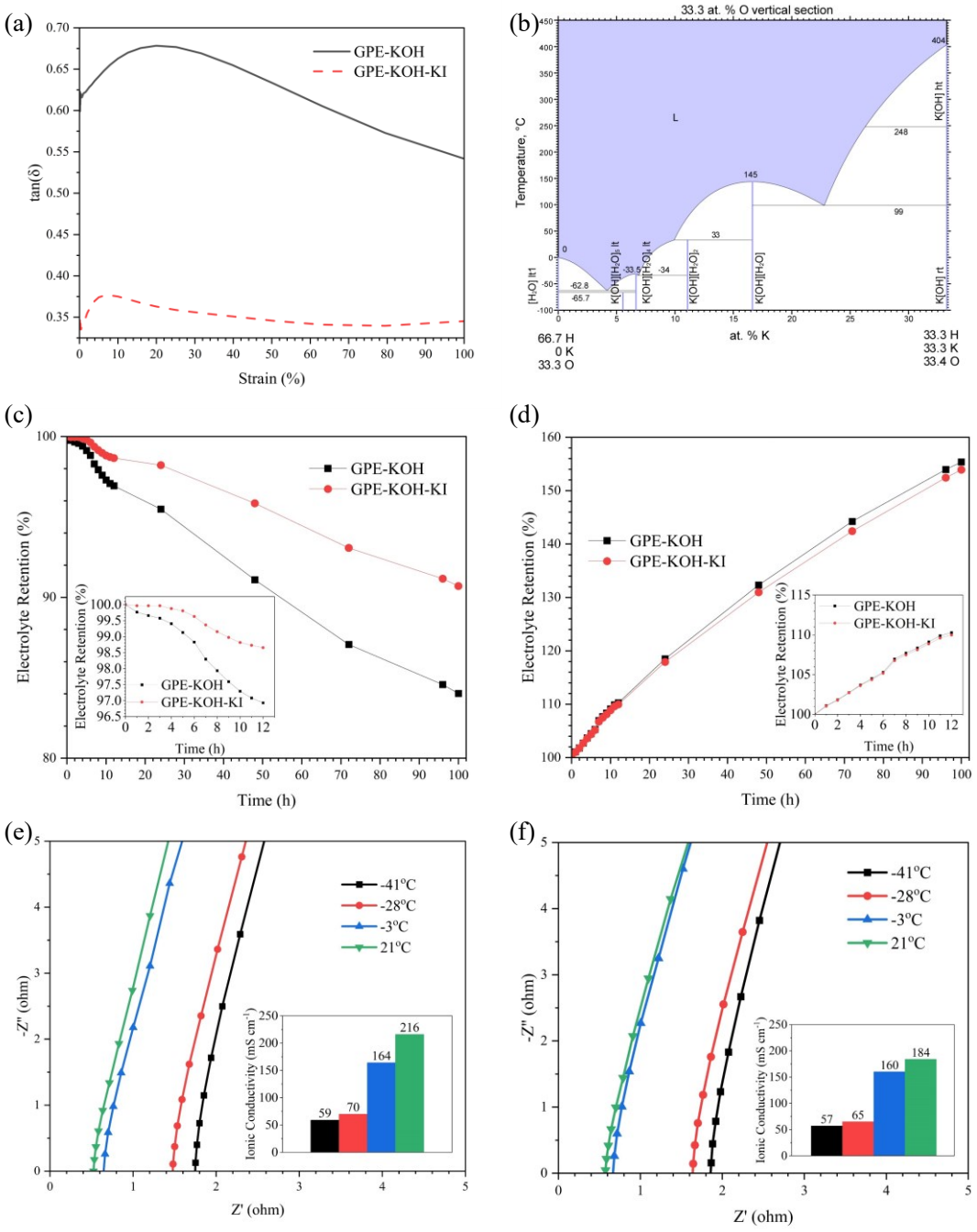

Figure 3.3. (a) Rheological measurements for GPE-KOH and GPE-KOH-KI using an amplitude sweep from 0.1-100% strain at 1 Hz. (b) Phase diagram for the KOH - H_2O system[27]. Electrolyte retention for GPE-KOH and GPE-KOH-KI in (c) a dry environment (58% RH) and (d) a humid (85% RH) environment, with the results of the first 12 h shown as insets. Impedance plots and ionic conductivity (shown as insets) for (e) GPE-KOH and (f) GPE-KOH-KI at different temperatures. The color schemes for the main legend and inset bars are matched.

3.3.2. Electrochemical Performance of ZABs Using GPE-KOH

A sandwich-type cell (shown in Figure 3.1a) was used for full cell testing of ZABs with GPE-KOH. GDL with $(Co,Fe)_3O_4$ decorated nitrogen-doped carbon nanotubes (N-CNTs) were used as the air electrode. Prior to the tests, each ZAB using GPE was left at room temperature for 1 h to allow the GPE to wet the air electrode. To make sure the temperature of the battery was at the designated low temperature, each battery was left in the freezer for an additional 2 h before each electrochemical test. The temperature of the freezer fluctuates, so the temperature ranges are $-3 \pm 2℃$, $-28 \pm 5℃$, and $-41 \pm 3℃$. Hereafter, the temperature for each corresponding temperature range is reported as $-3℃$, $-28℃$ and $-41℃$, respectively. Figure 3.4a shows the galvanostatic charge – discharge (GCD) curves at different current densities (referred to as rate tests) and different temperatures. Table 3.1 summarizes the rate test battery efficiency as well as the peak power density at each condition. As shown in Figure 3.4a, ZABs using GPE-KOH delivered relatively stable battery performance at current densities up to 10 mA cm^{-2} at $-41℃$ and stayed operable at 20 mA cm^{-2} and $-28℃$ with reduced stability than the performance obtained at higher temperatures. Also, the battery efficiencies dropped as the temperature decreased. Larger drops at higher current densities were observed. For example, the battery efficiency for 2 mA cm^{-2} dropped by 13% when the temperature was decreased from $21℃$ to $-41℃$, but the efficiency for 10 mA cm^{-2} reduced by 22% with the same amount of temperature drop. Furthermore, the ZABs using GPE-KOH could not operate (i.e., failed) when tested at 20 mA cm^{-2} and $-41℃$. As the temperature dropped, the ionic conductivity of GPE-KOH decreased, and electrochemical reaction kinetics became more sluggish. Operating at higher current densities requires relatively higher electrolyte ionic conductivities and faster reaction kinetics, which may be the reason why the battery efficiency drop was larger at higher current densities and why the battery could not operate at 20 mA cm^{-2} when tested at $-41℃$. Figure 3.4b shows the discharge polarization curves and their corresponding power densities at different temperatures. As shown in Figure 3.4b, the peak power density for ZABs using GPE-KOH decreased significantly when the temperature was reduced from $21℃$ to $-3℃$, with 127 mW cm^{-2} achieved at $21℃$ and 38 mW cm^{-2} at $-3℃$ (70% drop in power density). However, the differences in power density at lower temperatures were not as significant as the difference when the temperature was decreased from $21℃$ and $-3℃$, with a 21 mW cm^{-2} drop from $-3℃$ to $-28℃$ and a 6 mW cm^{-2} drop from $-28℃$ to $-41℃$. A number of factors may be responsible. A decrease in temperature results in an increase in charge transfer

resistance, and a decrease in ionic conductivity[81]. Therefore, ion diffusion velocity was reduced. As the temperature approaches to the crystallization temperature of the GPE, the GPE becomes more rigid and the wettability of the GPE worsens, resulting in an increase in the interfacial resistance. At low temperatures, electrochemical reaction kinetics also become more sluggish[81–83]. These factors are responsible for the decrease in power density.

To investigate the cyclability of ZABs using GPE-KOH, GCD cyclability tests were done at different current densities and temperatures. Figure S3.1a shows a comparison between two cyclability tests conducted in the winter and summer. Initially, a cyclability test was conducted at 21℃ and 10 mA cm^{-2} in the summer using GPE-KOH as the electrolyte and GDL with $(Co,Fe)_3O_4$ decorated N-CNTs as the air electrode. The same test was done later in the winter using the same setup to check the repeatability of the result. As shown in Figure S3.1a, the cyclability of the battery was significantly worse and failed close to the end of the test when tested in the winter. Efforts were made to identify the cause(s) of the worse results. Fluctuations in the RH in the laboratory were eventually determined as the reason. Therefore, for all cyclability tests conducted at 21℃, the RH of the test environment was controlled to about 85%, in order to reduce the effect of RH fluctuations. When tested at other temperatures, the corresponding RH was measured but not controlled. The measured RH in the freezers at −3℃, −28℃, −41℃ were 45%, 36%, and 35%, respectively.

Figure 3.4c to Figure 3.4e show the GCD curves for cyclability tests conducted at different temperatures at 2 mA cm^{-2}, 5 mA cm^{-2}, and 10 mA cm^{-2}, respectively. The fluctuations in the charging and discharging voltages were caused by temperature fluctuations in the freezers. As shown in the figures, ZABs using GPE-KOH could cycle for 100 h with little performance degradation at 2 mA cm^{-2} and 5 mA cm^{-2} when tested at −41℃, and at 10 mA cm^{-2} when tested at −28℃, demonstrating excellent cyclability at low temperatures. The initial and final battery efficiencies for different test conditions are shown in Table 3.2. As shown in Figure 3.4c to Figure 3.4e as well as Table 3.2, battery efficiency decreased with decreasing temperature for each current density, which is attributed to a decrease in ionic conductivity and electrochemical reaction kinetics and an increase in resistance. As illustrated in Figure 3.4a, the ZAB with GPE-KOH could operate at −41℃ and 10 mA cm^{-2} but the charging voltage increased slightly during the test, which indicated poorer stability under those conditions. This instability may be responsible for failure of

the battery in the cyclability test conducted under the same conditions. Since the degradation in battery performance was not severe when tested at 10 mA cm^{-2} and 21℃, an extended cyclability test was done (Figure 3.4f) for ZAB using GPE-KOH to reveal the lifetime of the ZAB. As shown in Figure S3.1b, the ZAB using GPE-KOH could cycle for 260 h before experiencing accelerated degradation in discharging performance. The initial battery efficiency was 61% and the battery efficiency after 260 h was 42%. Even though the efficiency decreased during cycling, the battery still had not failed after 260 h.

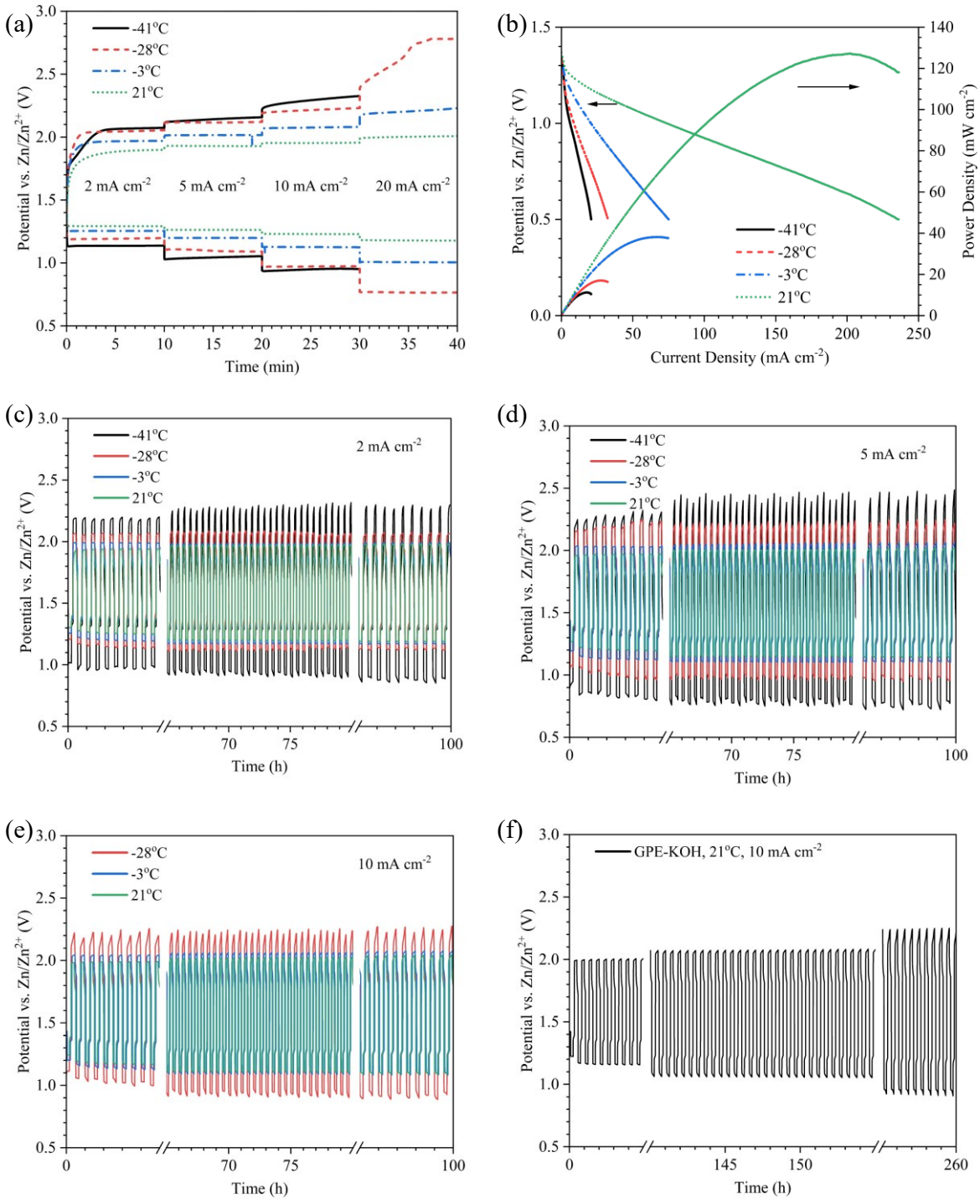

Figure 3.4. (a) Rate tests for ZABs using GPE-KOH at different temperatures. (b) Discharge polarization curves and corresponding power densities. Cyclability tests at different temperatures for ZABs using GPE-KOH at (c) 2 mA cm^{-2}, (d) 5 mA cm^{-2}, and (e) 10 mA cm^{-2}. (f) ZAB lifetime test using GPE-KOH at 21℃ and 10 mA cm^{-2}.

Table 3.1. Summary of rate test battery efficiencies and power densities for ZABs using GPE-KOH under different test conditions

	Efficiency at different current densities (%)				
Temperature (°C)	2 mA cm^{-2}	5 mA cm^{-2}	10 mA cm^{-2}	20 mA cm^{-2}	Peak power density (mW cm^{-2})
21	68	67	63	59	127
-3	64	60	54	45	38
-28	58	51	43	27	17
-41	55	49	41	Failed	11

Table 3.2. Summary of cyclability test battery efficiencies for ZABs using GPE-KOH under different test conditions

	2 mA cm^{-2}		5 mA cm^{-2}		10 mA cm^{-2}	
Temperature (°C)	Initial Efficiency (%)	Final Efficiency (%)	Initial Efficiency (%)	Final Efficiency (%)	Initial Efficiency (%)	Final Efficiency (%)
21	68	60	64	57	63	53
-3	63	59	59	53	59	52
-28	58	54	50	43	50	41
-41	46	39	42	32	Failed	Failed

3.3.3. Reaction Mechanisms for ZABs Using KI as An Electrolyte Additive

Prior to running electrochemical tests using GPE-KOH-KI in full cells, aqueous 6 M KOH+2 M KI+0.4 M ZnO was utilized with $(Co,Fe)_3O_4$ coated GDLs in a cyclability test using the cell setup shown in Figure 3.1c. As illustrated in Figure 3.5a, when $(Co,Fe)_3O_4$ coated GDL was used as the air electrode, the battery experienced fast polarization and early cell failure (reached cut-off voltages), which indicates poor battery cyclability. To better understand the cause for the poor performance, a CV test using the setup in Figure 3.2a was done (Figure 3.5b). With

$(Co,Fe)_3O_4$ coated GDL as the working electrode, one oxidization peak (peak (1)) appeared between 0.5 V and 1 V, which corresponds to the oxidization of I^- to IO_3^-. This oxidation step is believed to be an electrochemical-chemical step, where I^- is first oxidized to I_2 during an electrochemical reaction and then I_2 disproportionates to IO_3^- and I^- through a rapid chemical reaction since I_2 is not stable in an alkaline environment[84]. The two-step reaction is shown below.

Electrochemical reaction:

$$6I^- + 6e^- \longrightarrow 3I_2 \qquad (3-7)$$

Chemical reaction:

$$3I_2 + 6OH^- \longrightarrow IO_3^- + 5I^- + 3H_2O \qquad (3-8)$$

The oxidization of I^- has a much lower thermodynamic barrier than the conventional OER, which is the reason that the charging voltage is greatly reduced[48,75,85]. However, no reduction peak other than the ORR peak was observed, which raises concerns about the reversibility of the iodate reaction. Moreover, this result suggests that there may be accumulation of IO_3^- at the air electrode, which could block active sites at the air electrode and lead to precipitation of KIO_3. At 20℃, the solubility of KIO_3 in water is roughly 0.008 g mL^{-1}, which is equivalent to 3.7×10^{-5} M of KIO_3[86]. With KOH dissolved in water and less free water available, the solubility of KIO_3 in the KOH solution may be lower than that in water alone. Therefore, as KIO_3 accumulates in the electrolyte, there will likely be precipitation of KIO_3 because of its low solubility.

In previous work done on ZABs utilizing KI as an additive to the electrolyte, Pt was used as the catalyst[48,75]. It was hypothesized that Pt was essential for the reversal of IO_3^- to I^-. Therefore, to investigate the reversibility of the I^-/IO_3^- reaction, a Pt wire was used in a CV test with the cell setup shown in Figure 3.2a. As shown in Figure 3.5c, when the Pt wire was used as the working electrode, an oxidation peak (peak (1)) corresponding to the reaction from I^- to I_2 and two reduction peaks, respectively, corresponding to the reduction of IO_3^- to I^- (peak (3)) and I_2 to I^- (peak (2)) were observed. These two reactions are shown below.

Peak (2):

$$I_2 + 2e^- \longrightarrow 2I^- \qquad (3-9)$$

Peak (3):

$$IO_3^- + 3H_2O + 6e^- \longrightarrow I^- + 6OH^- \qquad (3-10)$$

The reduction peak of I_2 to I^- is only observed at high scan rates as the reaction from I_2 to I^- is fast[84]. The CV result suggests the redox reaction of I^-/IO_3^- is reversible when Pt is used as the catalyst. Therefore, to test the battery cyclability without the effect of a polymer host, a GDL coated with Pt/RuO_2 was used with aqueous 6 M KOH+2 M KI+0.4 M ZnO in cyclability tests. RuO_2 was included in the catalyst because it was used in previous work done that utilized KI as an additive to the electrolyte[48]. As shown in Figure 3.5d and Figure 3.5e, the battery cyclability was improved significantly. Benefitting from the change in path for charging reaction, the battery charging voltage was greatly reduced, resulting in initial and final efficiencies of 77% and 70%, respectively, at 5 mA cm^{-2} and 71% and 59%, respectively, at 10 mA cm^{-2}. However, the battery cycled at 10 mA cm^{-2} experienced rapid battery performance degradation after 90 h. A hole formed in the Zn electrode and residue was present at the bottom of the cell (Figure 3.5f), raising concerns regarding the reversibility of the reaction at the Zn electrode.

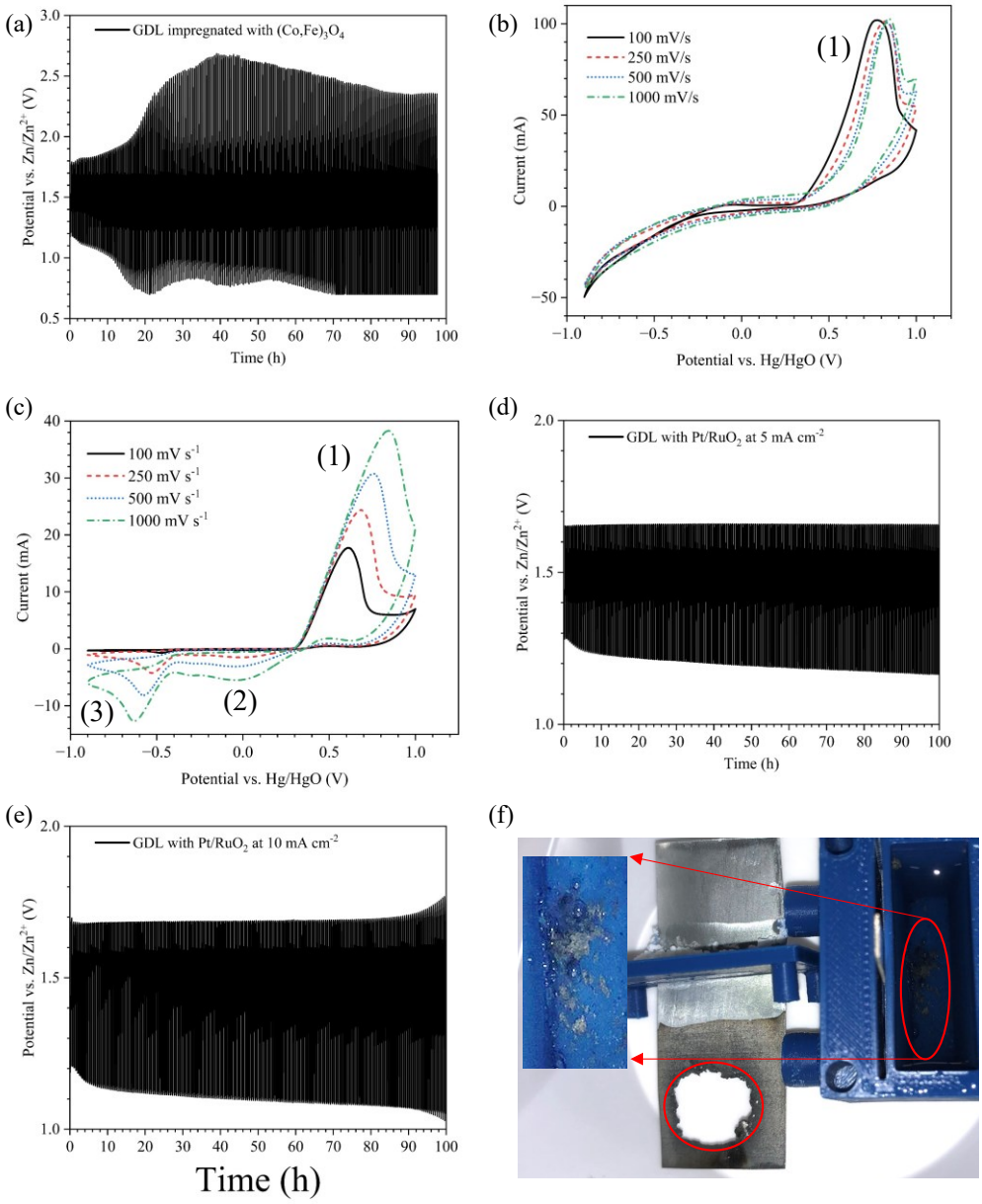

Figure 3.5. (a) Cyclability test at 10 mA cm^{-2} using aqueous 6 M KOH+2 M KI+0.4 M ZnO as the electrolyte and GDL with $(Co,Fe)_3O_4$ decorated N-CNTs as the air electrode. (b) Cyclic voltammograms at different scan rates obtained for $(Co,Fe)_3O_4$ coated GDL as the working electrode in 6 M KOH+2 M KI. (c) Cyclic voltammograms at different scan rates obtained for a Pt electrode in 1 M KOH+0.33 M KI. GCD curves at 21℃ (d) 5 mA cm^{-2}, and (e) 10 mA cm^{-2} using aqueous 6 M KOH+2 M KI+0.4 M ZnO and GDL coated with Pt/RuO_2. (f) Optical image of the 3D-printed cell and Zn electrode after the test shown in Figure 3.5e. Picture brightness was enhanced for the bottom of the cell to reveal the residue.

SEM and EDX analyses were performed to investigate the cause of the hole and to identify the residue. Figure 3.6a shows an SEM secondary electron (SE) image of a Zn foil after grinding the surface with sandpaper and rinsing with ethanol and reagent alcohol. The surface area of the Zn foil increased because of the grinding step. Figure 3.6b and Figure 3.6c are SEM SE images of the residue left at the bottom of the cell after the cycling test and on the Zn electrode (in the charged state) at the edge of the hole, respectively. Figure S3.2 shows SEM SE images for these samples at lower magnifications. After cycling, the surface of the Zn electrode became less smooth. The EDX spectrum in Figure 3.6d shows that the residue left at the bottom of the cell is mainly Zn. The small O peak indicates that some of the Zn has oxidized to ZnO. The EDX spectra in Figure 3.6e show much larger O peaks, which indicates that ZnO has formed at the surface of the Zn during cycling. The K peak is likely KOH residue on the Zn surface.

To determine whether the reaction at the Zn electrode was reversible, a CV test on the Zn electrode was done in different electrolytes using the setup shown in Figure 3.2b. As shown in Figure 3.6f, when tested in 6 M KOH+2 M KI+0.4 M ZnO, an oxidization peak and a reduction peak appear at almost the same potential as the electrolytes without KI. Therefore, it is likely that Zn is redeposited on the Zn electrode as the battery is cycled. However, as Zn dendrites grow, the needle-like protrusions eventually fracture and fall to the bottom of the cell, producing the residue and the hole in the Zn electrode.

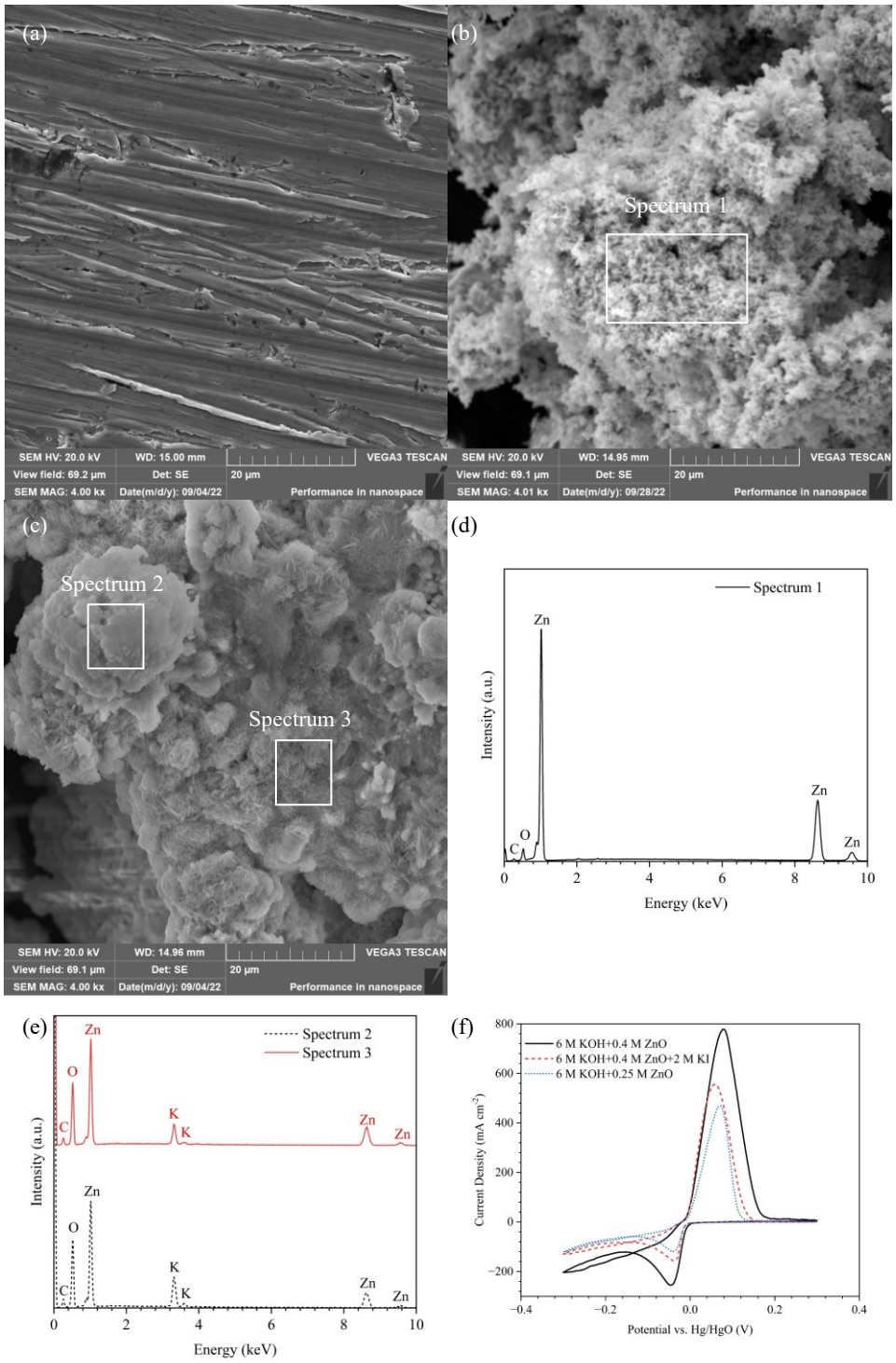

Figure 3.6. SEM SE images of (a) polished Zn foil, (b) particles at the bottom of the cell, and (c) Zn electrode after cycling for 100 h in aqueous 6 M KOH+2 M KI+0.4 M ZnO. (d-e) EDX spectra for the regions shown in the SEM SE images in (b) and (c). (f) Cyclic voltammogram obtained from a Zn electrode in different electrolytes with a scan rate of 50 mV s^{-1}.

It is important to confirm whether IO_3^- converts back to I^- during discharge in order to determine whether the battery is fully rechargeable. Previous work done by other groups where KI was utilized as an electrolyte additive used UV-vis spectroscopy to confirm the conversion of IO_3^- to I^- during discharging. Two groups have claimed that the appearance of a peak at between 300 and 350 nm during charge is due to the formation of IO_3^- and the disappearance of the peak during discharge indicates the conversion of IO_3^- to I^- [48,75]. However, the same peak was assigned to I_3^-, instead of I^-, in the references cited by the authors of the two studies. The cited references used UV-vis spectroscopy to analyze I_3^-, whereas IO_3^- was analyzed using ion chromatography[87,88].

For this work, standard solutions of KIO_3, KI, and KOH were prepared to determine whether UV-vis could be used for the confirmation of KIO_3 when KOH and KI also coexist in the solution. As illustrated in Figure 3.7a, KI, KOH and KIO_3, all show an increase in absorbance between 200 nm and 250 nm with KI exhibiting a peak. No peaks were observed at other wavelengths. This result indicates that when KI, KOH, and KIO_3 coexist in a solution, only the concentration of KI can be determined from the UV-vis results. Therefore, UV-vis is not suitable for direct analysis of the concentration change of KIO_3.

An attempt at using ion chromatography (IC) for analyzing KIO_3 was made. Standard solutions containing 40 ppm KI+4 ppm KIO_3 and 3.4 ppm KOH+10 ppm KI+1 ppm KIO_3 were prepared for IC measurements. A solution of 1 mM $NaHCO_3$ and 3.5 mM Na_2CO_3 was used as the eluent. As shown in Figure 3.7b, two peaks appear in the chromatogram obtained using 40 ppm KI+4 ppm KIO_3 at around 3 min and 10 min, which are respectively assigned to KIO_3 and KI because the concentration of KI is much higher. In IC measurements, the concentration of each species is determined by calculating the area under the peak relative to baseline. In the chromatogram obtained using the 3.4 ppm KOH+10 ppm KI+1 ppm KIO_3 standard solution, two additional peaks are observed between the KIO_3 and KI peaks, which are likely due to the products formed from the reaction between KOH and $NaHCO_3$. The setup shown in Figure 3.2a was used to prepare samples for the IC measurements with carbon cloth (CC) coated with Pt/RuO_2 used as the working electrode. Sample A served as a reference and contained 0.6 mM KOH+0.2 mM KI. Sample B was prepared by charging the half-cell that contained 6 M KOH+2 M KI followed by a dilution step and sample C was prepared by discharging the half-cell containing sample B followed by a dilution step. Sample A should have the highest KI concentration because samples B and C

would not produce more KI. During charging, KI should be oxidized and produce I_2, which would then form KIO_3 and KI due to disproportioniation[48,85]. Therefore, the concentration of KI for sample B should be smaller than that for sample A. The concentration of KIO_3 for sample C is unknown, but the concentration of KI for sample C should be smaller than that for sample A because sample B and C could not produce more KI. However, as illustrated in Figure 3.7c and Figure 3.7d, sample B exhibited a larger KI concentration, whereas the concentration of KI for sample A was the smallest, making the IC results unreliable. Moreover, as shown in Figure 3.7e, sample C had the highest KIO_3 concentration among the three samples, which was unexpected, as during battery discharging the KIO_3 concentration is expected to decrease. The IC results seem to indicate that more KI is oxidized during discharging. These unexpected results may be attributed to reaction between KOH and the eluent, which contained $NaHCO_3$. Such a reaction would affect the conductivity of the eluent, which was assumed to be fixed. The change in conductivity led to misleading results. Figure 3.7f shows the KI and KIO_3 peaks obtained using standard solutions with and without KOH. One sample contained 40 ppm KI+4 ppm KIO_3 (standard KI+KIO_3 sample) and the other contained 3.4 ppm KOH+10 ppm KI+1 ppm KIO_3. Since the concentrations of KI and KIO_3 in the standard KI+KIO_3 sample are 4 times that of the other sample, the area under each peak relative to baseline for both samples should demonstrate a similar relation as well. However, the area for the KIO_3 peak for the standard KI+KIO_3 sample is clearly much more than 4 times that of the other sample. Therefore, the IC measurement results did not provide meaningful results.

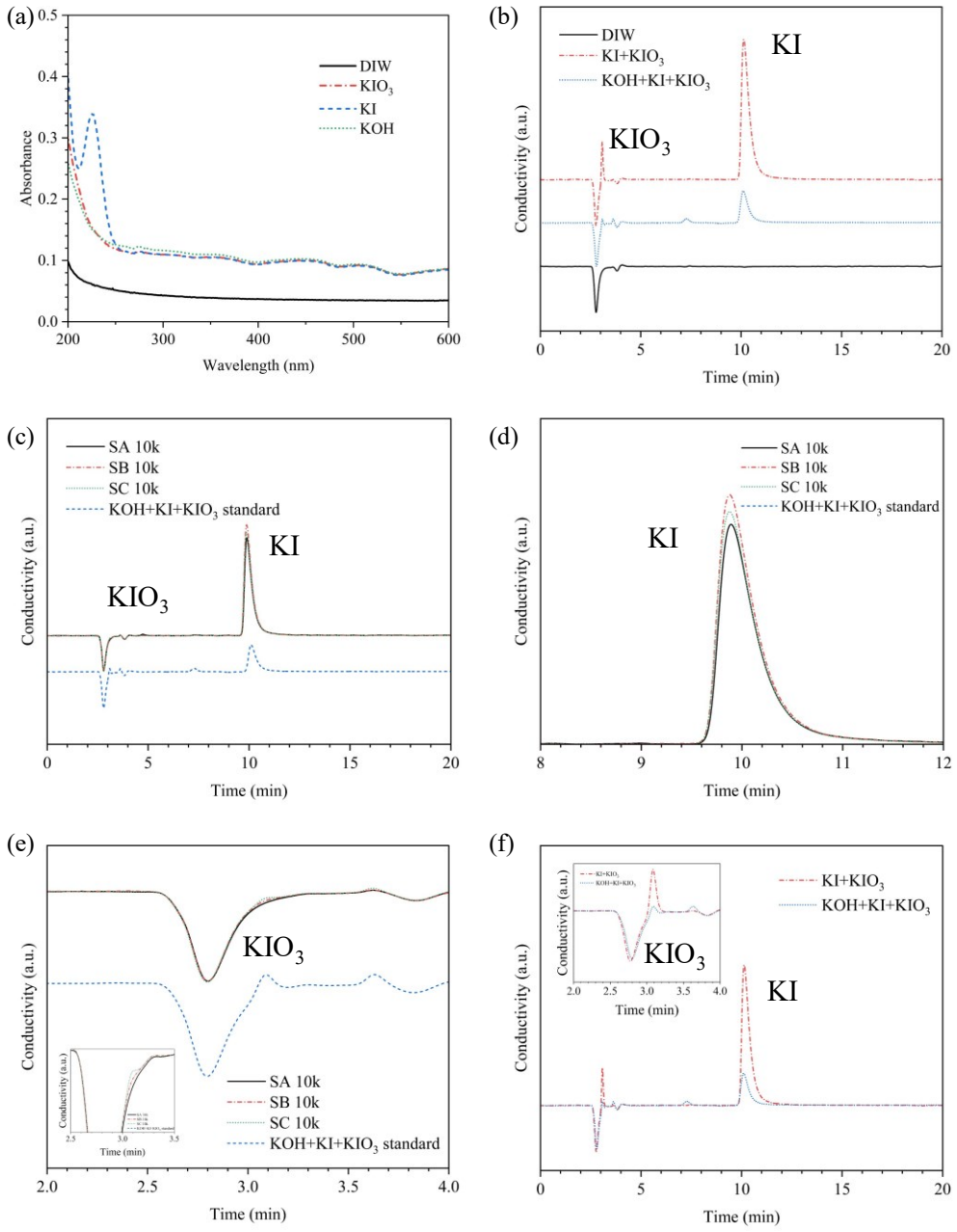

Figure 3.7. (a) UV-vis spectra for different standard solutions. (b) Ion chromatograms for DIW, standard 40 ppm KI+4 ppm KIO_3, and 3.4 ppm KOH+10 ppm KI+1 ppm KIO_3 solutions. (c) Ion chromatograms for samples A (0.6 mM KOH+0.2 mM KI), B, and C (unknown amounts of KOH+KI+KIO_3) as well as the 3.4 ppm KOH+10 ppm KI+1 ppm KIO_3 standard solution. Zoomed-in ion chromatogram to reveal the peaks for (d) KI and (e) KIO_3. (f) Comparison of ion chromatograms for standard 40 ppm KI+4 ppm KIO_3 and 3.4 ppm KOH+10 ppm KI+1 ppm KIO_3 solutions.

Whereas our attempt to determine whether IO_3^- was converting back to I^- during discharge was not successful, the issue can be speculated with theoretical argument. Figure 3.8a was plotted using the data obtained from Figure 3.5c. Figure 3.8a shows that the peak current for both the oxidization reaction from I^- to I_2 and the reduction reaction from IO_3^- to I^- has a linear relationship with the square root of the scan rate, which means that both reactions are limited by diffusion[36]. Therefore, the concentration of KI needs to be sufficiently high to allow the conversion from I^- to I_2 to happen. Likewise, it is likely that the amount of KIO_3 needs to be concentrated so that the conversion from IO_3^- to I^- can happen. Since the I^- concentration in the electrolyte is already high, such conversion is difficult when considering Le Chatelier's principle. Moreover, when the amount of oxygen is sufficient, the reduction reaction for IO_3^- can be neglected when it competes with ORR[84]. The reason why the reduction peak for IO_3^- was observed for the CV test with a Pt wire may be related to the low concentration of KI (0.33 M KI) for the CV test. IO_3^- adsorbed at the Pt wire during the test, providing sufficient concentration for the reduction reaction. Therefore, it is likely that ORR is dominating the discharging reaction and KIO_3 is accumulating during full cell cycling. However, the reaction on the Zn electrode is electrochemically reversible, as demonstrated by the CV tests shown in Figure 3.6f. Figure 3.8b shows a summary of the proposed ZAB reactions when KI is used as an additive for the electrolyte. The summary illustrates that Zn dissolution and redeposition occur as the battery cycles. ORR takes place during battery discharging, with the oxidization of I^- occurring during battery charging, resulting in an overall accumulation of IO_3^-. As such, in a ZAB that utilizes KI as an additive in the electrolyte, the battery is not fully rechargeable. Over time, there will be a depletion of I^- and likely precipitation of KIO_3.

(a)

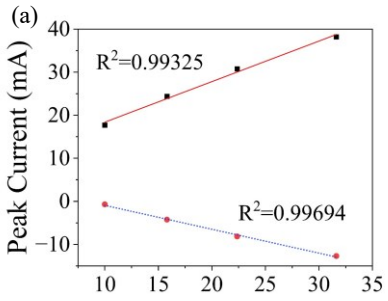

(b)

Discharge cycle

Air Cathode $O_2 + 2H_2O + 4e^- \rightarrow 4OH^-$

Zinc Anode $2Zn_{(s)} + 8OH^- \rightarrow 2Zn(OH)_4^{2-} + 4e^-$

Cell Overall $2Zn_{(s)} + 4OH^- + O_2 + 2H_2O \rightarrow 2Zn(OH)_4^{2-}$

Charge cycle

Air Anode $6I^- \rightarrow 3I_2 + 6e^-$

$3I_2 + 6OH^- \rightarrow IO_3^- + 5I^- + 3H_2O$

Zinc Cathode $3Zn(OH)_4^{2-} + 6e^- \rightarrow 3Zn_{(s)} + 12OH^-$

Cell Overall $I^- + 3Zn(OH)_4^{2-} \rightarrow 3Zn_{(s)} + IO_3^- + 3H_2O + 6OH^-$

Net Cycle Reaction

Discharge $6Zn_{(s)} + 12OH^- + 3O_2 + 6H_2O \rightarrow 6Zn(OH)_4^{2-}$

\+

Charge $2I^- + 6Zn(OH)_4^{2-} \rightarrow 6Zn_{(s)} + 2IO_3^- + 6H_2O + 12OH^-$

$2I^- + 3O_2 \rightarrow 2IO_3^-$

Figure 3.8. (a) Peak current vs. square root of scan rate for $I^- \rightarrow I_2$ (red solid line, black squares) and $IO_3^- \rightarrow I^-$ (blue dotted line, red circles). This plot was created by using the data in Figure 3.5c. (b) Proposed battery reactions for ZABs utilizing KI as an additive for the electrolyte.

3.3.4. Electrochemical Performance of ZABs using GPE-KOH-KI

Figure 3.9a shows rate tests for ZABs using GPE-KOH-KI at different test conditions. Since the cyclability of the battery was not good when GDL coated with $(Co,Fe)_3O_4$ was used as the air electrode with aqueous electrolyte containing KI, CC coated with Pt/RuO_2 was used for ZABs with GPE-KOH-KI. Other test conditions and battery configuration were the same as for ZABs using GPE-KOH. CC coated with Pt/RuO_2 was not used as the air electrode for ZABs using GPE-KOH because, as illustrated in Figure S3.1c and Figure S3.4a, the battery performance was much worse than that obtained using GDL coated with $(Co,Fe)_3O_4$. Table 3.3 summarizes battery efficiencies as well as peak power densities for ZABs using GPE-KOH-KI under different conditions. Battery efficiencies and power densities decreased with a decrease in temperature, due to reduced reaction kinetics and lower ionic conductivity. Table 3.4 summarizes the improvement in battery efficiency when compared with ZABs using GPE-KOH. Figure S3.4a shows a

comparison of rate test results obtained using GPE-KOH with different air electrodes. As exhibited in the figure, the ZAB using GPE-KOH with $(Co,Fe)_3O_4$ coated GDL had better performance at all current densities. Therefore, battery efficiency improvement calculations were done based on the results obtained using $(Co,Fe)_3O_4$ coated GDLs. Figure S3.3 shows comparisons of rate test results obtained using GPE-KOH and GPE-KOH-KI. With the change in charging reaction from the traditional OER to the oxidization of I^- to IO_3^-, battery efficiencies were greatly improved because of a reduction in charging voltage. When tested at 21℃ and 20 mA cm^{-2}, the charging voltage dropped from 2.0 V to 1.7 V (15% improvement). However, the ZAB using GPE-KOH-KI had a lower battery efficiency when tested at −41℃ and 10 mA cm^{-2}, due to the much lower discharging voltage. The peak power densities for ZAB using GPE-KOH-KI are also smaller than those for ZABs using GPE-KOH except at −3℃, where the ZAB using GPE-KOH-KI exhibited a peak power density of 72 mW cm^{-2} and the value for ZAB using GPE-KOH was 38 mW cm^{-2}. The lower discharging voltage and smaller peak power density have been attributed to I^- occupying ORR active sites[48].

Figure 3.9c to Figure 3.9e show GCD curves of cyclability tests for ZABs using GPE-KOH-KI. Similar to the GCD curves for the cyclability tests for ZABs using GPE-KOH, there were fluctuations of the discharge and charge voltages when tested at low temperatures due to temperature fluctuations inside the freezers. Table 3.5 summarizes initial and final efficiencies of the cyclability tests for ZABs using GPE-KOH-KI. When cycled at 2 cm^{-2} and 5 mA cm^{-2}, the ZABs using GPE-KOH-KI demonstrated excellent battery cyclability (100 h for both current densities) at all temperatures with impressive initial (77% and 74%, respectively) and final (73% and 66%, respectively) battery efficiencies at 21℃. Table 3.6 shows a summary of battery efficiency improvement for ZABs using GPE-KOH-KI compared with ZABs using GPE-KOH. Figure S3.5 to Figure S3.7 show comparisons of the cyclability test results. When tested at 2 mA cm^{-2} and 5 mA cm^{-2}, the improvement in initial battery efficiency was between 13% and 33% and 8% to 36% for the final battery efficiency. However, when cycled at 10 mA cm^{-2}, the cyclability of ZABs using GPE-KOH-KI was not as good as ZABs using GPE-KOH. The ZAB using GPE-KOH-KI cycled for 72 h at −28℃ before battery failure, whereas the ZAB using GPE-KOH cycled for 100 h under the same test conditions. Moreover, the difference in battery initial and final efficiency when tested at 21℃ and 10 mA cm^{-2} was much larger (nearly 20%) for the ZAB using GPE-KOH-KI than for the ZAB using GPE-KOH (10%). The poorer battery cyclability at

10 mA cm^{-2} for GPE-KOH-KI could be attributed to dendrite formation and passivation at the Zn electrode. Figure 3.9f shows an optical image comparing a Zn electrode cycled for 100 h at 21℃ and 10 mA cm^{-2} using GPE-KOH-KI and a Zn electrode cycled for 144 h under the same conditions using GPE-KOH. The surface of the Zn electrode obtained from the test using GPE-KOH is much smoother than the one obtained from the test using GPE-KOH-KI, even though the sample obtained using GPE-KOH was cycled for 44 h more. SEM and EDX spectroscopy were used to characterize the Zn electrode surface after cycling. As illustrated in Figure 3.10, the Zn surface obtained using GPE-KOH-KI had large oxide particles attached to the surface, whereas the sample obtained using GPE-KOH and cycled for 144 h had more Zn exposed, with scattered small oxide particles attached to the surface. Therefore, the poorer cyclability of the battery using GPE-KOH-KI at 10 mA cm^{-2} was likely due to passivation which formed an insulating layer at the Zn electrode that eventually made Zn dissolution and redeposition more difficult as cycling proceeded. Nevertheless, the use of GPE-KOH-KI in a ZAB still demonstrates advantages over aqueous electrolytes containing KI and GPE-KOH. The use of GPE-KOH-KI successfully prevented deterioration of Zn caused by dendrite formation, whereas a hole appeared in the Zn electrode when an aqueous electrolyte containing KI was used. Lowering the charging voltage by altering the charging reaction successfully improved battery efficiency in most conditions. Table 3.7 shows comparisons of battery performance for GPE-KOH and GPE-KOH-KI and the literature, where both GPEs have better battery performance relative to the competitors. Table S3.2 summarizes cyclability performance of ZABs using GPE-KOH and GPE-KOH-KI under different conditions.

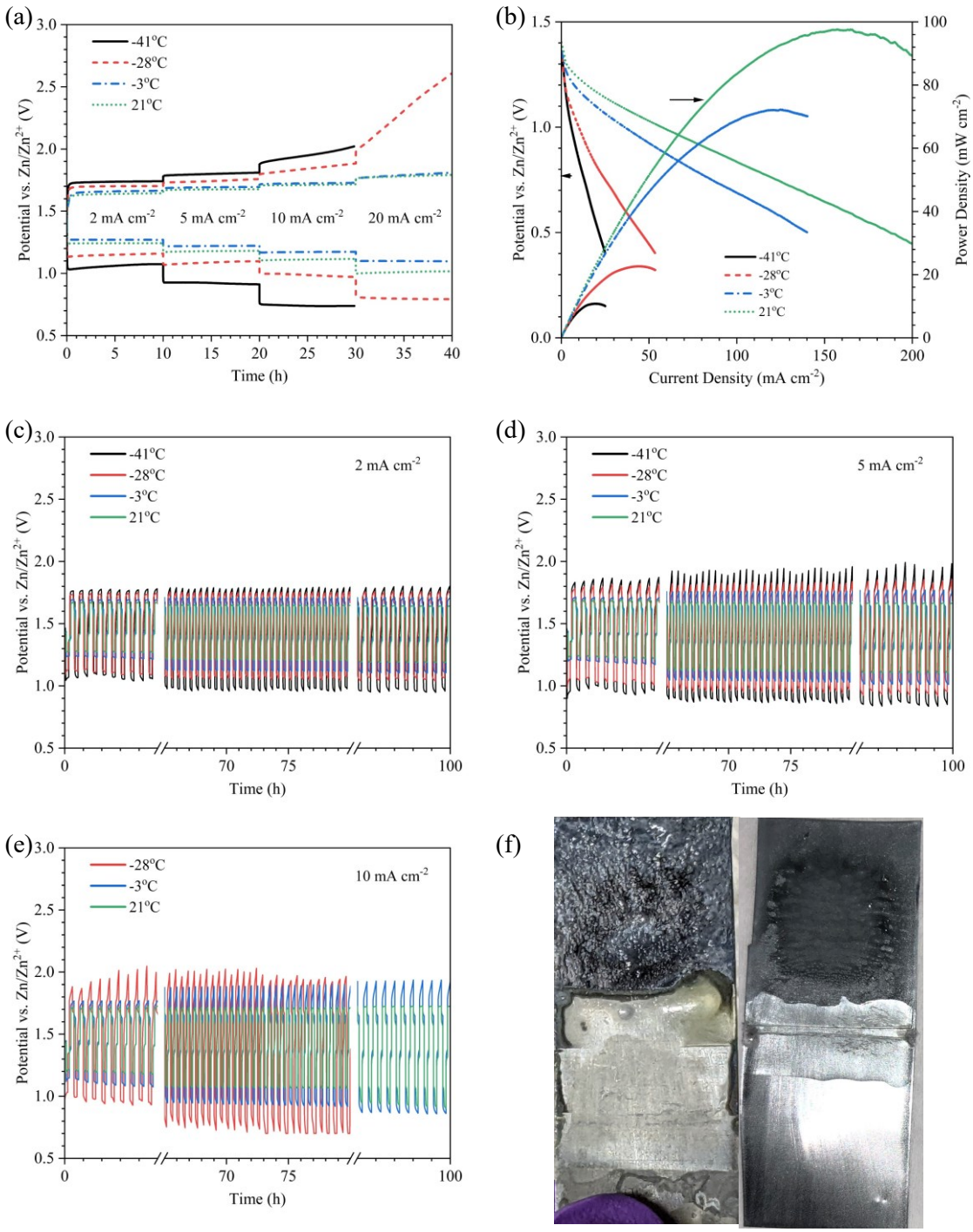

Figure 3.9. (a) Rate tests for ZABs using GPE-KOH-KI at different temperatures. (b) Discharge polarization curves and corresponding power densities. Cyclability tests at different temperatures for ZABs using GPE-KOH-KI at (c) 2 mA cm^{-2}, (d) 5 mA cm^{-2}, and (e) 10 mA cm^{-2}. (f) Optical images of Zn foils after cycling for 100 h at 21℃ and 10 mA cm^{-2} using GPE-KOH-KI (left) and cycled for 144 h at 21℃ and 10 mA cm^{-2} using GPE-KOH (right).

Table 3.3. Summary of rate test battery efficiencies and power densities for ZABs using GPE-KOH-KI under different test conditions

	Efficiency at different current densities (%)				
Temperature (°C)	2 mA cm^{-2}	5 mA cm^{-2}	10 mA cm^{-2}	20 mA cm^{-2}	Peak power density (mW cm^{-2})
21	80	77	73	67	98
-3	76	72	68	61	72
-28	68	63	54	31	22
-41	61	50	37	Failed	11

Table 3.4. Summary of rate test battery efficiency improvement for ZABs using GPE-KOH-KI under different testing conditions when compared with ZABs using GPE-KOH

	Efficiency improvement at various current densities (%)			
Temperature (°C)	2 mA cm^{-2}	5 mA cm^{-2}	10 mA cm^{-2}	20 mA cm^{-2}
21	18	15	16	14
-3	19	20	26	36
-28	17	24	26	15
-41	11	2	-10	Both failed

Table 3.5. Summary of cyclability test battery efficiencies for ZABs using GPE-KOH-KI under different test conditions

	2 mA cm^{-2}		5 mA cm^{-2}		10 mA cm^{-2}	
Temperature (°C)	Initial Efficiency (%)	Final Efficiency (%)	Initial Efficiency (%)	Final Efficiency (%)	Initial Efficiency (%)	Final Efficiency (%)
21	77	73	74	66	71	52
-3	73	65	71	57	65	45
-28	65	61	60	52	55	Failed
-41	61	53	52	43	Failed	Failed

Table 3.6. Summary of cyclability test initial and final battery efficiency improvements for ZABs using GPE-KOH-KI under different test conditions when compared with ZABs using GPE-KOH

	2 mA cm^{-2}		5 mA cm^{-2}		10 mA cm^{-2}	
Temperature (°C)	Initial Efficiency (%)	Final Efficiency (%)	Initial Efficiency (%)	Final Efficiency (%)	Initial Efficiency (%)	Final Efficiency (%)
21	13	22	16	16	13	-2
-3	16	10	20	8	10	-13
-28	12	13	20	21	10	None
-41	33	36	24	34	N/A	N/A

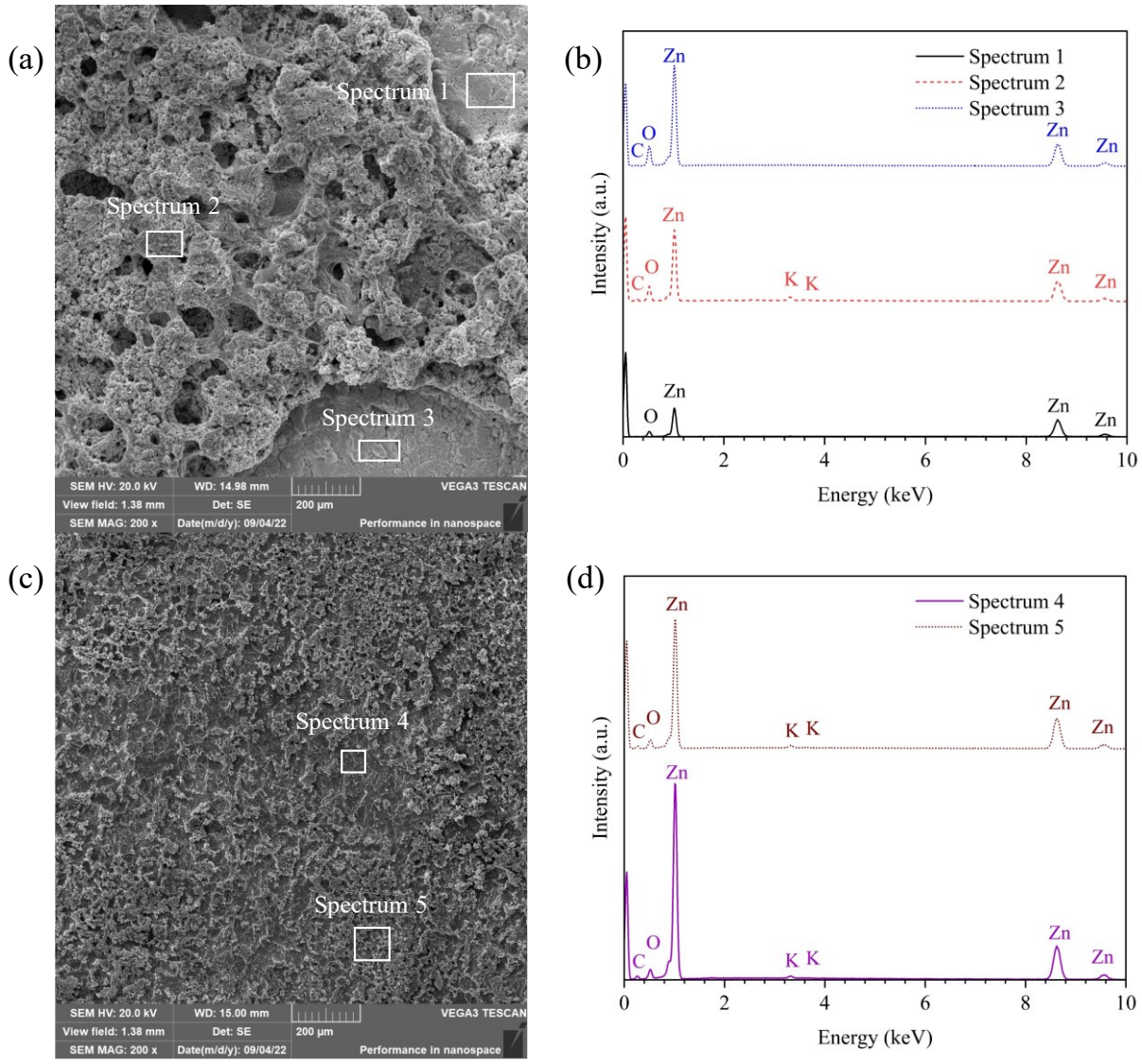

Figure 3.10. (a) SEM SE image of the Zn electrode obtained using GPE-KOH-KI and (b) EDX spectra from the regions indicated. (c) SEM SE image of the Zn electrode obtained using GPE-KOH and (d) EDX spectra from the regions indicated.

Table 3.7. Comparison of ZABs using GPEs reported in this work and in the literature

Electrolyte	Current Density (mA cm^{-2})	Temp. (℃)	Catalyst	Maximum Power Density (mW cm^{-2})	Initial Battery Efficiency (%)	Cycling Time (h)	Ref.
GPE-KOH	2	21	$(Co,Fe)_3O_4$	127	68	100	This work
		-28		17	58	100	
		-41		11	46	100	
	10	21		127	61	260	
GPE-KOH-KI	2	21	Pt/RuO_2	98	77	100	
		-28		22	65		
		-41		11	61		
	5	21		98	77		
PAM-PAA	1	25	Pt/RuO_2	11.8	66	10	26
		-20		8.2	55	10	
Cellulose-PAA	2	25	MnO_2, Co_3O_4	40.25	69	11	89
PAM	5	25	MnO_2, GO	105	63	23.3	90
PVA	3	25	Co_3O_4	62.6	63	48	91
PAA	2	25	FeCo based catalyst	160	65	105	28
	5	25			~60	80	
	2	-20		80.5	57	5	
PAMPS-K/MC	1	25	Co_3O_4	73.9	64	24	70
		0		N/A	~60		
		-20		54.2	~55		
PAM-KI	2	20	Pt/RuO_2	43	71	75	48
		-40		10	59	40	
PANa-starch	1	25	Pt/RuO_2	67.5	68	28.7	92
		-20		30.7	~53	44.1	
PAA	2	25	FeCo based catalyst	128.8	65.9	92	93
		-30		63.6	60.4	92	
PANa	2	25	Pt/RuO_2	88	65.5	160	94
PANa-cellulose	5	25	Fe based	108.6	60	110	95
PVA-GG	2	25	Pt/IrO_2	50	~60	10	96
PVA	1	25	Co_3O_4	N/A	~38	70	97
PVA	1	25	Co_3O_4	16	~39	40	98
PVA-PAA-GO-KI	2	25	$Pt/C+Co_3O_4$	78.6	73	200	75
Aqueous 6 M KOH+3 M KI+0.2 M Zn(Ac)2	5	25	Pt/C	148.8	76.5	80	85
PEVA	2	25	Co_3O_4	N/A	~60	230	99

Abbreviations:

PAMPS-K/MC: poly(2-acrylamido-2-methylpropanesulfonic acid potassium salt) with methyl cellulose

PANa-starch: sodium polyacrylate-starch

GG: guar hydroxypropyltrimonium chloride

GO: graphene oxide

PEVA: poly(ethylene vinyl acetate)

3.4. Conclusions

In summary, both GPE-KOH and GPE-KOH-KI demonstrated competitive battery performance at various current densities and temperatures. The use of GPE-KOH-KI in the battery successfully prevented deterioration of the Zn electrode. The addition of KI to the electrolyte changed the path of the charging reaction from the traditional OER to the oxidation reaction of I^- to IO_3^-, which has a lower thermodynamic barrier. As such, the charging voltage was significantly reduced, and this led to greatly improved battery efficiency. However, the cyclability of the battery using GPE-KOH-KI at a current density of 10 mA cm^{-2} was not as good as the ZAB using GPE-KOH when tested at 21℃. The ZAB using GPE-KOH was able to cycle for 260 h at 21℃ and 10 mA cm^{-2}, whereas the ZAB using GPE-KOH-KI showed accelerated performance degradation after 90 h under the same test conditions. It is likely that the addition of KI to the electrolyte transforms the traditional ZAB to a battery where only the reaction at the Zn electrode is reversible and KIO_3 accumulates as the battery cycles, making the battery not fully rechargeable. Nevertheless, the addition of KI to the electrolyte for ZABs provides a new strategy in terms of designing ZABs, but further studies on the reaction mechanism at the air electrode are needed.

3.5. Supporting Information

3.5.1. Calculation Details

Conversion of concentration of KOH to atomic percent.

Molecular weight:

$$\mathrm{KOH}: 56\ \mathrm{g\ mol^{-1}} \qquad \mathrm{H_2O}: 18\ \mathrm{g\ mol^{-1}}$$

$$\mathrm{K}: 39\ \mathrm{g\ mol^{-1}} \qquad \mathrm{H}: 1\ \mathrm{g\ mol^{-1}} \qquad \mathrm{O}: 16\ \mathrm{g\ mol^{-1}}$$

The density of a 6 M KOH aqueous solution from the CRC Handbook of Chemistry and Physics[100] is 1.253 g mL^{-1}.

The volume of the 6 M KOH aqueous solution is assumed to be 1 L.

The weight of the 6 M KOH aqueous solution is:

$$1.253\,\frac{\mathrm{g}}{\mathrm{mL}} \times \frac{1000\ \mathrm{mL}}{1\ \mathrm{L}} = 1253\ \mathrm{g}$$

The weight of KOH required to prepare a 6 M solution is:

$$56.1\,\frac{\mathrm{g}}{\mathrm{mol}} \times 6\,\frac{\mathrm{mol}}{\mathrm{L}} \times 1\ \mathrm{L} = 336.6\ \mathrm{g}$$

The weight of $\mathrm{H_2O}$ in the 6 M KOH aqueous solution is:

$$1253\ \mathrm{g} - 336.6\ \mathrm{g} = 916.4\ \mathrm{g}$$

The weight contributed by element K is:

$$\frac{39\ \mathrm{g\ mol^{-1}}}{56\ \mathrm{g\ mol^{-1}}} \times 336.6\ \mathrm{g} = 234.4\ \mathrm{g}$$

The conversion to moles is given as:

$$234.4\ \mathrm{g} \div 39\,\frac{\mathrm{g}}{\mathrm{mol}} = 6\ \mathrm{mol}$$

The weight contributed by element O is:

$$\frac{16\ \text{g mol}^{-1}}{56\ \text{g mol}^{-1}} \times 336.6\ \text{g} + \frac{16\ \text{g mol}^{-1}}{18\ \text{g mol}^{-1}} \times 916.4\ \text{g} = 910.7\ \text{g}$$

The conversion to moles is:

$$910.7\ \text{g} \div 16 \frac{\text{g}}{\text{mol}} = 56.92\ \text{mol}$$

The weight contributed by element H is:

$$\frac{1\ \text{g mol}^{-1}}{56\ \text{g mol}^{-1}} \times 336.6\ \text{g} + \frac{2 \times 1\ \text{g mol}^{-1}}{18\ \text{g mol}^{-1}} \times 916.4\ \text{g} = 107.8\ \text{g}$$

The conversion to moles is:

$$107.8\ \text{g} \div 1 \frac{\text{g}}{\text{mol}} = 107.8\ \text{mol}$$

The total amount of moles is:

$$6\ \text{mol} + 56.92\ \text{mol} + 107.8\ \text{mol} = 170.7\ \text{mol}$$

The mole percent of K is:

$$6\ \text{mol} \div 170.7\ \text{mol} \times 100 = 3.515\ \text{at\%}$$

Weight of PAA obtained from the 4 mL GPE-KOH sample:

$$0.342\ \text{g}$$

Density of PAA[101]:

$$1.22\ \text{g cm}^{-3}$$

$$\text{Volume of PAA} = \frac{\text{Weight of PAA}}{\text{Density of PAA}} = \frac{0.342\ \text{g}}{1.22\ \text{g cm}^{-3}} = 0.28\ \text{cm}^3 = 0.28\ \text{mL}$$

Volume fraction occupied by PAA in GPE-KOH:

$$\frac{0.28\ \text{mL}}{4\ \text{mL}} \times 100\% = 7\%$$

Table S3.1. Ionic mobility of selected ions in water

Ion	Mobility (10^{-8} m^2 s^{-1} V^{-1})	Reference
K^+	7.62	102
OH^-	20.64	102
I^-	6.23±0.04	103

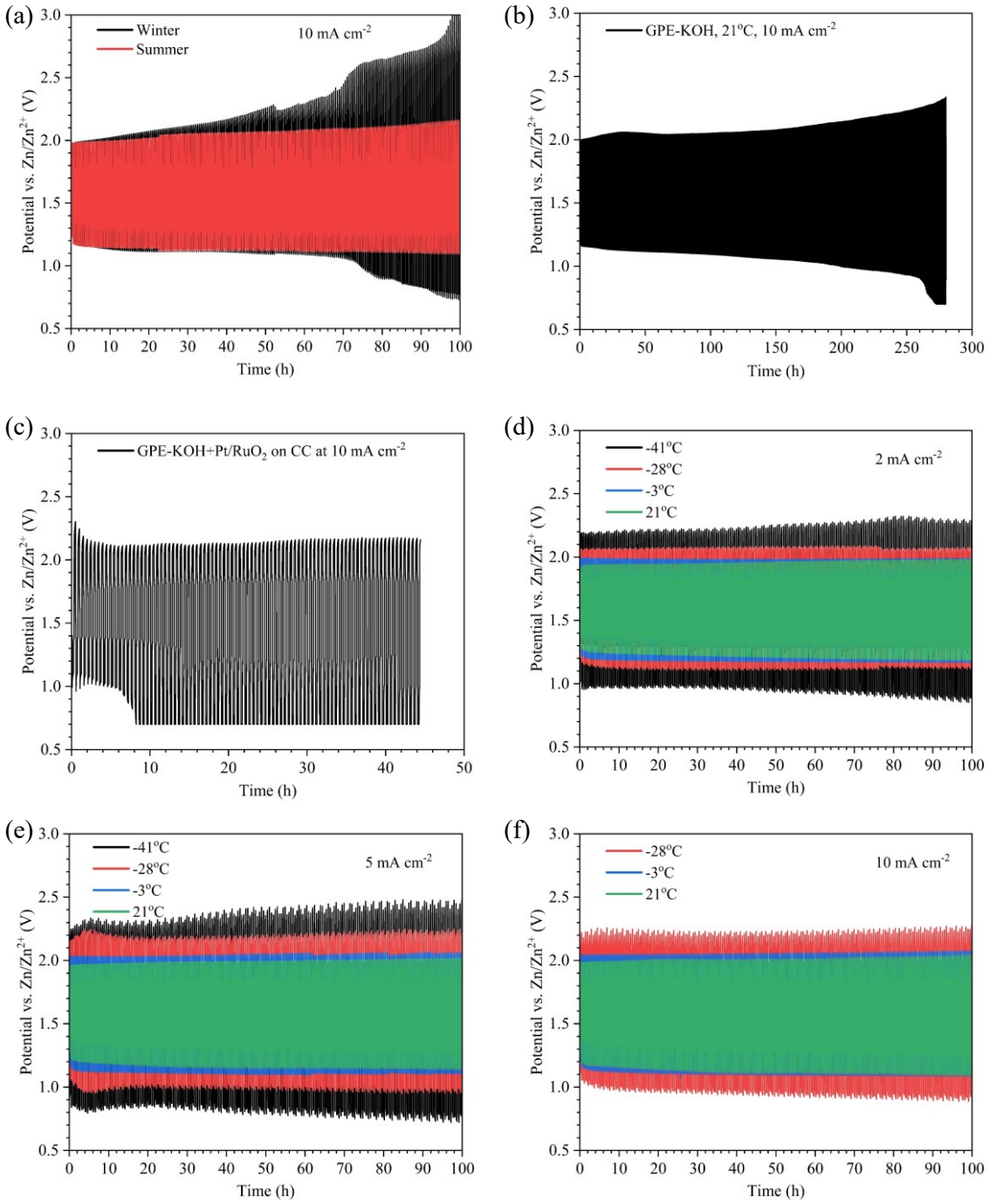

Figure S3.1. (a) Cyclability test at 21℃ and 10 mA cm^{-2} for ZAB using GPE-KOH in different seasons. (b) Full view of the lifetime test for ZAB using GPE-KOH. (c) Cyclability test at 21℃ and 10 mA cm^{-2} for ZAB using GPE-KOH and Pt/RuO_2 coated CC as the air electrode. Cyclability tests at different temperatures for ZABs using GPE-KOH and $(Co,Fe)_3O_4$ coated GDL at (d) 2 mA cm^{-2}, (e) 5 mA cm^{-2}, (f) 10 mA cm^{-2}.

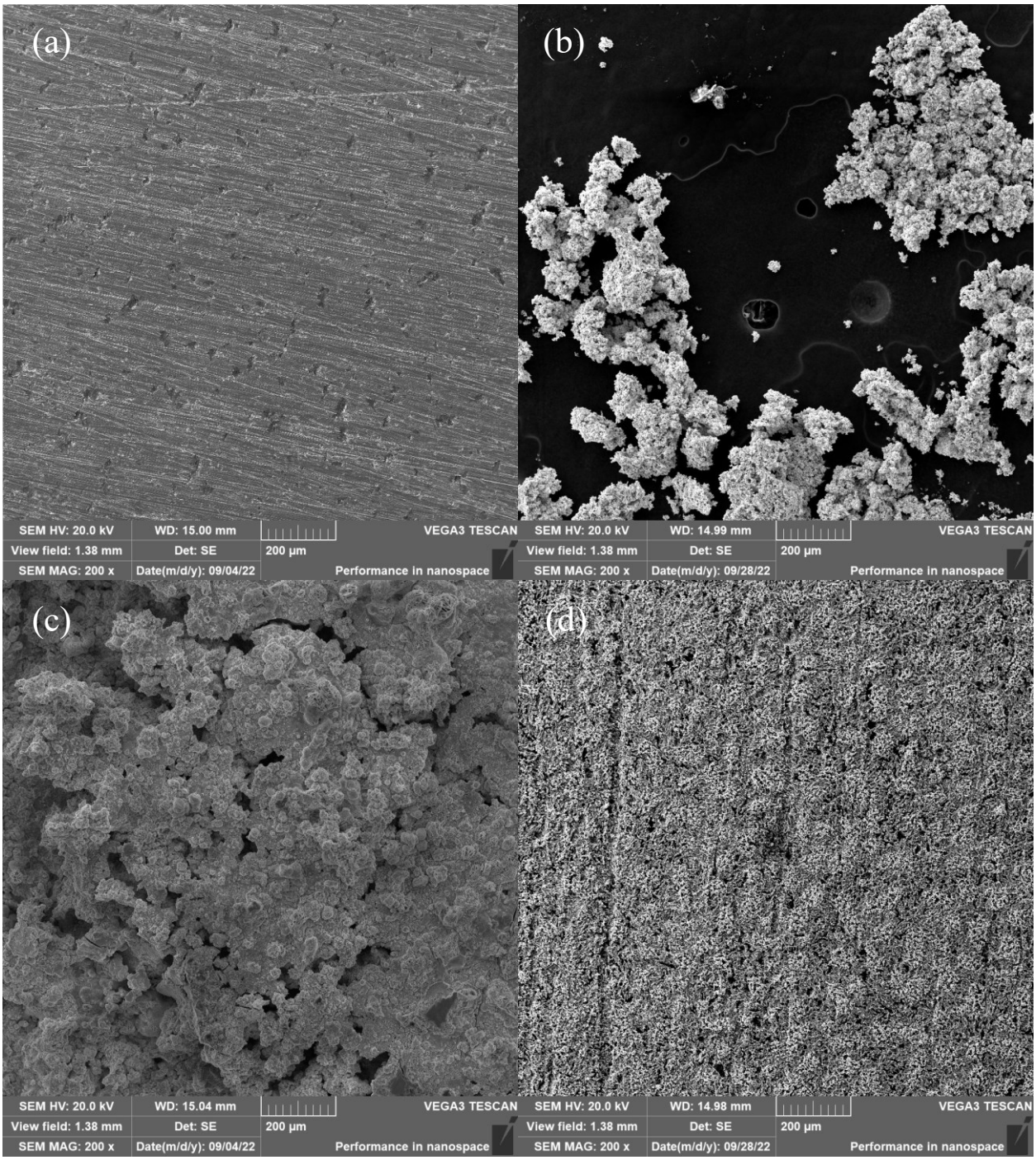

Figure S3.2. SEM SE images of (a) ground Zn foil, (b) particles at the bottom of the cell, (c) Zn electrode after cycling in aqueous 6 M KOH+2 M KI+0.4 M ZnO, and (d) Zn electrode after cycling in aqueous electrolyte without KI and Pt/RuO_2 coated GDL at 10 mA cm^{-2} for 100 h.

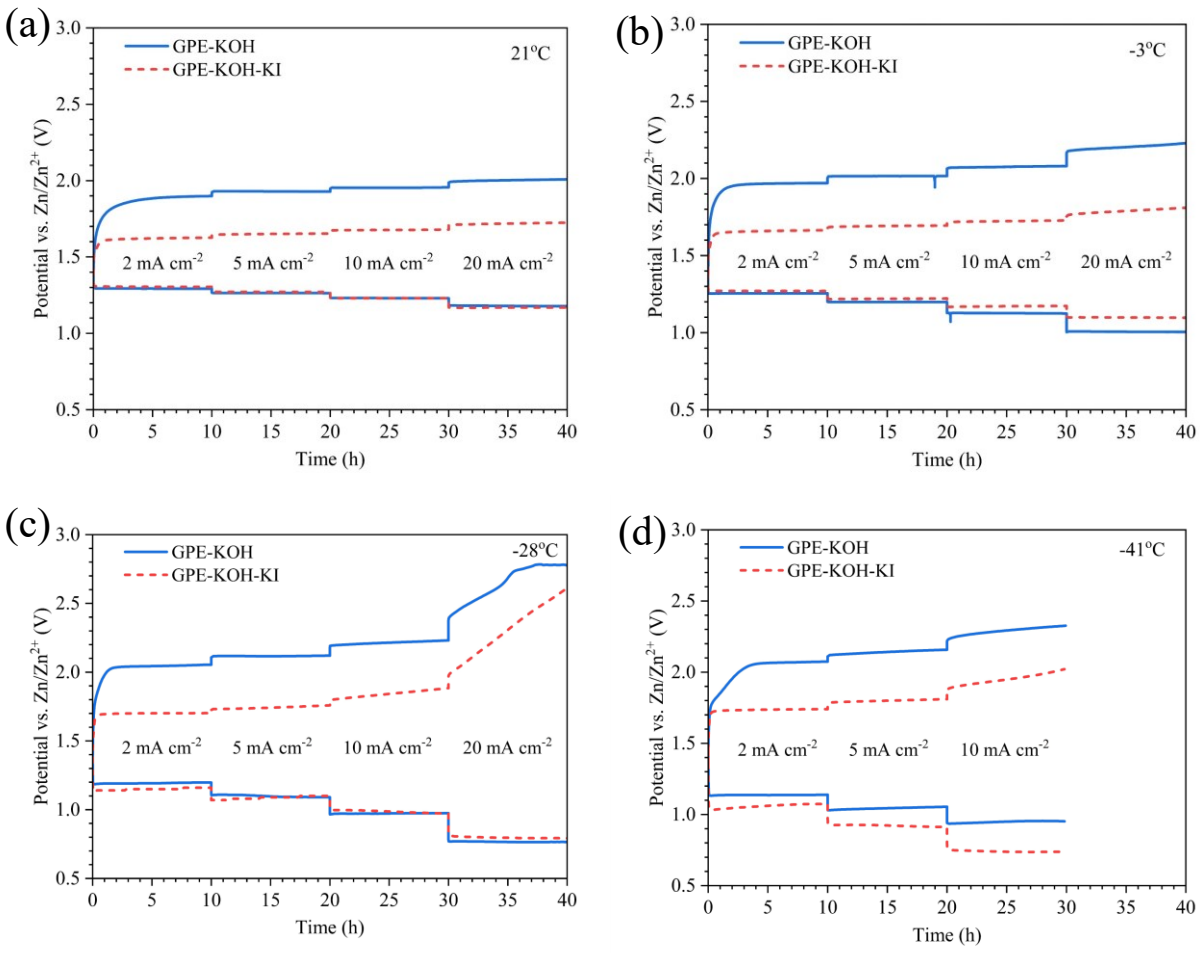

Figure S3.3. Comparison of rate test results for ZABs using $(Co,Fe)_3O_4$ coated GDL with GPE-KOH and Pt/RuO_2 coated CC with GPE-KOH-KI at (a) 21℃, (b) −3℃, (c) −28℃, and (d) −41℃.

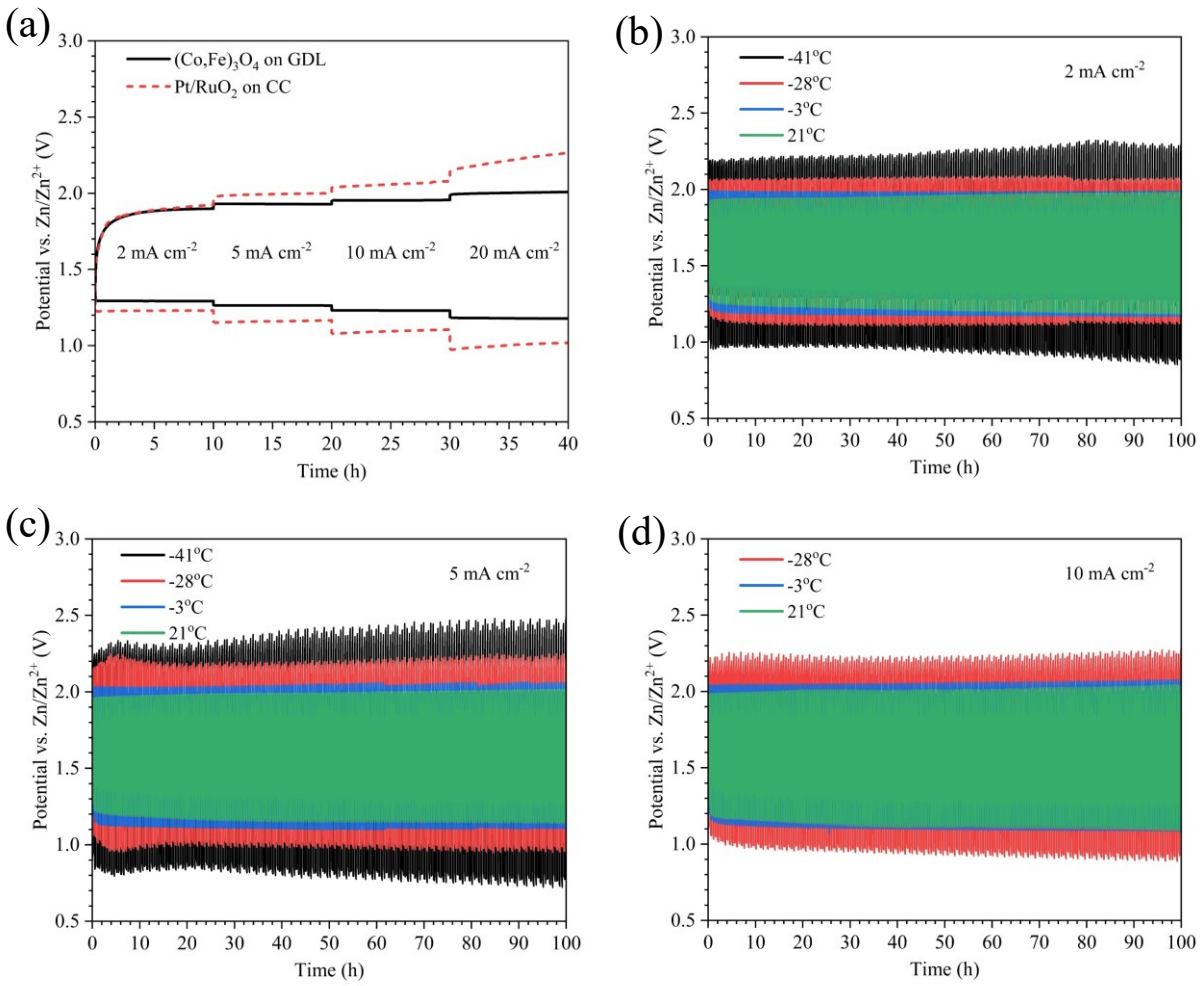

Figure S3.4. (a) Rate test results for ZABs using GPE-KOH with $(Co,Fe)_3O_4$ on GDL and Pt/RuO_2 on CC as the air electrode at 21℃. Cyclability tests at different temperatures for ZABs using GPE-KOH-KI and Pt/RuO_2 coated CC at (b) 2 mA cm^{-2}, (c) 5 mA cm^{-2}, and (d) 10 mA cm^{-2}.

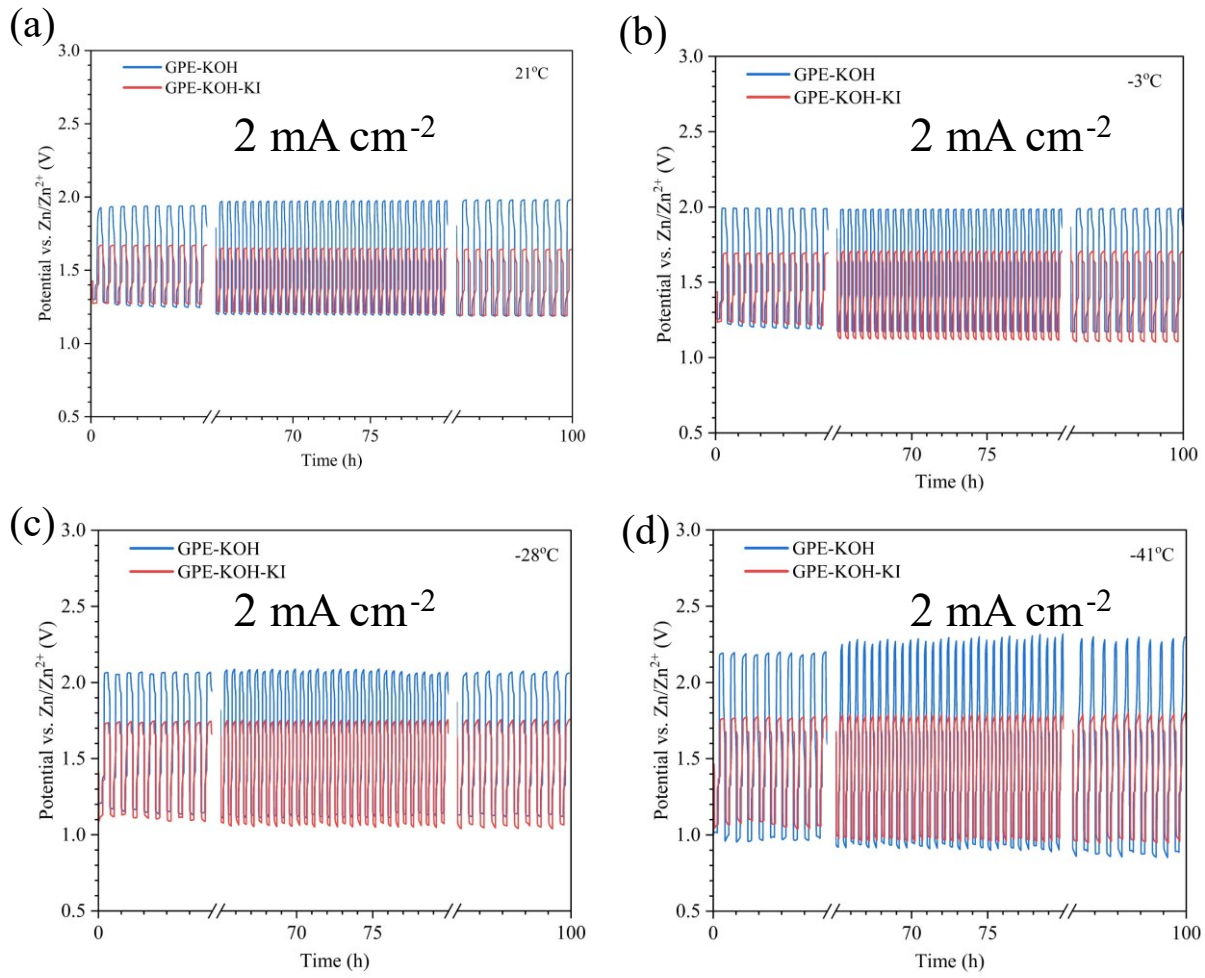

Figure S3.5. Cyclability test results for ZABs using $(Co,Fe)_3O_4$ coated GDL with GPE-KOH and Pt/RuO_2 coated CC with GPE-KOH-KI at 2 mA cm^{-2} at (a) 21℃, (b) −3℃, (c) −28℃, and (d) −41℃.

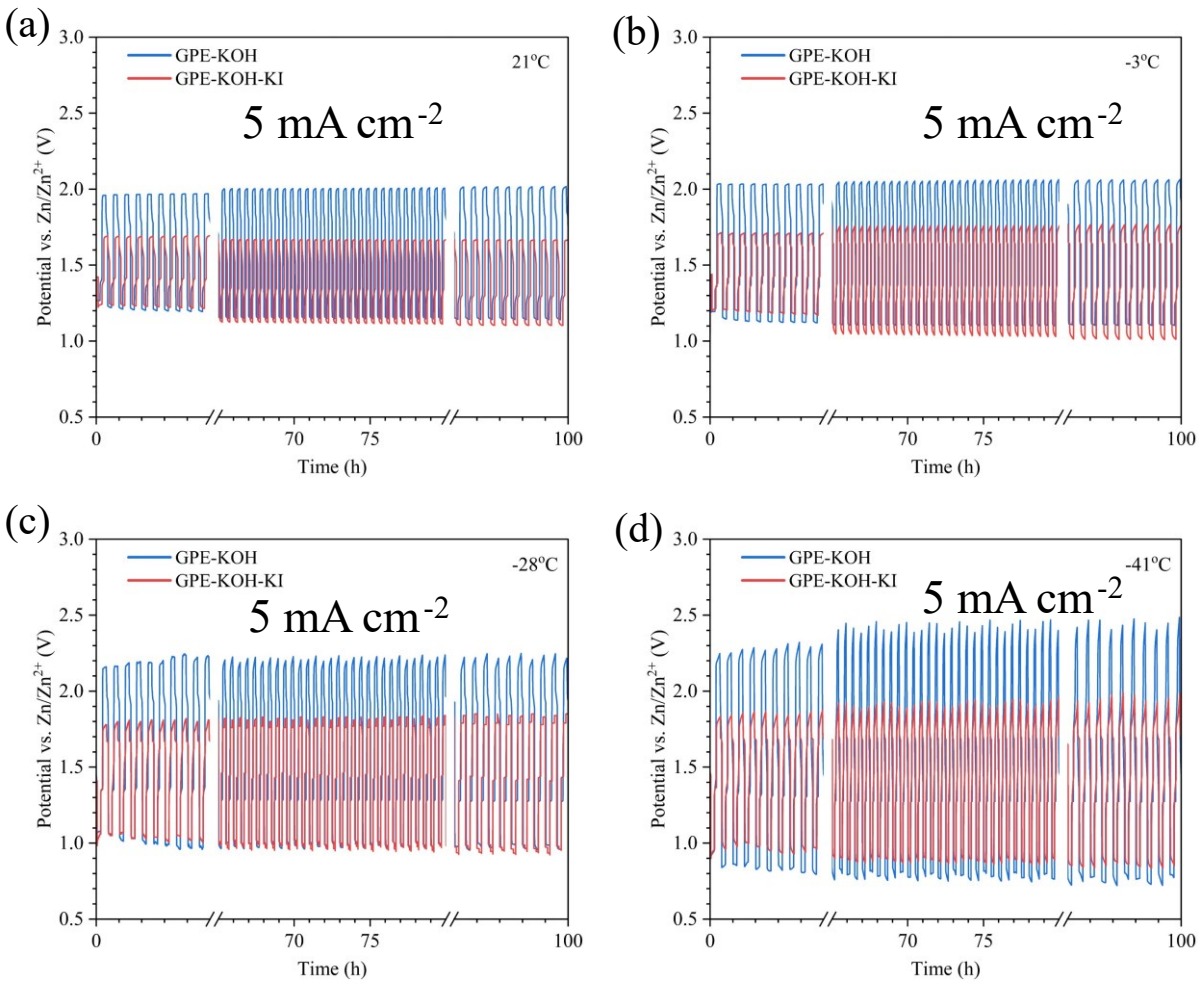

Figure S3.6. Comparison of cyclability test results for ZABs using $(Co,Fe)_3O_4$ coated GDL with GPE-KOH and Pt/RuO_2 coated CC with GPE-KOH-KI at 5 mA cm^{-2} at (a) 21℃, (b) −3℃, (c) −28℃, and (d) −41℃.

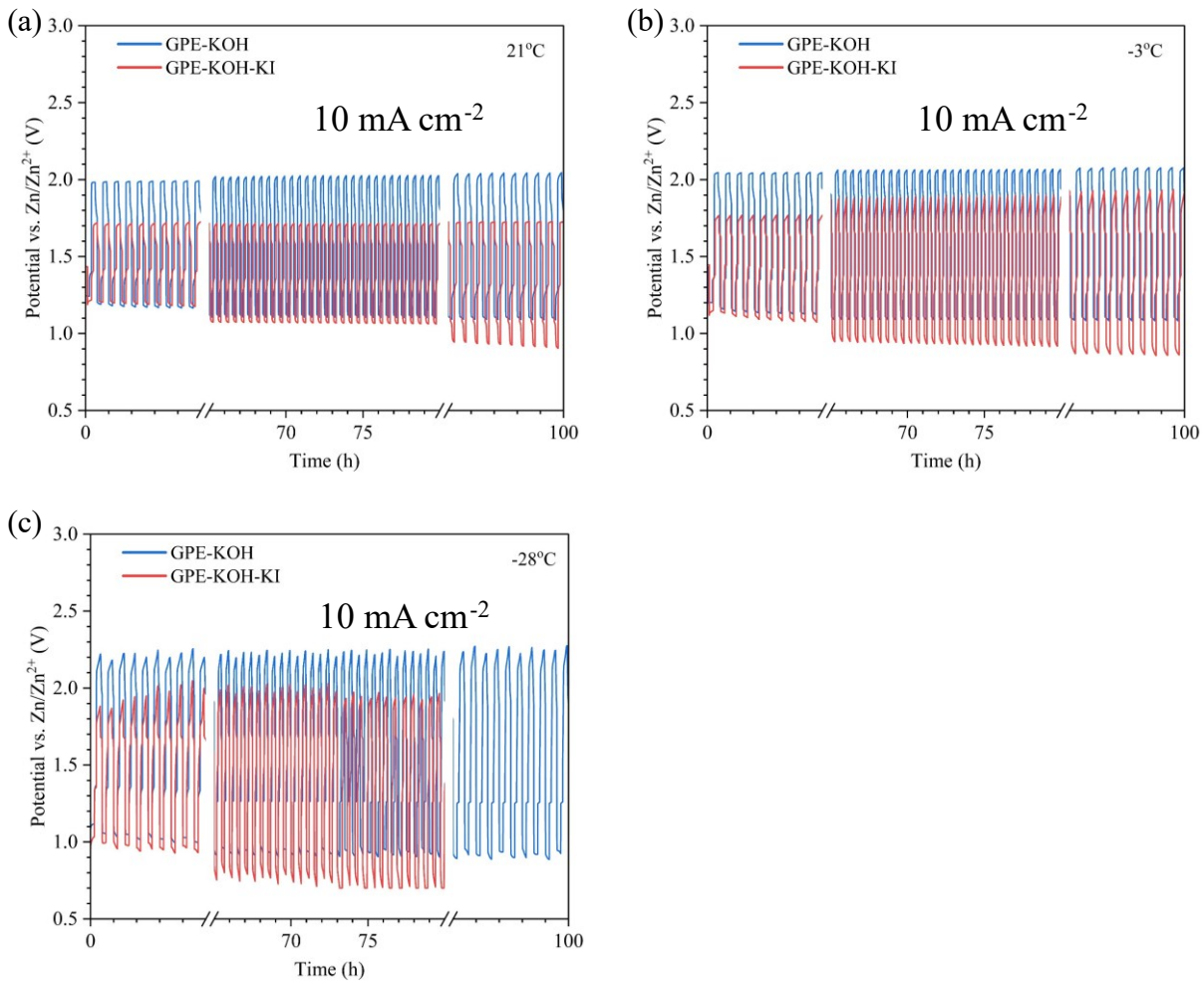

Figure S3.7. Cyclability test results for ZABs using $(Co,Fe)_3O_4$ coated GDL with GPE-KOH and Pt/RuO_2 coated CC with GPE-KOH-KI at 10 mA cm^{-2} at (a) 21℃, (b) −3℃, and (c) −28℃.

Table S3.2. Summary of cyclability performance of ZABs using GPE-KOH and GPE-KOH-KI under different conditions

GPE-KOH						
	2 mA cm^{-2}		5 mA cm^{-2}		10 mA cm^{-2}	
Temperature (°C)	Initial Efficiency (%)	Final Efficiency (%)	Initial Efficiency (%)	Final Efficiency (%)	Initial Efficiency (%)	Final Efficiency (%)
21	68	60	64	57	63	53
-3	63	59	59	53	59	52
-28	58	54	50	43	50	41
-41	46	39	42	32	Failed	Failed
GPE-KOH-KI						
	2 mA cm^{-2}		5 mA cm^{-2}		10 mA cm^{-2}	
Temperature (°C)	Initial Efficiency (%)	Final Efficiency (%)	Initial Efficiency (%)	Final Efficiency (%)	Initial Efficiency (%)	Final Efficiency (%)
21	77	73	74	66	71	52
-3	73	65	71	57	65	45
-28	65	61	60	52	55	Failed
-41	61	53	52	43	Failed	Failed

Chapter 4. In-situ Fabrication of Gel Polymer Electrolytes for Zn-air Batteries

4.1. Introduction

Recent record-breaking high temperatures during the summer throughout the world[104–106] indicate that global warming and climate change are real[107]. Approaches such as utilizing clean energy generated by wind or solar power are being considered as measures to help in the fight against climate change[108]. Batteries are reliable devices that can store electricity generated by wind or solar energy. Li-ion batteries (LIBs) are the most widely used commercial batteries on the market, but their high price make them less attractive for application in grid storage. Metal-air batteries, especially Zn-air batteries (ZABs), are more affordable solutions[4] because Zn is a more abundant material in the earth's crust than Li[109].

Gel polymer electrolytes (GPEs) are emerging electrolytes for ZABs that have good ionic conductivity and mechanical properties. They can also act as a separator in the battery and prevent short circuits caused by dendrite formation. However, compared with traditional aqueous electrolytes, ZABs using GPEs tend to experience higher interfacial resistance. This is because GPEs have lower electrolyte fluidity and wettability, which lead to poorer contact between the air electrode and the electrolyte. In contrast, aqueous electrolytes have better access to the high surface area of the air electrode including micropores[5]. To mediate this problem, in-situ fabrication of GPEs directly at the air electrode is proposed. In this method, precursor solutions are injected into a container where the air electrode is exposed to the precursor solution. Since the precursor solution exhibits a much lower viscosity than the GPE, it can take advantage of the high surface area of the air electrode better than the fabricated GPE. Then, the polymerization reaction takes place in the container, with the precursor solution in good contact with the air electrode[110]. In principle, batteries using GPEs synthesized by this method would be expected to demonstrate lower interfacial resistance and better battery cyclability, since the GPE has a better chance of infiltrating the micropores at the air electrode. This ideal scenario can be valid when the location of the tri-phase boundary (i.e, where the electrolyte, air, and carbon electrode meet) coincides with the locations of the catalysts.

The objectives of this part of the research study are to develop a precursor solution leak-free cell configuration for in-situ fabrication of a GPE within a ZAB and to investigate whether using in-situ fabrication of GPEs will lead to better battery cyclability.

4.2. Experimental Procedure

4.2.1.1. Synthesis of GPEs

Ex-situ and in-situ fabrication of GPE-KOH formulations were done. Acrylic acid (99.5%, stabilized with 200 ppm 4-methoxyphenol), KOH pellets, ZnO powder, a vortex mixer, transfer pipettes, 50 mL polypropylene conical tubes, and 5 mL polypropylene round-bottom tubes were purchased from Fisher Scientific. MBAA (99.5%) and KPS (99%) were purchased from Sigma-Aldrich.

The target precursor solution volume for GPE-KOH was 20 mL. The concentrations of each component added to the precursor solution for GPE-KOH were 6.5 M KOH, 0.2 M ZnO, 0.5 M acrylic acid, 0.03 M MBAA, and 0.0015 M KPS.

For ex-situ fabrication of GPE-KOH, 7.29 g KOH and 0.3256 g ZnO were added to a 50 mL conical tube and mixed with 12 mL deionized water (DIW) using a vortex mixer. Once all solids were dissolved and the temperature of the solution was at room temperature, 0.685 mL acrylic acid was added to the tube followed by another mixing and cooling step. 0.0925 g MBAA and 0.008 g KPS were then added. More DIW was added to reach the 20 mL target. The solution was mixed vigorously for about 2 min before transferring to round-bottom tubes using a transfer pipette with each tube containing 4 mL of precursor solution. The tubes were then kept in an oven at 65℃ for 1 h to complete polymerization. The prepared GPEs were air cooled to room temperature overnight before use.

For in-situ fabrication of GPE-KOH, instead of transferring the precursor solution to round-bottom tube, the solution was transferred to a 3D-printed cell (Figure 4.1a) which contained the air electrode. All other procedures for in-situ fabrication of GPE-KOH were the same as for ex-situ fabrication.

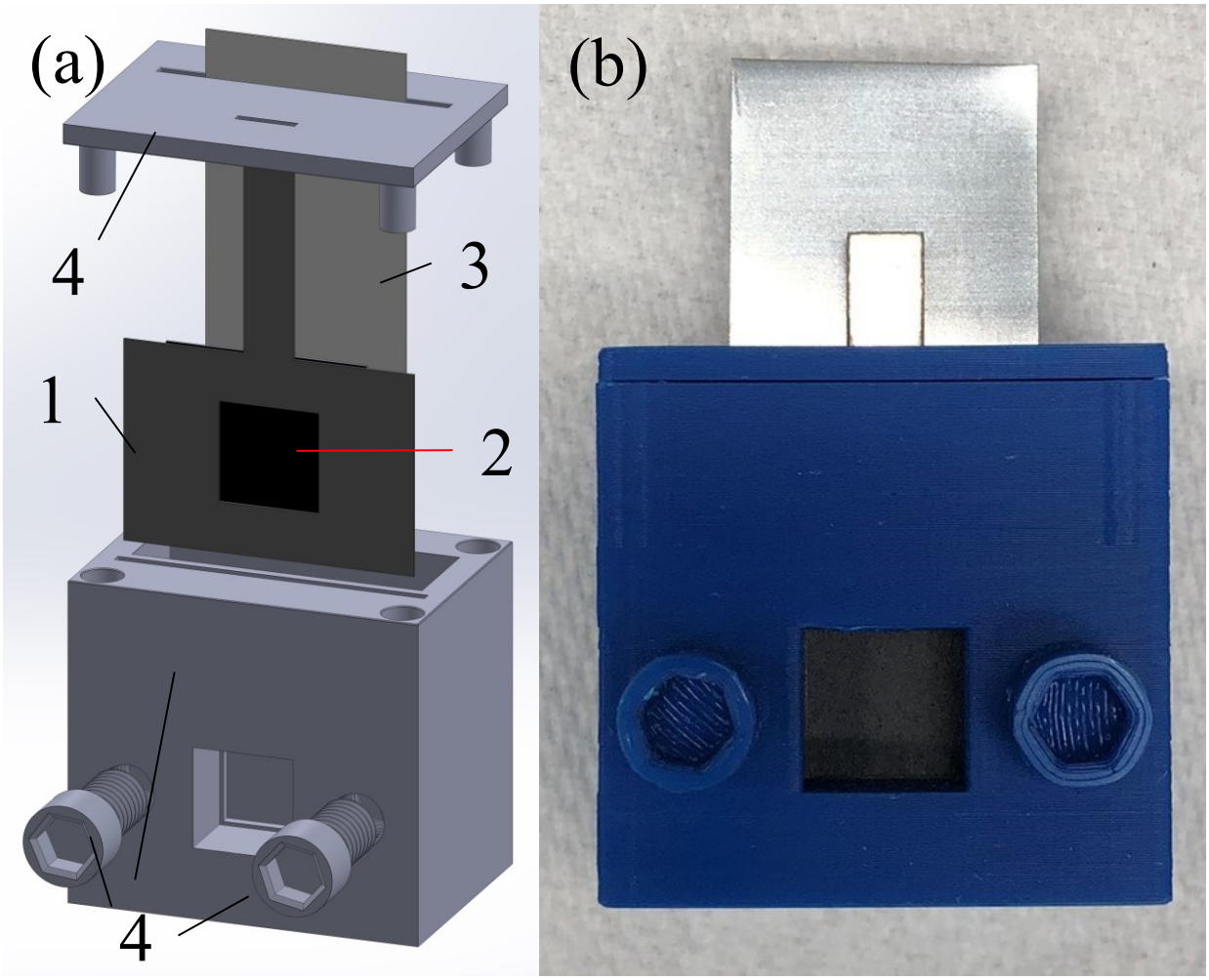

Figure 4.1. (a) 3D-printed cell in a disassembled view. (b) Optical image of the assembled 3D-printed cell. Note that the numbers correspond to the following: 1) Ni current collector, 2) GDL coated with electrocatalyst, 3) Zn foil, and 4) 3D-printed parts using ABS.

4.2.1.2. Synthesis of Electrocatalysts

$(Co,Fe)_3O_4$ decorated nitrogen-doped carbon nanotubes (N-CNTs) were used as electrocatalysts for this work. The synthesis procedure is the same as described in Section 3.2.1.2. Synthesis of Electrocatalysts.

4.2.1.3. Cell Fabrication

A sandwich-type cell and a 3D-printed cell were used with GPEs synthesized using ex-situ fabrication and in-situ fabrication, respectively. Cell configurations, as well as details about cell

fabrication, are shown in Section 3.2.1.3. Cell Fabrication. Prior to electrochemical tests, the Zn electrode was squeezed into the 3D-printed cell (illustrated in Figure S4.1e). An aqueous electrolyte containing 6 M KOH+0.2 M ZnO was used to fill any space between the Zn electrode and the GPE synthesized using in-situ fabrication. Then the cell was left at room temperature and ambient air for 1 h before testing.

4.2.1.4. Materials Characterization

A Tescan VEGA3 SEM coupled with an energy dispersive X-ray (EDX) spectrometer was used to reveal the degree of penetration of GPE into the air electrode. The accelerating voltage used was 20 kV for both SEM and EDX analyses. To obtain an air electrode sample from the sandwich-type cell, a full cell was first assembled and then left at room temperature in ambient air for 1 h to allow the GPE to penetrate into the air electrode. The cell was then disassembled, and the air electrode was removed. For the 3D-printed cell, the cell was fabricated in-situ and then left overnight before disassembly and removal of the air electrode. Both air electrodes were dried in a sealed container with desiccant for 1 week before doing SEM and EDX analysis.

4.2.1.5. Electrochemical Measurements

All electrochemical measurements were done using BioLogic VSP-100 and SP300, as well as Arbin LBT20084, potentiostats at room temperature. All batteries were left in the ambient environment for 1 h before any full cell testing to allow the GPE to wet the air electrode (for ZABs using ex-situ fabricated GPE) and to let the GPE absorb the aqueous electrolyte (for ZABs using in-situ fabricated GPE). During galvanostatic charge – discharge rate tests, batteries were discharged at 2, 5, 10, and 20 mA cm^{-2} for 10 min at each current density, followed by a 10 min rest period before charging at the same current densities for 10 min each. For galvanostatic charge – discharge cyclability tests, batteries were cycled at 2, 5, and 10 mA cm^{-2}; and each cycle was 30 min long and was composed of a sequence of 10 min discharging, 5 min rest, 10 min charging, and 5 min rest. Battery efficiencies for both rate tests and cyclability were calculated using the following equation.

$$\eta = \frac{E_{discharge}}{E_{charge}} \times 100\% \qquad (4-1)$$

where η is the battery voltage efficiency, while $E_{discharge}$ and E_{charge} are the battery discharge voltage and charge voltage, respectively.

Discharge polarization curves were obtained by discharging the battery from 0 mA to 400 mA at a scan rate of 1 mA s^{-1}. The power density of the battery was determined using the discharge polarization curve and the following equation.

$$P = J \cdot V \qquad (4-2)$$

where P, J, and V are the power density of the battery, the discharge current density, and the corresponding discharge voltage, respectively.

EIS was used to measure the resistance of the battery by applying a 10 mV AC potential from 100 kHz to 10 mHz at 1.2 V vs. Zn/Zn^{2+}. The EIS data was fitted to an equivalent circuit shown in Figure S4.1a using EC-Lab.

4.3. Results and Discussion

To investigate whether GPE-KOH synthesized using in-situ fabrication provides any electrochemical advantages over GPEs synthesized using ex-situ fabrication, rate tests, cyclability tests, and EIS analysis were done. As shown in Figure 4.2a and Figure 4.2b, GPE-KOH synthesized using in-situ and ex-situ fabrication exhibits similar charging behavior at different current densities. The discharge performance is also similar at lower current densities, although the battery with ex-situ fabricated GPE has slightly better discharge potentials. The difference in discharge performance increases with increasing current density, with the ex-situ fabricated GPE showing better overall battery efficiency and peak power density. Table 4.1 summarizes the battery efficiencies and peak power densities for ZABs using GPE-KOH synthesized with both methods. Figure 4.2c shows the Nyquist plots obtained using EIS and the equivalent circuit is shown in Figure S4.1a. Table 4.2 summarizes the R_s, R_{int}, and R_{ct} values obtained using the fitted impedance data. R_s is the resistance from the electrolyte plus other resistances due to wires and contacts[111]. R_{int} is particularly important in this study because it demonstrates the interfacial resistance between the electrolyte and the electrode[5]. The use of in-situ fabrication for the GPE was expected to lower the interfacial resistance between the electrolyte and electrode when

compared with GPEs synthesized using ex-situ fabrication[110]. R_{ct} represents the charge transfer resistance of the air electrode during electrochemical reactions[111]. As summarized in Table 4.2, the R_s values are similar for both electrolytes, but the R_{int} and R_{ct} values are larger for the in-situ fabricated GPE. The battery performance difference appears to be mainly caused by the charge transfer resistance of the air electrode. A larger R_{ct} value means worse ORR catalytic activity[111-113], which resulted in the lower discharge voltage and peak power density for the ZAB using in-situ fabrication of the GPE. The result was unexpected, as better contact between the GPE and the air electrode was expected with in-situ fabrication. This will be discussed later in this section.

Figure 4.2d to Figure 4.2f show GCD curves of cyclability tests for ZABs using GPE fabricated by the two methods, at 2 mA cm^{-2}, 5 mA cm^{-2}, and 10 mA cm^{-2}. Figure S4.1b to Figure S4.1d show the complete views of these tests. Table 4.3 summarizes the battery initial and final efficiencies for both synthesis methods at different current densities. ZABs using both GPE fabrication methods demonstrate competitive battery cyclability when compared with the literature shown in Table 3.7. The cycling behavior at 2 mA cm^{-2} is very similar for the two ZABs; however, the cycling behavior for ZABs using in-situ fabricated GPE is worse when cycled at 5 mA cm^{-2} and 10 mA cm^{-2}. For current densities of 5 mA cm^{-2} and 10 mA cm^{-2}, the initial charge and discharge potentials are similar to those attained during rate testing, with the ZABs fabricated with ex-situ GPEs exhibiting higher discharge potentials. As cycling proceeds, there is some degradation in the discharge potentials for both batteries, but the discharge potentials are about the same for both. The main difference is with the charging potentials. For both ZABs, the charging potentials increase initially during cycling and then level out; however, the increase in charging potential is larger for the ZAB with the in-situ fabricated GPE and the difference is larger at higher current density. The reasons that caused this phenomenon were explored and are explained later in this section.

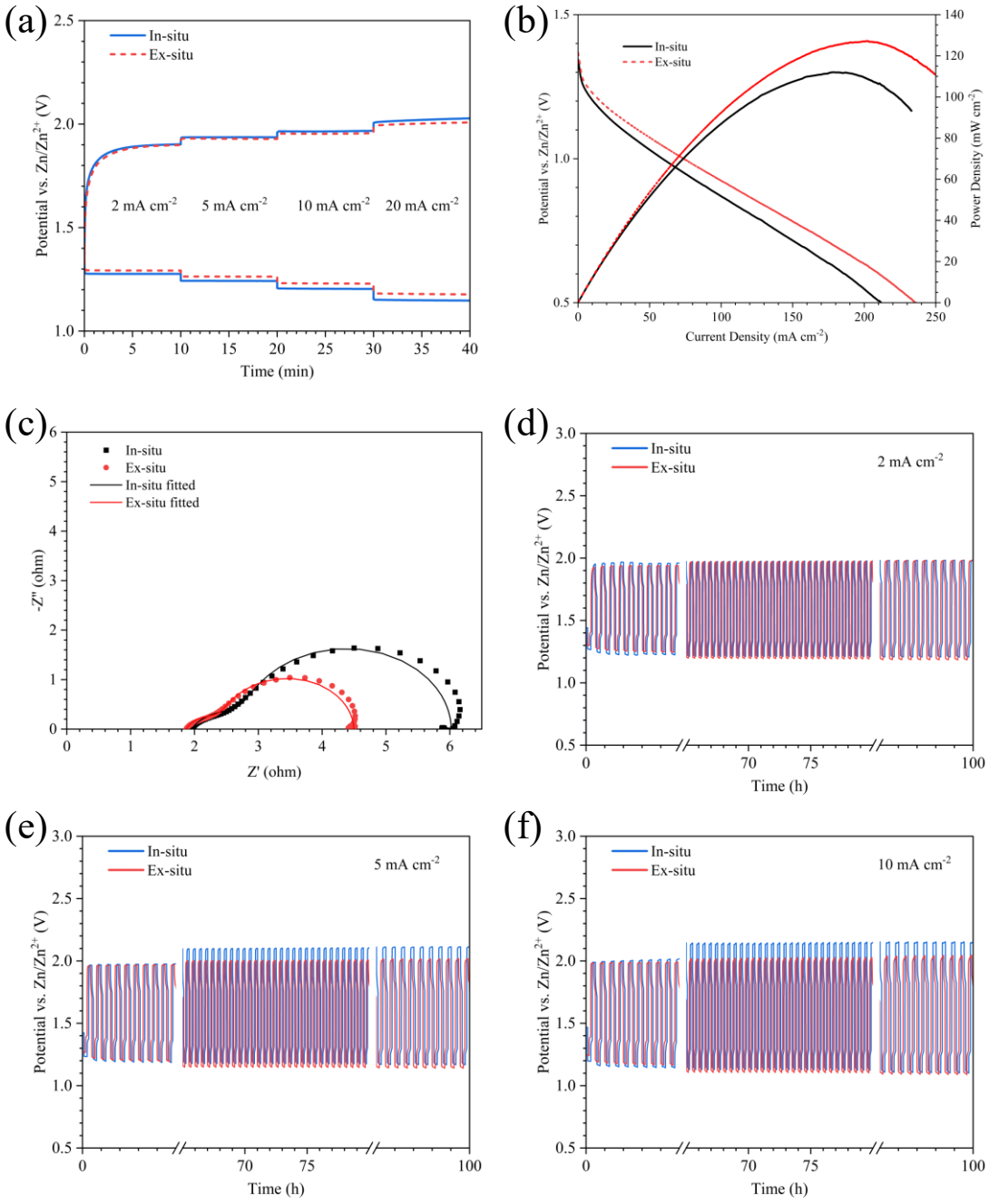

Figure 4.2. Electrochemical results for ZABs using GPE-KOH synthesized using in-situ and ex-situ fabrication. (a) Rate test, (b) discharge polarization curves and corresponding power densities, and (c) Nyquist plots. Experimental data is shown using symbols while the best fitted lines obtained using the equivalent circuit illustrated in Figure S4.1a are shown using solid lines. Cyclability test for ZABs using GPE-KOH synthesized using in-situ and ex-situ fabrication at (d) 2 mA cm^{-2}, (e) 5 mA cm^{-2}, and (f) 10 mA cm^{-2}.

Table 4.1. Rate test results comparison between ZABs using GPE-KOH synthesized by in-situ and ex-situ fabrication

	Efficiency at different current densities (%)				
Synthesis method	2 mA cm^{-2}	5 mA cm^{-2}	10 mA cm^{-2}	20 mA cm^{-2}	Peak power density (mW cm^{-2})
In-situ	67	64	61	56	112
Ex-situ	68	67	63	59	127

Table 4.2. Summary of values for equivalent circuit elements based on the fitted impedance data

GPE synthesis method	R_s (Ω)	R_{int} (Ω)	R_{ct} (Ω)
In-situ fabrication	1.95	0.923	3.14
Ex-situ fabrication	1.871	0.732	2.00

Table 4.3. Cyclability test results comparison for ZABs using GPE-KOH synthesized using in-situ and ex-situ fabrication

	2 mA cm^{-2}		5 mA cm^{-2}		10 mA cm^{-2}	
Synthesis method	Initial Efficiency (%)	Final Efficiency (%)	Initial Efficiency (%)	Final Efficiency (%)	Initial Efficiency (%)	Final Efficiency (%)
In-situ	65	61	63	55	60	51
Ex-situ	68	60	64	57	63	53

To compare the degree of GPE penetration into the GDL, the backing layer of the air electrodes used in the sandwich-type cell and the 3D-printed cell were examined using SEM and EDX analysis. A pristine, annealed air electrode sample was also examined as a baseline. Figure 4.3a shows the backing layer of the GDL coated with $(Co,Fe)_3O_4$ after annealing. The GDL

consists of two layers, a microporous layer which contains the catalyst and is in contact with the electrolyte during battery operation. The other layer is a macroporous layer which faces outward away from the electrolyte; it is highly hydrophobic and allows gas diffusion to and from the microporous layer. Both layers are composed of graphitized carbon fibers[5] which are bound together with polytetrafluoroethylene (PTFE)[115]. EDX spectra from the backing layer are shown in Figure 4.4a and Figure 4.4b. The spectra are, in fact, the same; the spectrum in Figure 4.4a is just an expanded view of the spectrum in Figure 4.4b at lower energies. Several elements, including C, O, F, Co, Fe, Na, Si, and S, are detected which correspond to the GDL (C, O, F, Si, and S), and the catalyst (Fe, Co, and O). The Na signal is from the solution utilized during catalyst impregnation. Figure 4.3b shows an SEM SE image of the backing layer of the GDL that was used with ex-situ fabricated GPE-KOH. A full sandwich-type cell was first assembled and left at room temperature and in ambient air for 1 h to allow the GPE-KOH to penetrate into the air electrode and then the cell was disassembled to obtain the air electrode sample. The morphology of the air electrode backside is similar to that of the pristine air electrode (Figure 4.3a). The EDX spectra, shown in Figure 4.4c and Figure 4.4d, has peaks for K and Zn, in addition to the peaks detected for the pristine air electrode sample (Figure 4.4a and 4.4b). The SEM SE image (Figure 4.3c) of the air electrode sample obtained from the 3D-printed cell, which was used for in-situ fabrication of the GPE, shows several white features on the backing layer of the GDL. The EDX spectrum, shown in Figure 4.4e and Figure 4.4f, has the same peaks detected in the ex-situ fabrication sample, with higher peak intensities for K and Zn. The K and Zn peaks for both the ex-situ and in-situ fabrication samples are attributed to GPE-KOH as only the electrolyte contains K and Zn. EDX maps for K and O (Figure 4.5) were taken from the same areas shown in Figure 4.3b (sandwich-type cell) and Figure 4.3c (3D-printed cell). The K and O signals overlap and the most intense signals correspond to the white features. These features indicate regions where the electrolyte has penetrated through the GDL and reached the back side (air side). Clearly, there is more electrolyte penetration for the 3D-printed cell (in-situ fabrication).

Electrolyte penetration may affect the catalytic activity of the air electrode. The catalyst distribution in the GDL microporous layer changes with depth; i.e., the concentration decreases with increasing depth into the microporous layer. In a recent study where the same catalyst impregnation process was used, the amount of catalyst decreased significantly at a depth of ~35 μm[116]. During battery discharging, ORR happens at three-phase boundaries where oxygen,

catalyst, and the electrolyte are in contact[115]. Figure 4.6 shows a schematic illustration of the expected or desired distribution of the GPE within the catalyst impregnated GDL from in-situ fabrication. There is a good distribution of three-phase boundaries with sufficient porosity remaining to allow for gas diffusion. The actual GPE distribution in the GDL is more like the situation depicted in Figure 4.6b, where there is complete penetration in places of the GPE through the GDL, including the microporous or backing layer. This leads to fewer three-phase boundaries and more blocked porosity. The result is fewer catalytic sites for ORR and fewer pores for gas diffusion. It becomes more difficult for oxygen to reach the areas where catalyst is available because the solubility of oxygen in the electrolyte is low[117]. As such, the higher charge transfer resistance and lower discharging voltages during rate testing, for the ZAB with the in-situ fabricated GPE, are attributed to over penetration of GPE through the GDL. Over penetration of GPE into the GDL is similar to aqueous electrolyte flooding, which may cause higher interfacial resistance[29].

O_2 is consumed during battery discharging at three-phase boundaries[115] and evolved from the air electrode during battery charging at two-phase boundaries where catalyst and electrolyte are both available[10]. When in-situ fabrication is used, more GPE penetrates through the GDL, reaching areas where catalyst is not available. OER can still occur at the catalyst/electrolyte interfaces, but porosity is blocked which hinders O_2 escape from the GDL and lead to O_2 accumulation. When the battery (with in-situ fabricated GPE) is cycled at lower current densities (e.g., 2 mA cm^{-2}), the reaction rate is low enough to allow O_2 to escape. However, at higher current densities (5 mA cm^{-2} and higher), O_2 escape cannot keep up with the faster rates so that discharge potentials are larger.

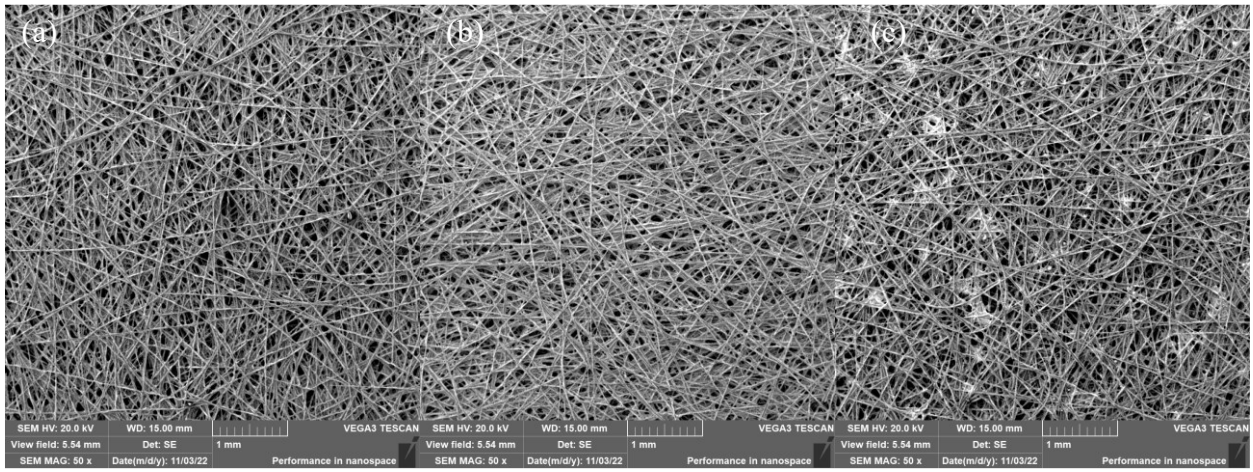

Figure 4.3. SEM SE images of the backing layer of the GDL coated with $(Co,Fe)_3O_4$ on the front side (a) after annealing (pristine sample), (b) after assembly and disassembly of the sandwich-type cell (ex-situ fabrication sample), and (c) after synthesizing the GPE using in-situ fabrication and disassembly of the 3D-printed cell (in-situ fabrication sample).

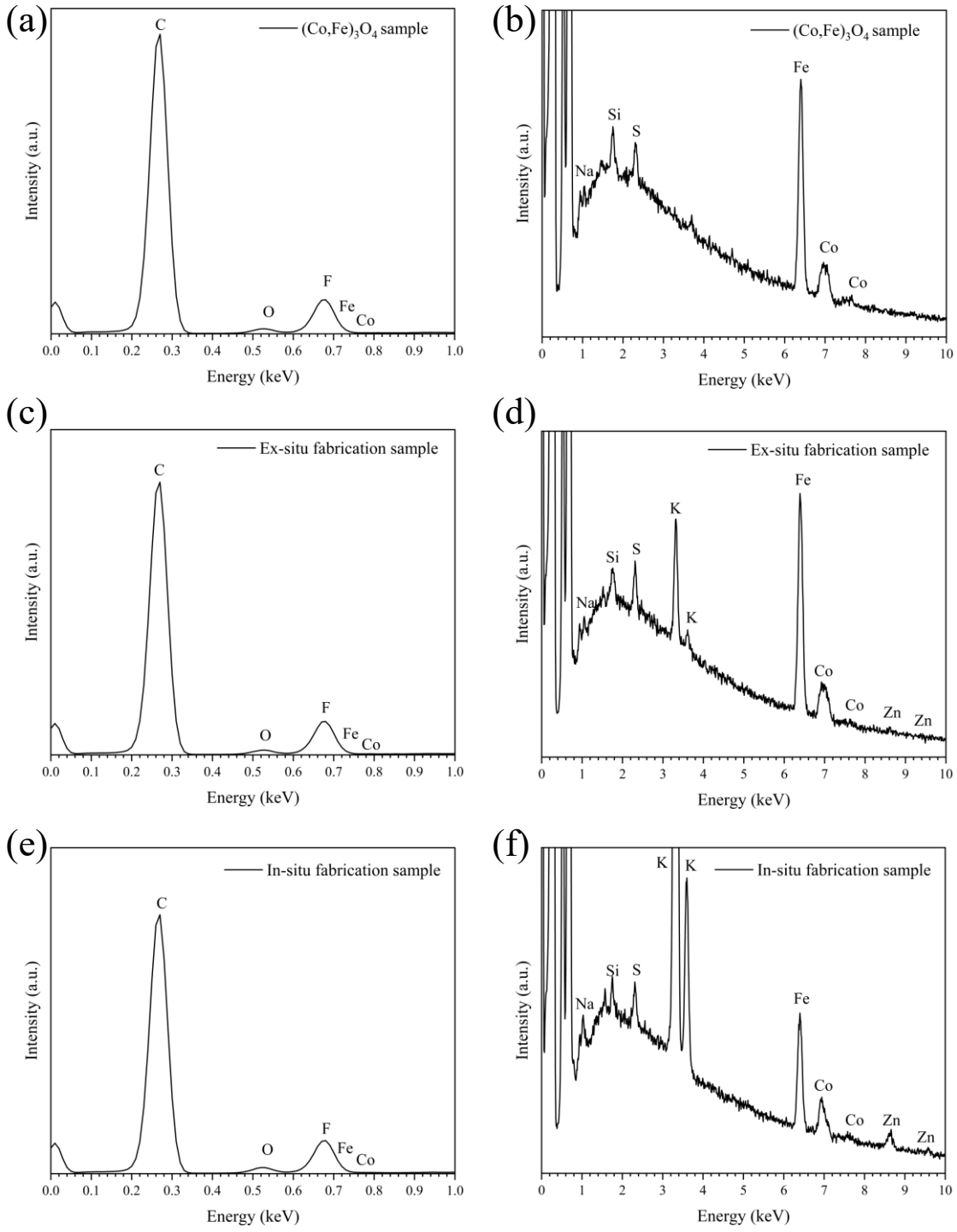

Figure 4.4. EDX spectra for (a-b) the $(Co,Fe)_3O_4$ air electrode sample, (c-d) the ex-situ fabrication sample, and (d-e) the in-situ fabrication sample, with (a), (c), and (e) showing an expanded view in the 0-1 keV range and (b), (d), and (f) showing the range from 0-10 keV. The spectra are from the entire area of the respective images in Figure 4.3.

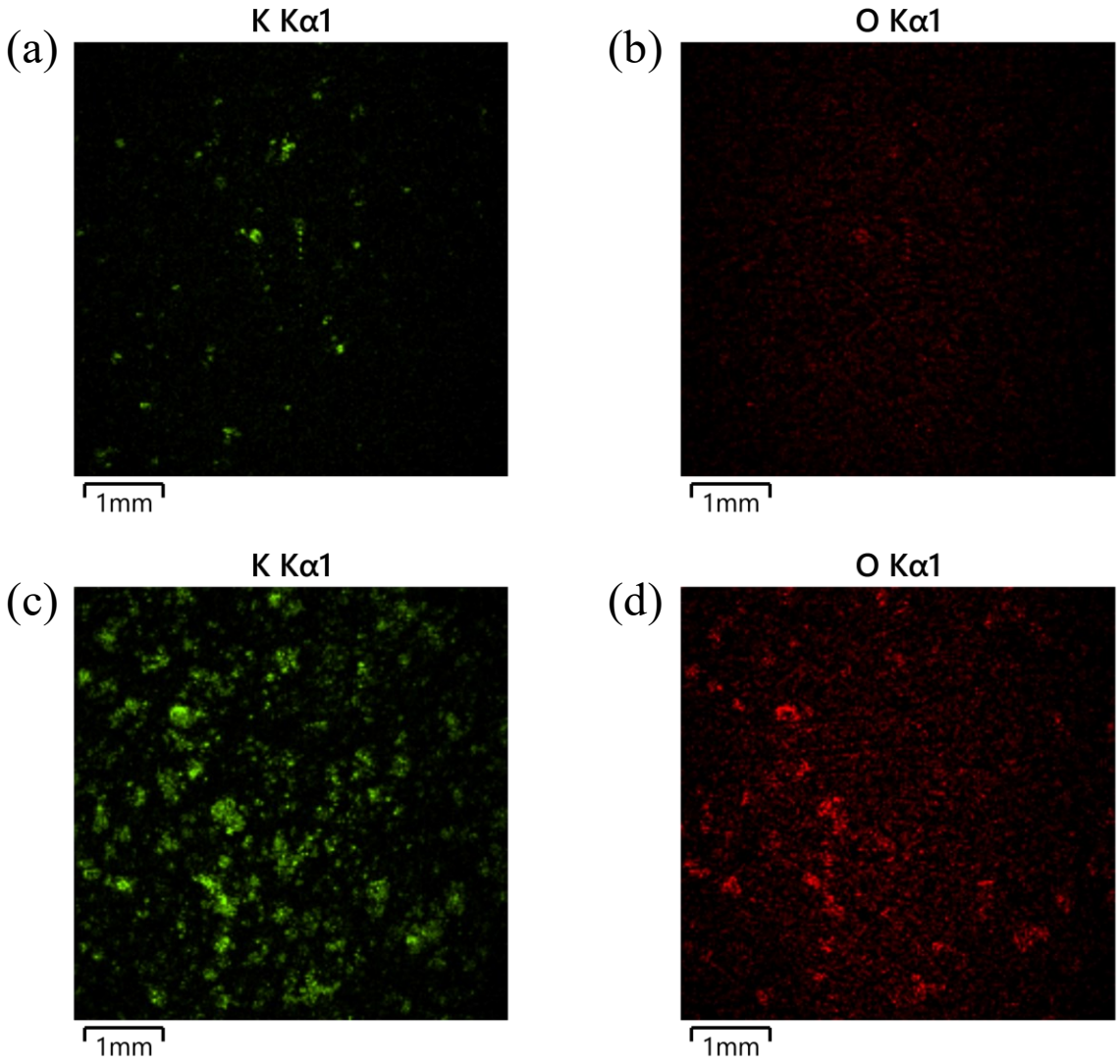

Figure 4.5. SEM EDX maps of K and O for (a-b) the ex-situ fabrication air electrode sample and (c-d) the in-situ fabrication air electrode sample for the images shown in Figure 4.3b and Figure 4.3c, respectively.

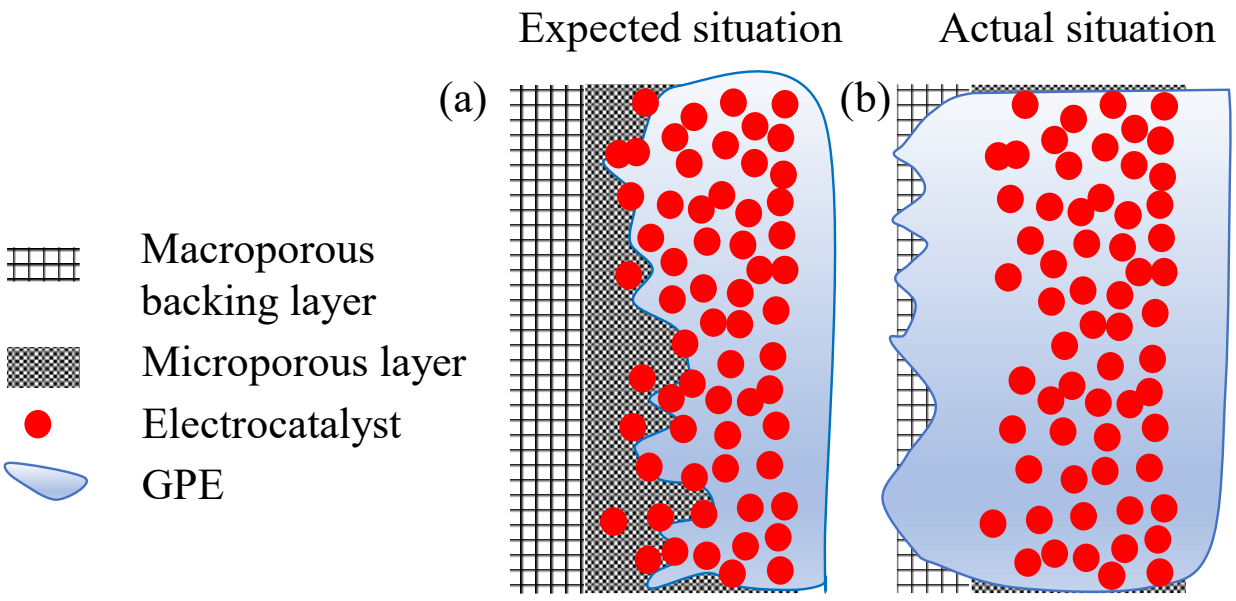

Figure 4.6. Schematic illustration of GPE penetration into the GDL using in-situ fabrication for the (a) expected situation and (b) actual situation.

4.4 Conclusions

In summary, a 3D-printed cell was designed to realize in-situ fabrication of a GPE in a ZAB. The use of in-situ GPE fabrication did not lead to reduced interfacial resistance between the electrolyte and the air electrode for the battery, nor did it improve battery cyclability.

SEM and EDX analysis revealed that more GPE completely penetrated through the air electrode, reaching areas where less catalyst was available causing electrolyte flooding. As a result, the three-phase reaction zone where the ORR takes place, as well as the two-phase reaction zone where the OER takes place, had less catalyst available in the cell fabricated in-situ compared with the cell fabricated ex-situ. This led to worse battery discharge performance during rate testing for the in-situ cell. Moreover, during battery cycling, the penetrating GPE blocked GDL pores, which hindered O_2 escape during battery charging, leading to O_2 accumulation in the GDL.

4.5. Supporting Information

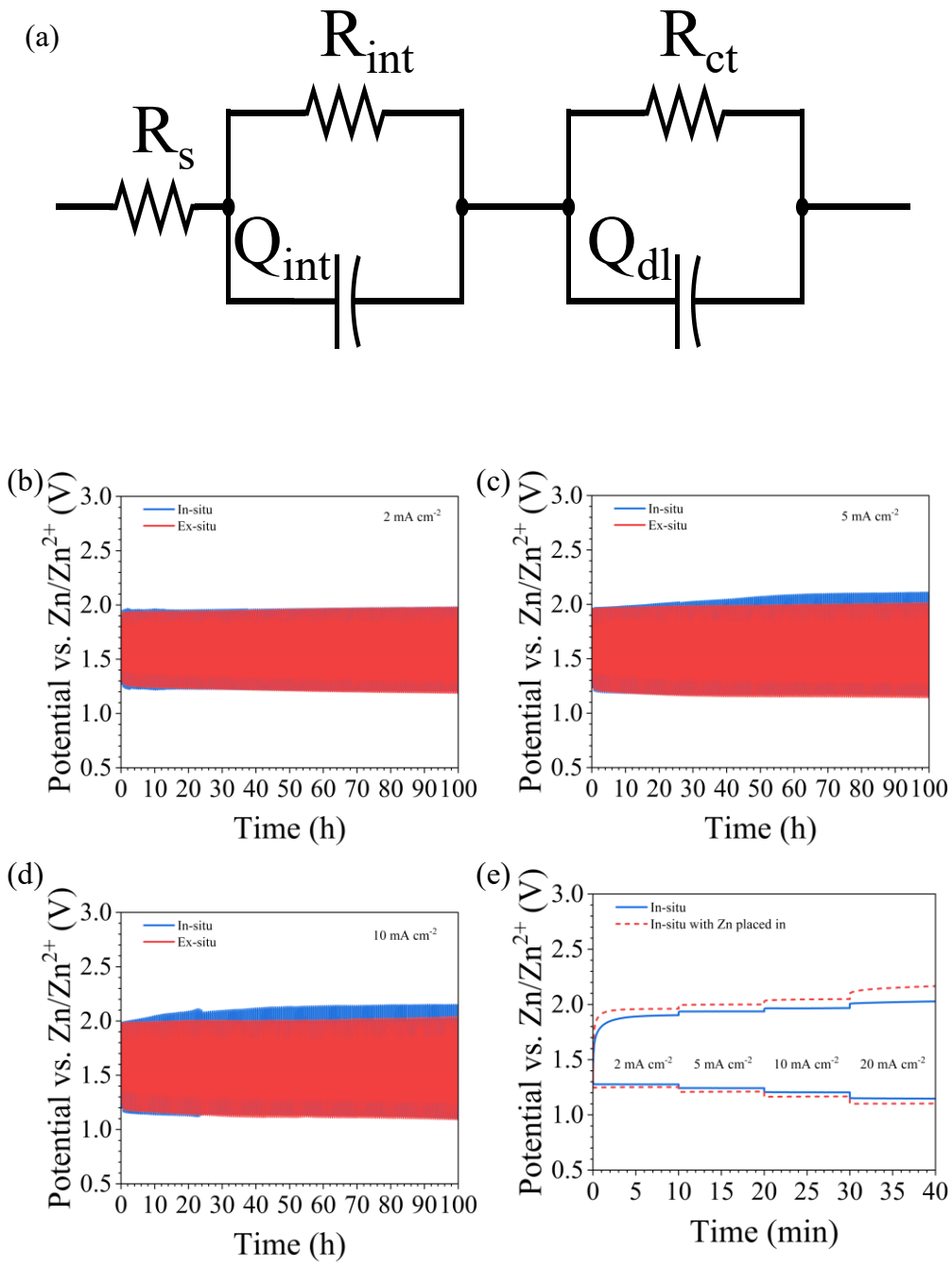

Figure S4.1. (a) Equivalent circuit used for EIS analysis. GCD curves for ZABs using GPE synthesized by the two methods cycled at (b) 2 mA cm^{-2}, (c) 5 mA cm^{-2}, and (d) 10 mA cm^{-2}. (e) ZAB rate tests using in-situ fabricated GPE-KOH with and without Zn placed in the 3D-printed cell during fabrication.

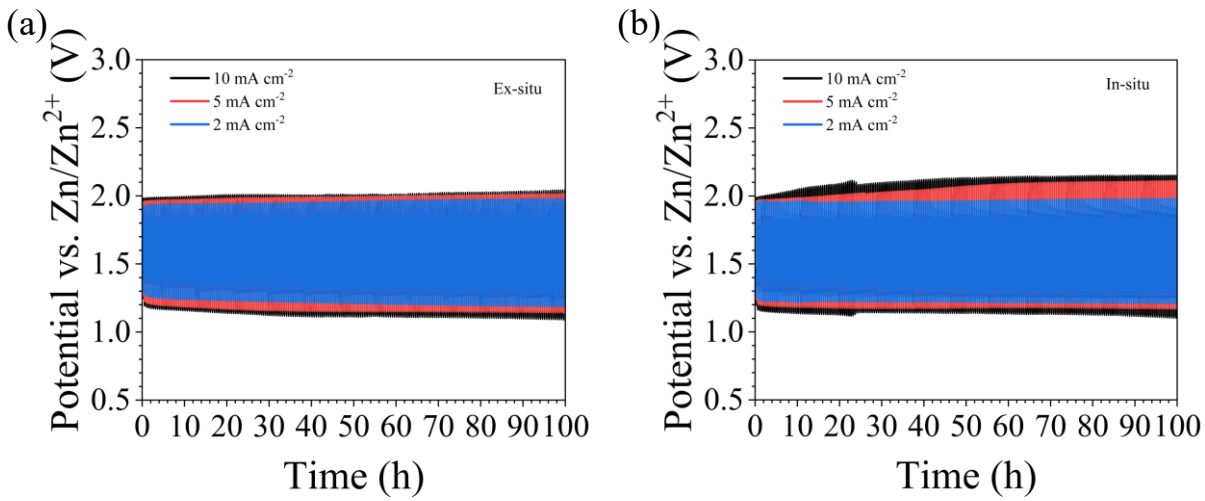

Figure S4.2. Cyclability tests at different current densities for ZABs using GPE synthesized using (a) ex-situ fabrication and (b) in-situ fabrication.

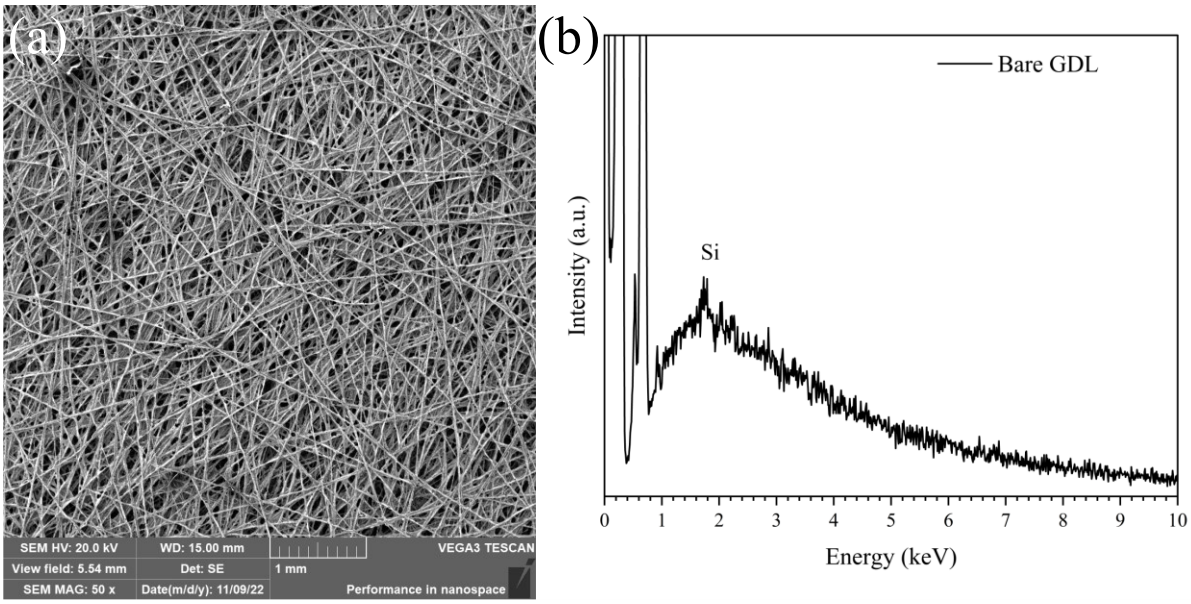

Figure S4.3. (a) SEM SE image of a bare GDL without catalyst coated and its (b) EDX spectrum.

Chapter 5. Conclusions and Future Work

5.1. Conclusions

The first part of this thesis investigated the low-temperature performance of Zn-air batteries (ZABs) using gel polymer electrolytes (GPEs) with and without KI as an additive to the GPE. Both GPEs exhibited excellent low-temperature resistance and ZABs utilizing these two GPEs outperformed other competitors reported in the literature. The second part of the thesis examined the use of in-situ fabrication of the GPD to reduce the interfacial resistance between the GPE and the electrode. The following subsections summarize the achievements of these studies.

5.1.1. Gel Polymer Electrolytes for Zn-air Batteries Operating at Low Temperatures

An electrolyte consisting of a gel polymer and KOH (GPE-KOH) was developed based on previous work done in the author's group. Changes in relative humidity in the laboratory affected battery cyclability. ZABs using GPE-KOH were able to cycle at 10 mA cm^{-2} and $-25℃$ for 100 h (200 cycles) with initial and final efficiencies of 50% and 41%, respectively. A lifetime test was done for a ZAB with GPE-KOH at 10 mA cm^{-2} and 21℃ with a relative humidity of 85%. The ZAB was successfully cycled for 260 h (520 cycles) before experiencing accelerated performance degradation. The initial efficiency was 61% and the efficiency at 260 h was 42%.

A second electrolyte (GPE-KOH-KI) was synthesized in a procedure similar to that for GPE-KOH but with an additional immersion step. The addition of KI to the electrolyte changed the conventional OER to an oxidation reaction of I^-, which has a lower thermodynamic barrier, resulting in a much lower charging voltage and better battery efficiency when compared with ZABs using GPE-KOH. The efficiency of ZABs was greatly improved with an initial efficiency of 71% when cycled at 10 mA cm^{-2} and 21℃. However, the cyclability of ZABs at 10 mA cm^{-2} using GPE-KOH-KI was not as good as the ZAB using GPE-KOH. A full cell reaction was proposed, where the reaction at the Zn electrode is considered to be reversible while the reaction at the air electrode is not, resulting in an accumulation of KIO_3 as the battery cycles.

5.1.2. In-Situ Fabrication of Gel Polymer Electrolytes for Zn-Air Batteries

A cell configuration for in-situ fabrication of GPE for ZABs without leakage was developed, which can also be used for ZABs with aqueous electrolytes. The interfacial resistance

was not reduced and the cyclability of the battery was not improved by using in-situ fabrication. ZABs using in-situ fabricated GPE-KOH exhibited worse battery discharge performance during rate testing and worse charging performance during cyclability testing, with larger efficiency differences at higher current densities. SEM and EDX analysis revealed that more GPE completely penetrated through the air electrode during in-situ fabrication compared with ex-situ fabrication, resulting in an increase in charge transfer resistance that led and reduced catalytic activity, electrolyte flooding, and blockage of GDL pores. The poorer charging performance during cycle testing was attributed to O_2 accumulation in the GDL pores due to the poor blockage by the GPE.

5.2. Future Work

The following recommendations are made for future work in this research area.

5.2.1. Battery Failure Analysis

A ZAB using GPE-KOH was able to withstand 520 cycles at 21℃ and 10 mA cm^{-2} before experiencing accelerated discharge performance degradation and the battery eventually failed at 270 h. The exact reason(s) for battery failure are not clear and need to be determined. Post-cycling battery failure analysis needs to be done by disassembling the battery and examining the battery components; i.e., the GPE, the Zn electrode, and the air electrode, using microstructural techniques such as electron microscopy and X-ray diffraction. In addition, the cycled components can be assembled with other fresh components (e.g., tested GPE with fresh Zn and air electrodes) and cycled again. The component responsible for cell failure in the lifetime tests will exhibit faster performance degradation or even instant cell failure in the new cyclability tests.

5.2.2. Determination of Reaction Mechanisms

With the addition of KI to the electrolyte, the battery efficiency was improved significantly. However, with the change in charging reaction from the conventional OER to an oxidization reaction of I^-, the discharging reaction of the battery became uncertain. It is important to determine whether the product (IO_3^-) formed during charging is converted back to the reactant (I^-) during discharging, since the conversion reaction is required for a reversible air electrode and a fully rechargeable battery. Ultraviolet–visible (UV-vis) spectroscopy and ion chromatography (IC) were methods used previously by other researchers for the detection of IO_3^-, and these techniques were utilized in this study. The concentration of IO_3^- cannot be determined directly from UV-vis

testing as no peak appears for IO_3^-. However, I^- exhibits a clear peak in the UV-vis spectrum. Therefore, the concentration of IO_3^- can be determined indirectly from the UV-vis results, by measuring the pH of the solution to determine the concentration of OH^-. The concentration of IO_3^- can then be calculated based on the free energy change for the air anode reaction (Figure 3.8b).

5.2.3. Investigation of Catalysts

Pt/RuO_2 was used as the catalyst to achieve better battery cyclability in ZABs using KI as an additive to the GPE-KOH electrolyte in this study. $(Co,Fe)_3O_4$, which is cheaper than Pt/RuO_2 was utilized as the catalyst for ZABs with GPE-KOH. $(Co,Fe)_3O_4$ was not an effective catalyst for charging reaction in batteries with GPE-KOH-KI electrolytes. Further investigation is needed to develop more cost-effective catalysts for ZABs with GPE-KOH-KI electrolytes. Zhao et.al have claimed that Pt can catalyze both the oxidation of I^- as well as the ORR[85]. Therefore, it is worth trying Pt alone as the catalyst for ZABs with GPE-KOH-KI as a first step to lowering the cost of catalyst.

5.2.4. Further investigation of Air Electrodes

GDLs substrates impregnated with $(Co,Fe)_3O_4$ decorated N-CNTs were used as the air electrodes with in-situ fabrication of GPE. However, the electrolyte completely penetrated through the air electrode in several regions, leading to poorer catalytic activity and poorer battery cyclability when cycled at a 5 mA cm^{-2} and 10 mA cm^{-2}. In-situ fabrication was developed in an attempt to lower the interfacial resistance between the air electrode and the electrolyte; however, the interfacial resistance increased, in part because of electrolyte flooding and blockage of GDL pores. Further microstructural analysis is needed to characterize the electrolyte distribution within the GDL, both within the microporous layer and the backing layer. This can be done through electron microscopy methods using focused ion beam (FIB) techniques for cross section specimen preparation.

References

1. Wuebbles, D. J. & Jain, A. K. Concerns about climate change and the role of fossil fuel use. *Fuel Process. Technol.* **71**, 99–119 (2001).

2. Owusu, P. A. & Asumadu-Sarkodie, S. A review of renewable energy sources, sustainability issues and climate change mitigation. *Cogent Engineering* vol. 3 (2016).

3. Denholm, P., Ela, E., Kirby, B. & Milligan, M. The role of energy storage with renewable electricity generation. in *Energy Storage: Issues and Applications* 1–58 (2011).

4. Caramia, V. & Bozzini, B. Materials science aspects of zinc-air batteries: A review. *Mater. Renew. Sustain. Energy* **3**, (2014).

5. Fu, J. *et al.* Electrically Rechargeable Zinc–Air Batteries: Progress, Challenges, and Perspectives. *Advanced Materials* vol. 29 (2017).

6. James Morris. Rising Lithium Prices Could Stop The EV Revolution – Or Could They? *Forbes* https://www.forbes.com/sites/jamesmorris/2022/04/16/rising-lithium-prices-could-stop-the-ev-revolution--or-could-they/?sh=accc01171255 (2022).

7. Fu, J. *et al.* Recent Progress in Electrically Rechargeable Zinc–Air Batteries. *Advanced Materials* vol. 31 (2019).

8. Tran, T. N. T. *et al.* Compositional Effects of Gel Polymer Electrolyte and Battery Design for Zinc-Air Batteries. *Batter. Supercaps* **3**, 917–927 (2020).

9. Solar 101 - Solar Alberta. https://solaralberta.ca/learn/solar-101/.

10. Tran, T. N. T., Clark, M. P., Xiong, M., Chung, H. J. & Ivey, D. G. A tri-electrode configuration for zinc-air batteries using gel polymer electrolytes. *Electrochim. Acta* **357**, (2020).

11. Lee, J. S. *et al.* Metal-air batteries with high energy density: Li-air versus Zn-air. *Advanced Energy Materials* vol. 1 34–50 (2011).

12. Diggle, J. W., Despic, A. R. & Bockris, J. O. The Mechanism of the Dendritic

Electrocrystallization of Zinc. *J. Electrochem. Soc.* **116**, 1503 (1969).

13. Moshtev, R. V & Zlatilova, P. Kinetics of growth of zinc dendrite precursors in zincate solutions. *J. Appl. Electrochem.* **8**, 213–222 (1978).

14. Aasen, D., Clark, M. P. & Ivey, D. G. Investigation of Transition Metal-Based (Mn, Co, Ni, Fe) Trimetallic Oxide Nanoparticles on N-doped Carbon Nanotubes as Bifunctional Catalysts for Zn-Air Batteries. *J. Electrochem. Soc.* **167**, 040503 (2020).

15. Mainar, A. R. *et al.* An overview of progress in electrolytes for secondary zinc-air batteries and other storage systems based on zinc. *Journal of Energy Storage* vol. 15 304–328 (2018).

16. Wang, C. *et al.* Rechargeable zinc-air batteries with neutral electrolytes: Recent advances, challenges, and prospects. *EnergyChem* vol. 3 (2021).

17. Li, L. & Manthiram, A. Long-Life, High-Voltage Acidic Zn-Air Batteries. *Adv. Energy Mater.* **6**, (2016).

18. Hosseini, S., Masoudi Soltani, S. & Li, Y. Y. Current status and technical challenges of electrolytes in zinc–air batteries: An in-depth review. *Chemical Engineering Journal* vol. 408 (2021).

19. Fernicola, A., Scrosati, B. & Ohno, H. Potentialities of ionic liquids as new electrolyte media in advanced electrochemical devices. *Ionics* vol. 12 95–102 (2006).

20. Zhu, M. *et al.* Antifreezing Hydrogel with High Zinc Reversibility for Flexible and Durable Aqueous Batteries by Cooperative Hydrated Cations. *Adv. Funct. Mater.* **30**, (2020).

21. Mohamad, A. A. Zn/gelled 6 M KOH/O2 zinc-air battery. *J. Power Sources* **159**, 752–757 (2006).

22. Lan, Z., Wu, J., Lin, J. & Huang, M. Quasi-solid-state dye-sensitized solar cells with a novel efficient absorbent for liquid electrolyte based on PAA-PEG hybrid. *J. Power Sources* **164**, 921–925 (2007).

23. Wei, Y., Shi, Y., Chen, Y., Xiao, C. & Ding, S. Development of solid electrolytes in Zn-air and Al-air batteries: From material selection to performance improvement strategies.

Journal of Materials Chemistry A vol. 9 4415–4453 (2021).

24. Sui, X. *et al.* Zwitterionic Osmolyte-Based Hydrogels with Antifreezing Property, High Conductivity, and Stable Flexibility at Subzero Temperature. *Adv. Funct. Mater.* **30**, (2020).

25. Zhou, D. *et al.* Biomimetic Extreme-Temperature- and Environment-Adaptable Hydrogels. *ChemPhysChem* vol. 20 2139–2154 (2019).

26. Chen, R. *et al.* A Flexible and Safe Aqueous Zinc-Air Battery with a Wide Operating Temperature Range from -20 to 70 °C. *ACS Sustain. Chem. Eng.* **8**, 11501–11511 (2020).

27. Villars, P. H-K-O Vertical Section of Ternary Phase Diagram. *SpringerMaterials (online database)* c_0212343 https://materials.springer.com/isp/phase-diagram/docs/c_0212343 (2016).

28. Pei, Z. *et al.* A Flexible Rechargeable Zinc–Air Battery with Excellent Low-Temperature Adaptability. *Angew. Chemie - Int. Ed.* **59**, 4793–4799 (2020).

29. Tran, T. N. T., Chung, H. J. & Ivey, D. G. A study of alkaline gel polymer electrolytes for rechargeable zinc–air batteries. *Electrochim. Acta* **327**, (2019).

30. Tran, T. N. T., Clark, M. P., Chung, H. J. & Ivey, D. G. Effects of Crosslinker Concentration in Poly(Acrylic Acid)-KOH Gel Electrolyte on Performance of Zinc-Air Batteries. *Batter. Supercaps* **3**, 409–416 (2020).

31. Choudhary, Y. S., Jothi, L. & Nageswaran, G. Electrochemical Characterization. in *Spectroscopic Methods for Nanomaterials Characterization* vol. 2 19–54 (Elsevier, 2017).

32. Yang, X. & Rogach, A. L. Electrochemical Techniques in Battery Research: A Tutorial for Nonelectrochemists. *Advanced Energy Materials* vol. 9 (2019).

33. Bard, Allen J., L. R. F. *Electrochemical methods: fundamentals and applications*. (John Wiley & Sons, 2001).

34. Parker, V. D. Chapter 3 Linear Sweep and Cyclic Voltammetry. *Compr. Chem. Kinet.* **26**, 145–202 (1986).

35. Elgrishi, N. *et al.* A Practical Beginner's Guide to Cyclic Voltammetry. *J. Chem. Educ.* **95**, 197–206 (2018).

36. Wang, J. *Analytical electrochemistry*. (John Wiley & Sons, 2006).

37. Díaz-Patiño, L. *et al.* Zinc-Air Battery Operated with Modified-Zinc Electrodes/Gel Polymer Electrolytes. *ChemElectroChem* **9**, (2022).

38. Bredar, A. R. C., Chown, A. L., Burton, A. R. & Farnum, B. H. Electrochemical Impedance Spectroscopy of Metal Oxide Electrodes for Energy Applications. *ACS Applied Energy Materials* vol. 3 66–98 (2020).

39. Tran, T. N. T. Gel Polymer Electrolytes and Battery Designs for Rechargeable Zinc-Air Batteries. (University of Alberta, 2020).

40. Goldstein, J. I. *et al. Scanning Electron Microscopy and X- Ray Microanalysis*. (Springer, 2017).

41. Dobraszczyk, B. J. & Morgenstern, M. P. Rheology and the breadmaking process. *Journal of Cereal Science* vol. 38 229–245 (2003).

42. Liew, C. W., Durairaj, R. & Ramesh, S. Rheological studies of PMMA-PVC based polymer blend electrolytes with LiTFSI as doping salt. *PLoS One* **9**, (2014).

43. Wilson, D. I. What is rheology? *Eye* **32**, 179–183 (2018).

44. Schick, C. Differential scanning calorimetry (DSC) of semicrystalline polymers. *Analytical and Bioanalytical Chemistry* vol. 395 1589–1611 (2009).

45. Abraham, J., Mohammed, A. P., Kumar, M. P. A., George, S. C. & Thomas, S. Thermoanalytical techniques of nanomaterials. in *Characterization of Nanomaterials: Advances and Key Technologies* 213–236 (Elsevier, 2018).

46. Lukas, K. & LeMaire, P. K. Differential Scanning Calorimetry: Fundamental overview. *Resonance* **14**, 807–817 (2009).

47. Menczel, J. D. & Prime, R. B. *Thermal Analysis of Polymers: Fundamentals and*

Applications. *Thermal Analysis of Polymers: Fundamentals and Applications* (2008).

48. Zhang, Y. *et al.* Reaction modifier system enable double-network hydrogel electrolyte for flexible zinc-air batteries with tolerance to extreme cold conditions. *Energy Storage Mater.* **42**, 88–96 (2021).

49. Chapter 1 Introduction. in *ion chromatography* (eds. Haddad, P. R. & Haddad, P. R.) vol. 46 1–12 (Elsevier, 1990).

50. LEMMON, J. P. ION CHROMATOGRAPHY. Encyclopedia of Materials: Science and Technology. *Ion Chromatogr.* 1–4 (2001).

51. Chapter 9 Conductivity Detection. in *ion chromatography* (eds. Haddad, P. R. & Haddad, P. R. B. T.-J. of C. L.) vol. 46 245–289 (Elsevier, 1990).

52. Rocha, F. S., Gomes, A. J., Lunardi, C. N., Kaliaguine, S. & Patience, G. S. Experimental methods in chemical engineering: Ultraviolet visible spectroscopy—UV-Vis. *Can. J. Chem. Eng.* **96**, 2512–2517 (2018).

53. Worsfold, P. J. SPECTROPHOTOMETRY | Overview. in *Encyclopedia of Analytical Science* (eds. Worsfold, P., Townshend, A. & Poole, C. B. T.-E. of A. S. (Second E.) 318–321 (Elsevier, 2005). doi:https://doi.org/10.1016/B0-12-369397-7/00714-7.

54. Houghton, J. The science of global warming. *Clim. Chang.* **0188**, 3–13 (2017).

55. Johnsson, F., Kjärstad, J. & Rootzén, J. The threat to climate change mitigation posed by the abundance of fossil fuels. *Clim. Policy* **19**, 258–274 (2019).

56. Sims, R. E. H. Renewable energy: A response to climate change. *Sol. Energy* **76**, 9–17 (2004).

57. Solaun, K. & Cerdá, E. Climate change impacts on renewable energy generation. A review of quantitative projections. *Renew. Sustain. Energy Rev.* **116**, (2019).

58. Ravestein, P., van der Schrier, G., Haarsma, R., Scheele, R. & van den Broek, M. Vulnerability of European intermittent renewable energy supply to climate change and climate variability. *Renew. Sustain. Energy Rev.* **97**, 497–508 (2018).

59. Gernaat, D. E. H. J. *et al.* Climate change impacts on renewable energy supply. *Nat. Clim. Chang.* **11**, 119–125 (2021).

60. Zhang, J., Zhou, Q., Tang, Y., Zhang, L. & Li, Y. Zinc-air batteries: Are they ready for prime time? *Chem. Sci.* **10**, 8924–8929 (2019).

61. Li, Y. *et al.* Advanced zinc-air batteries based on high-performance hybrid electrocatalysts. *Nat. Commun.* **4**, 1–7 (2013).

62. Liu, X. *et al.* Mapping the Design of Electrolyte Materials for Electrically Rechargeable Zinc–Air Batteries. *Adv. Mater.* **33**, 1–21 (2021).

63. Luo, M., Sun, W., Xu, B. Bin, Pan, H. & Jiang, Y. Interface Engineering of Air Electrocatalysts for Rechargeable Zinc–Air Batteries. *Adv. Energy Mater.* **11**, 1–14 (2021).

64. Fan, X. *et al.* Porous nanocomposite gel polymer electrolyte with high ionic conductivity and superior electrolyte retention capability for long-cycle-life flexible zinc–air batteries. *Nano Energy* **56**, 454–462 (2019).

65. Fu, J. *et al.* A flexible solid-state electrolyte for wide-scale integration of rechargeable zinc-air batteries. *Energy Environ. Sci.* **9**, 663–670 (2016).

66. Park, J., Park, M., Nam, G., Lee, J. S. & Cho, J. All-solid-state cable-type flexible zinc-air battery. *Adv. Mater.* **27**, 1396–1401 (2015).

67. Li, M. *et al.* Long-Shelf-Life Polymer Electrolyte Based on Tetraethylammonium Hydroxide for Flexible Zinc-Air Batteries. *ACS Appl. Mater. Interfaces* **11**, 28909–28917 (2019).

68. Zhao, N. *et al.* Flexible Hydrogel Electrolyte with Superior Mechanical Properties Based on Poly(vinyl alcohol) and Bacterial Cellulose for the Solid-State Zinc-Air Batteries. *ACS Appl. Mater. Interfaces* **11**, 15537–15542 (2019).

69. Fu, J. *et al.* Flexible High-Energy Polymer-Electrolyte-Based Rechargeable Zinc-Air Batteries. *Adv. Mater.* **27**, 5617–5622 (2015).

70. Sun, N. *et al.* Alkaline Double-Network Hydrogels with High Conductivities, Superior

Mechanical Performances, and Antifreezing Properties for Solid-State Zinc-Air Batteries. *ACS Appl. Mater. Interfaces* **12**, 11778–11788 (2020).

71. Zhang, S. S., Xu, K. & Jow, T. R. The low temperature performance of Li-ion batteries. *J. Power Sources* **115**, 137–140 (2003).

72. Liu, D., Tong, Y., Yan, X., Liang, J. & Dou, S. X. Recent Advances in Carbon-Based Bifunctional Oxygen Catalysts for Zinc-Air Batteries. *Batteries and Supercaps* vol. 2 743–765 (2019).

73. Zhong, Y., Xu, X., Wang, W. & Shao, Z. Recent Advances in Metal-Organic Framework Derivatives as Oxygen Catalysts for Zinc-Air Batteries. *Batteries and Supercaps* vol. 2 272–289 (2019).

74. Luo, F. *et al.* Regulated coordination environment of Ni single atom catalyst toward high-efficiency oxygen electrocatalysis for rechargeable Zinc-air batteries. *Energy Storage Mater.* **35**, 723–730 (2021).

75. Song, Z. *et al.* A Rechargeable Zn–Air Battery with High Energy Efficiency and Long Life Enabled by a Highly Water-Retentive Gel Electrolyte with Reaction Modifier. *Adv. Mater.* **32**, 1–10 (2020).

76. Aasen, D., Clark, M. P. & Ivey, D. G. (Co,Fe)3O4 Decorated Nitrogen-Doped Carbon Nanotubes in Nano-Composite Gas Diffusion Layers as Highly Stable Bifunctional Catalysts for Rechargeable Zinc-Air Batteries. *Batter. Supercaps* **3**, 174–184 (2020).

77. Frank, M. Superabsorbents. in *Ullmann's Encyclopedia of Industrial Chemistry* (2003). doi:https://doi.org/10.1002/14356007.f25_f01.

78. Herth, G., Schornick, G. & L. Buchholz, F. Polyacrylamides and Poly(Acrylic Acids). in *Ullmann's Encyclopedia of Industrial Chemistry* 1–16 (2015). doi:https://doi.org/10.1002/14356007.a21_143.pub2.

79. Anjum, N., Joyal, N., Iroegbu, J., Li, D. & Shen, C. Humidity-modulated properties of hydrogel polymer electrolytes for flexible supercapacitors. *J. Power Sources* **499**, 229962 (2021).

80. Sun, Y., Liu, B., Liu, L. & Yan, X. Ions Transport in Electrochemical Energy Storage Devices at Low Temperatures. *Adv. Funct. Mater.* **32**, 1–26 (2022).

81. Meng, F., Xiong, X., Tan, L., Yuan, B. & Hu, R. Strategies for improving electrochemical reaction kinetics of cathode materials for subzero-temperature Li-ion batteries: A review. *Energy Storage Mater.* **44**, 390–407 (2022).

82. Ma, S. *et al.* Temperature effect and thermal impact in lithium-ion batteries: A review. *Prog. Nat. Sci. Mater. Int.* **28**, 653–666 (2018).

83. Zhang, J., Wang, J., Shi, Z. & Xu, Z. Electrochemical behavior of lithium ion capacitor under low temperature. *J. Electroanal. Chem.* **817**, 195–201 (2018).

84. Tang, Y. *et al.* Energy-saving synthesis of potassium iodate via electrolysis of potassium iodine and O2 in a membraneless cell. *Green Chem.* **14**, 334–337 (2012).

85. Zhao, S. *et al.* Pt/C as a bifunctional ORR/iodide oxidation reaction (IOR) catalyst for Zn-air batteries with unprecedentedly high energy efficiency of 76.5%. *Appl. Catal. B Environ.* **320**, 121992 (2023).

86. Hasebe, K. & Asahi, T. Inorganic Substances other than Oxides. Part 1: SbSI family ... TAAP · 32A-1 KIO3[F]. doi:10.1007/10635019_73.

87. Miseki, Y., Fujiyoshi, S., Gunji, T. & Sayama, K. Photocatalytic water splitting under visible light utilizing I 3-/I- and IO3-/I - redox mediators by Z-scheme system using surface treated PtO x/WO3 as O2 evolution photocatalyst. *Catal. Sci. Technol.* **3**, 1750–1756 (2013).

88. Higashi, M., Abe, R., Takata, T. & Domen, K. Photocatalytic overall water splitting under visible light using ATaO 2N (A = Ca, Sr, Ba) and WO 3 in a IO 3-/I - shuttle redox mediated system. *Chem. Mater.* **21**, 1543–1549 (2009).

89. Zhang, G. *et al.* Design of co-continuous structure of cellulose/PAA-based alkaline solid polyelectrolyte for flexible zinc-air battery. *Int. J. Biol. Macromol.* **221**, 446–455 (2022).

90. Miao, H. *et al.* All-solid-state flexible zinc-air battery with polyacrylamide alkaline gel electrolyte. *J. Power Sources* **450**, 227653 (2020).

91. Fan, X. *et al.* Porous nanocomposite gel polymer electrolyte with high ionic conductivity and superior electrolyte retention capability for long-cycle-life flexible zinc–air batteries. *Nano Energy* **56**, 454–462 (2019).

92. Zhang, Y. *et al.* Alkaline sodium polyacrylate-starch hydrogels with tolerance to cold conditions for stretchable zinc-air batteries. *Compos. Part B Eng.* **224**, 109228 (2021).

93. Pei, Z. *et al.* Make it stereoscopic: Interfacial design for full-temperature adaptive flexible zinc-air batteries. *Energy Environ. Sci.* **14**, 4926–4935 (2021).

94. Huang, Y. *et al.* Solid-State Rechargeable Zn//NiCo and Zn–Air Batteries with Ultralong Lifetime and High Capacity: The Role of a Sodium Polyacrylate Hydrogel Electrolyte. *Adv. Energy Mater.* **8**, 1802288 (2018).

95. Ma, L. *et al.* Super-Stretchable Zinc–Air Batteries Based on an Alkaline-Tolerant Dual-Network Hydrogel Electrolyte. *Adv. Energy Mater.* **9**, 1803046 (2019).

96. Wang, M., Xu, N., Fu, J., Liu, Y. & Qiao, J. High-performance binary cross-linked alkaline anion polymer electrolyte membranes for all-solid-state supercapacitors and flexible rechargeable zinc-air batteries. *J. Mater. Chem. A* **7**, 11257–11264 (2019).

97. Li, Y. *et al.* Long-battery-life flexible zinc-air battery with near-neutral polymer electrolyte and nanoporous integrated air electrode. *J. Mater. Chem. A* **7**, 25449–25457 (2019).

98. Lin, C. *et al.* Solid-State Rechargeable Zinc–Air Battery with Long Shelf Life Based on Nanoengineered Polymer Electrolyte. *ChemSusChem* **11**, 3215–3224 (2018).

99. Chen, Z. *et al.* Nanofiber Composite for Improved Water Retention and Dendrites Suppression in Flexible Zinc-Air Batteries. *Small* **17**, 1–7 (2021).

100. *CRC handbook of chemistry and physics.* (CRC Press, 1978).

101. Kholodovych, V. & Welsh, W. J. Densities of Amorphous and Crystalline Polymers BT - Physical Properties of Polymers Handbook. in (ed. Mark, J. E.) 611–617 (Springer New York, 2007). doi:10.1007/978-0-387-69002-5_37.

102. Varcoe, J. R. *et al.* Anion-exchange membranes in electrochemical energy systems. *Energy*

Environ. Sci. **7**, 3135–3191 (2014).

103. Koneshan, S., Rasaiah, J. C., Lynden-Bell, R. M. & Lee, S. H. Solvent Structure, Dynamics, and Ion Mobility in Aqueous Solutions at 25 °C. *J. Phys. Chem. B* **102**, 4193–4204 (1998).

104. Yu, V. China reports 'most severe' heatwave and third driest summer on record. *The Guardian* https://www.theguardian.com/world/2022/sep/07/china-reports-most-severe-heatwave-and-lowest-rainfall-on-record (2022).

105. Phillips, A., Dennis, B., Samenow, J., Muyskens, J. & Ahmed, N. Summer in America is becoming hotter, longer, and more dangerous. *Washington Post* (2022).

106. Kaplan, S. Europe just had its hottest summer in recorded history. *Washington Post* https://www.washingtonpost.com/climate-environment/2022/09/08/europe-record-hot-summer-extreme-heat/ (2022).

107. United States Environmental Protection Agency. Climate Change Indicators: U.S. and Global Temperature. *Https://Www.Epa.Gov/Climate-Indicators/Climate-Change-Indicators-Us-and-Global-Temperature* 1–10 (2021).

108. Arent, D. J., Wise, A. & Gelman, R. The status and prospects of renewable energy for combating global warming. *Energy Econ.* **33**, 584–593 (2011).

109. Zhao, Z. *et al.* Revealing the effects of conductive carbon materials on the cycling stability of rechargeable Zn-air batteries. *Int. J. Energy Res.* **46**, 7694–7703 (2022).

110. Cho, Y. G., Hwang, C., Cheong, D. S., Kim, Y. S. & Song, H. K. Gel/Solid Polymer Electrolytes Characterized by In Situ Gelation or Polymerization for Electrochemical Energy Systems. *Advanced Materials* vol. 31 (2019).

111. Bredar, A. R. C., Chown, A. L., Burton, A. R. & Farnum, B. H. Electrochemical Impedance Spectroscopy of Metal Oxide Electrodes for Energy Applications. *ACS Appl. Energy Mater.* **3**, 66–98 (2020).

112. Lee, D. U., Park, H. W., Park, M. G., Ismayilov, V. & Chen, Z. Synergistic bifunctional catalyst design based on perovskite oxide nanoparticles and intertwined carbon nanotubes

for rechargeable zinc-air battery applications. *ACS Appl. Mater. Interfaces* **7**, 902–910 (2015).

113. Lee, D. U. *et al.* Highly Active and Durable Nanocrystal-Decorated Bifunctional Electrocatalyst for Rechargeable Zinc–Air Batteries. *ChemSusChem* **8**, 3129–3138 (2015).

114. Chen, Z. *et al.* Highly active and durable core-corona structured bifunctional catalyst for rechargeable metal-air battery application. *Nano Lett.* **12**, 1946–1952 (2012).

115. Clark, M. P., Xiong, M., Cadien, K. & Ivey, D. G. High Performance Oxygen Reduction/Evolution Electrodes for Zinc–Air Batteries Prepared by Atomic Layer Deposition of MnOx. *ACS Appl. Energy Mater.* **3**, 603–613 (2020).

116. Aasen, D., Clark, M. & Ivey, D. G. A Gas Diffusion Layer Impregnated with Mn3O4-Decorated N-Doped Carbon Nanotubes for the Oxygen Reduction Reaction in Zinc-Air Batteries. *Batter. Supercaps* **2**, 882–893 (2019).

117. Shang, W. *et al.* Constructing the Triple-Phase Boundaries of Integrated Air Electrodes for High-Performance Zn–Air Batteries. *Adv. Mater. Interfaces* **8**, 2101256 (2021).